2018

Particle Fluxes In The North Pacific: An Assessment Of Pseudonitzschia And Domoic Acid In The Santa Barbara Basin, And Of Mercury, Carbon And Nitrogen In The Central Pacific

Blaire P. Umhau
University of South Carolina

PARTICLE FLUXES IN THE NORTH PACIFIC: AN ASSESSMENT OF *PSEUDO-NITZSCHIA* AND DOMOIC ACID IN THE SANTA BARBARA BASIN, AND OF MERCURY, CARBON AND NITROGEN IN THE CENTRAL PACIFIC

by

Blaire P. Umhau

Bachelor of Science
University of Miami, 2013

Submitted in Partial Fulfillment of the Requirements

For the Degree of Doctor of Philosophy in

Marine Science

College of Arts and Sciences

University of South Carolina

2018

Accepted by:

Claudia Benitez-Nelson, Major Professor

Michael Bizimis, Committee Member

Tammi Richardson, Committee Member

Brian Popp, Committee Member

Cheryl L. Addy, Vice Provost and Dean of the Graduate School

DEDICATION

Those who go down to the sea in ships,

Who do business on great waters,

They see the works of the LORD,

And His wonders in the deep.

Psalm 107:23-24 NKJV

For my parents, who sent me to sea the first time.

ACKNOWLEDGEMENTS

I would like to express my gratitude to the many people who made this work possible. Thanks are due to my advisor, Dr. Claudia Benitez-Nelson for presenting me with exciting fieldwork, research, and teaching opportunities and giving me the guidance and patience necessary so that I could learn as much as possible while accomplishing these tasks well. Thanks to my lab mates, past and present for their moral support and assistance with sample collecting and paper editing. Thanks to my co-authors who helped collect my samples and collaborated with me on the manuscripts for the equatorial Pacific and Santa Barbara Basin. Thanks to my committee members, Dr. Tammi Richardson, Dr. Brian Popp, and Dr. Michael Bizimis for their input and advice on these projects. And finally, thanks to my family for their unending encouragement.

ABSTRACT

Particle fluxes are an integral part of marine biogeochemical cycling and mediate the transfer of material from the surface ocean to depth. Throughout this process, particles are subjected to a suite of biological and physical processes that influence element and compound composition. Understanding these myriad factors is therefore critical for examining an array of marine biogeochemical questions that range from the role of particles in sequestering anthropogenic carbon dioxide, to serving as a food source and as vector for the removal and/or bioaccumulation of toxic chemicals. This thesis examines spatial and temporal changes in particle formation and export of nutrients, carbon, the neurotoxin domoic acid, and mercury using a combination of water column ^{238}U-^{234}Th disequilibria, *in situ* pumps, and sediment traps.

In Chapter 2, water column bulk *Pseudo-nitzschia* abundance and dissolved and particulate domoic acid (DA) concentrations were measured in the coastal waters of the Santa Barbara Basin (SBB), California from 2009-2013 and compared to bulk *Pseudo-nitzschia* abundance and DA concentrations and fluxes in sinking particles collected using moored sediment traps at 147 m and 509 m. Our results indicate that while a variety of *Pseudo-nitzschia* spp. exist in the SBB, specific species likely drive toxicity in response to a suite of environmental conditions that are complicated by physical processes and bloom stage. This work demonstrates that dissolved DA is a significant component of the water column and should not be ignored when examining potential

allelopathic impacts on competitors or deterrents to grazers. Water column *Pseudo-nitzschia* abundance and pDA concentrations were poorly correlated with sediment trap concentrations and fluxes, with *Pseudo-nitzschia* trap fluxes decreasing by an order of magnitude with increasing depth and DA fluxes increasing by a factor of three. However, DA toxicity is likely associated with senescent blooms that rapidly sink to the seafloor, adding another potential source of DA to benthic organisms.

In Chapter 3, the downward fluxes of particulate carbon (PC), nitrogen (PN) and total mercury (PHg) were measured at Station ALOHA in the North Pacific Subtropical Gyre using a combination of sediment traps and *in situ* pumps coupled with ^{238}U -^{234}Th disequilibria. While highest absolute PC fluxes were observed during the summer, our findings indicate that zooplankton exert more influence over both small and large PC (and PN) fluxes in February than in September or May, when heterotrophic bacteria play a proportionally larger role in particle remineralization and cycling. PHg fluxes were also seasonally variable and highest in May and September yet were influenced by different biogeochemical cycling processes than PC in the subsurface. PHg fluxes in May and September were higher than those previously measured in the equatorial Pacific and continue to be high (> 250 pmol Hg m^{-2} d^{-1}) down to 400 m, thereby providing a significant source of Hg that may be incorporated into the mesopelagic food web.

In Chapter 4, the role of dissolved oxygen in PC, PN, and PHg was explored using a combination of sediment traps and *in situ* pumps coupled with ^{238}U -^{234}Th disequilibria by sampling a transect within the central North Pacific Ocean along 155°W between 5 and 17°N. Results indicate that particle fluxes at 150 m throughout this region are very low, among the lowest measured. Water column profiles of fluorescence across

both oxygenated waters (5°N) and across the oxygen minimum zone (8°N) were similar, yet the magnitude of particle export was significantly higher in oxygenated waters, by a factor of 3 to 7 for PC, PN, and PHg. Furthermore, the peak in PHg fluxes occurred below the depth of maximum PC export. Combined, our results suggest that PC and PN production may have been influenced by a lack of small grazers, while PHg fluxes were additionally influenced by enhanced solubility in low oxygen waters. Thus, while oxygenation may influence particle production and remineralization rates in the upper water column, fluxes across 150 m remain low regardless of oxygen concentration.

TABLE OF CONTENTS

LIST OF FIGURES

LIST OF TABLES

CHAPTER 1: INTRODUCTION AND OVERVIEW

1.1 Overview

The biological pump is an intricate system of biogeochemical processes that move molecules, traditionally carbon (C), but also nutrients such as nitrogen (N), from the atmosphere into the ocean down to the sea floor (Honjo et al., 2008). In essence, C, in the form of carbon dioxide is removed from the atmosphere via photosynthesis in the euphotic zone and converted to particulate organic C (POC) by marine primary producers, e.g., phytoplankton. The resulting POC can be mixed downward through physical processes, consumed by zooplankton, or form aggregates that sink relatively rapidly to depth (Honjo et al., 2008; Savoye et al., 2006; Siegel et al., 2014) (Figure 1.1). Most of the POC produced is broken down into smaller and smaller particles until it is classified as dissolved organic C (DOC) or converted back into inorganic forms through bacterial remineralization or other chemical processes. While only a small fraction of POC is ultimately buried in marine sediments, this process has important implications for global climate with regards to the oceanic sequestration of atmospheric C, with estimates ranging from 5 to > 12 Pg C y^{-1} (Boyd and Trull, 2007; Henson et al., 2011). Marine particles also transport pollutants, toxins, metals and other elements that scavenge or adsorb onto particle surfaces, such as mercury. Quantifying the composition and magnitude of sinking particle fluxes therefore also has larger scale implications for understanding and addressing human health risks, particularly with regards to seafood consumption (Fitzgerald et al., 2007; Kvitek et al., 2008; Sekula-Wood et al., 2009).

Sinking particle fluxes are measured using a variety of methods ranging from the physical collection of particles as they sink through the water column to indirect methods that include geochemical mass balance, video, and tracers (Buesseler et al., 2007;

McDonnell and Buesseler, 2010; Savoye et al., 2006). None of these methods are prefect and are challenged by the spatial and temporal variability inherent to the ocean system. As such, understanding where and how particles are formed in the water column and how particles are modified as they sink through the water column remains one of the grand challenges facing the oceanographic field today (e.g., see Seigel et al., 2016).

Thorium-234 is a trace element that effectively scavenges onto both small and large particles and has a short half-life (24 days) compared to its parent, ^{238}U (4.5 billion years). The combination of these two elements provides a valuable proxy for measuring particle flux on the scale of days to weeks (Benitez-Nelson et al., 2001; Buesseler et al., 2009) and has been used previously to measure carbon, nutrient and trace element fluxes in a range of ocean environments (eg. Weinstein and Moran 2005; Maiti et al. 2008; Owens et al. 2015; Lamborg et al. 2016). In this dissertation, particle fluxes are measured using both sediment traps and uranium-238 (^{238}U) -Thorium-234 (^{234}Th) disequilibria. Both of these methods have advantages and drawbacks. One of the primary advantages of sediment traps is that they can be used to collect sinking particles continuously over time and, depending on the type of sediment trap used, provide fine scale temporal resolution (Buesseler et al., 2007). However, a major drawback is that they only allow for particle fluxes to be determined at a very specific depth horizon and are subject to hydrodynamic biases in the upper water column. In contrast, ^{238}U- ^{234}Th disequilibria can provide much finer vertical spatial resolution and integrates particle flux processes over days to weeks prior to collection. A major disadvantage, however, is that the calculation of specific fluxes requires knowledge of the element (or compound) to ^{234}Th ratio on sinking particles. Identification of "sinking particles" is often conducted using in situ pumps and

relies on specific size classes that may or may not reflect the actual sinking particle pool. Both small and large particles are important, but somewhat different, components of vertical particle fluxes (Puigcorbé et al., 2015; Richardson and Jackson, 2007) Recent work, indicates that using sediment traps and the ^{238}U- ^{234}Th method together can help differentiate which particle sizes are contributing to particle flux throughout the upper water column (Lam et al., 2015; Puigcorbé et al., 2015).

This dissertation focuses on understanding the composition and magnitude of particulate material as it moves from the surface ocean through the upper water column and into the twilight zone (> 500 m) using a combination of surface and deep moored sediment traps, and ^{238}U-^{234}Th disequilibria. Chapter 1 focuses on examining the role that upwelling plays in the appearance, persistence, and efficiency in the downward transport of the neurotoxin, domoic acid, produced by the diatom *Pseudo-nitzschia*, in the Santa Barbara Basin, California. Chapter 2 focuses on particulate carbon, nitrogen, and mercury production and the role that seasonality, specifically the late summer bloom and zooplankton grazing, plays on their downward transport at Station ALOHA in the North Pacific Subtropical Gyre. Chapter 3 expands on the spatial range of particulate carbon, nitrogen, and mercury production and examines how the export of carbon, nitrogen, and mercury changes from Station ALOHA south into the Equatorial Pacific Ocean across an oxygen minimum zone. A more detailed overview of each Chapter is provided below.

1.2 *Pseudo-nitzschia* and domoic acid in the Santa Barbara Basin

Pseudo-nitzschia is a diatom found worldwide, and many of the species of this genus produce a neurotoxin, domoic acid (Trainer et al., 2012). Severe cases of domoic acid toxicity, also called amnesiac shellfish poisoning, can cause memory loss, seizures

and death in humans, and cause similar symptoms in marine mammals and seabirds (Costa et al., 2010; Goldstein et al., 2008a; Lelong et al., 2012; Scholin et al., 2000; Watanabe et al., 2011). Domoic acid toxicity occurs mainly through consumption of contaminated food such as shellfish or anchovies that have ingested particulates containing the toxin (Bargu et al., 2002; Trainer et al., 2012, 2000). While found world-wide, toxic blooms of *Pseudo-nitzschia* are particularly prevalent during and after coastal upwelling events and the associated change in temperature, salinity, and nutrient availability (Ryan et al., 2017; Trainer et al., 2012), and have been increasing in frequency since the turn of the century (Sekula-Wood et al. 2011; Barron et al. 2013, Figure 1.2). Once produced, DA persists in the environment for days to months, depending on location in the water column, particulate versus. dissolved form and food web ecology (Bouillon et al., 2006; Sekula-Wood et al., 2009; Timmerman et al., 2014). *Pseudo-nitzschia* and associated particulate DA have been found throughout the water column and as deep as 800 m, providing a source of DA to the food web long after the bloom ends (Sekula-Wood et al., 2011; Timmerman et al., 2014), but many studies have not taken into account the role that dissolved DA plays. In this dissertation, a time series of both sediment trap fluxes and water column measurements from the Santa Barbara Basin from 2009-2013, a site of frequent *Pseudo-nitzschia* blooms, is analyzed. *Pseudo-nitzschia* abundances, dissolved and particulate DA from both the water column and sinking into sediment traps is discussed in the context of upwelling and non-upwelling periods.

1.3 Seasonal changes in particulate carbon, nitrogen and mercury in the central Pacific

The magnitude and composition of particle fluxes from the surface to the deep ocean are key elements of understanding the biogeochemical cycles of trace elements, carbon and nitrogen (Buesseler et al., 2008). The cycling and composition of these particles is partially mediated through complex food webs that span the water column as part of the biological pump (Buesseler et al., 2008; Buesseler and Boyd, 2009; Siegel et al., 2014). Particles also play a role in the introduction and subsequent bioaccumulation of trace metals, such as mercury (Hg), which can enter the food web via particle scavenging and ingestion (Lam et al., 2015; Lam and Marchal, 2015; Lamborg et al., 2016). Hg is a potent toxin, particularly in its methylated forms, which are produced in the water column from particulate Hg (PHg). Methylmercury bioaccumulates in fish that may be consumed by humans, exposing them to this potent neurotoxin (Figure 1.3). Characterizing PHg fluxes are therefore critical for improving our understanding of how Hg enters the food web.

Station ALOHA (22^{o}N, 158^{o}W) is an oligotrophic region subject to a seasonal summer export pulse that is up to three times higher than the particle flux seen at other times of the year (Böttjer et al., 2017; Karl et al., 2012). This work provides some of the first measurements of seasonal changes in small and large PHg fluxes using ^{238}U-^{234}Th disequilibria and relates the PHg fluxes to seasonal changes in small and large PC and PN fluxes collected using sediment traps and the ^{238}U-^{234}Th method.

1.4 Spatial changes in particulate mercury, carbon and nitrogen in the central Pacific

One important mediator of particle cycling, especially formation and remineralization dynamics, is microbial activity. Microbial activity changes with dissolved oxygen concentrations; most bacterial degradation takes place in very low or anoxic environments (Bianchi et al., 2018; Blum et al., 2013; Choy et al., 2009). In the central equatorial Pacific ocean between 15^{o}N and the equator, an oxygen minimum zone shoals, reaching depths as shallow as 200 m near 10^{o}N (Munson et al. 2015, Figure 1.4). This work examines how particle fluxes change along a north-south transect that stretches from 17^{o}N to 5^{o}N at 155^{o}W covering a range of oxygen regimes. Of particular interest is particulate mercury, which has been shown to be methylated at higher rates in low oxygen zones (Blum et al., 2013; Munson et al., 2015). Previous work has focused latitudinal changes in dissolved and particulate concentrations of Hg, and included some sediment trap fluxes in this region (Munson et al., 2015), but this will be some of the first data presented examining PHg fluxes divided into small and large size fractions using the ^{238}U-^{234}Th disequillibria. Spatial changes in PC and PN fluxes and concentrations are also discussed in relation to particulate Hg as well as the changes in water chemistry with latitude.

1.5 References

Bargu, S., Powell, C., Coale, S., Busman, M., Doucette, G., Silver, M., 2002. Domoic acid detection in krill: a potential vector in marine food webs. Mar. Ecol. Prog. Ser. 237, 209–219. doi:10.3354/meps237209

Barron, J. a., Bukry, D., Field, D.B., Finney, B., 2013. Response of diatoms and silicoflagellates to climate change and warming in the California Current during the past 250 years and the recent rise of the toxic diatom Pseudo-nitzschia australis. Quat. Int. 310, 140–154. doi:10.1016/j.quaint.2012.07.002

Benitez-Nelson, C.R., Buesseler, K.O., van der Loeff, M.R., Andrews, J., Ball, L., Crossin, G., Charette, M.A., 2001. Testing a new small-volume technique for determining 234 Th in seawater. J. Radioanal. Nucl. Chem. 248, 795–799.

Bianchi, D., Weber, T.S., Kiko, R., Deutsch, C., 2018. Global niche of marine anaerobic metabolisms expanded by particle microenvironments. Nat. Geosci. 11, 263–268. doi:10.1038/s41561-018-0081-0

Blum, J.D., Popp, B.N., Drazen, J.C., Anela Choy, C., Johnson, M.W., 2013. Methylmercury production below the mixed layer in the North Pacific Ocean. Nat. Geosci. 6, 879–884. doi:10.1038/ngeo1918

Böttjer, D., Dore, J.E., Karl, D.M., Letelier, R.M., Mahaffey, C., Wilson, S.T., Zehr, J., Church, M.J., 2017. Temporal variability of nitrogen fixation and particulate nitrogen export at Station ALOHA. Limnol. Oceanogr. 62, 200–216. doi:10.1002/lno.10386

Bouillon, R.-C., Knierim, T.L., Kieber, R.J., Skrabal, S. a., Wright, J.L.C., 2006. Photodegradation of the algal toxin domoic acid in natural water matrices. Limnol. Oceanogr. 51, 321–330. doi:10.4319/lo.2006.51.1.0321

Buesseler, K.O., Antia, A.N., Chen, M., Fowler, S.W., Gardner, W.D., Gustafsson, O., Harada, K., Michaels, A.F., van der Loeff, M.R., Sarin, M., Steinberg, D.K., Trull, T., 2007. An assessment of the use of sediment traps for estimating upper ocean particle fluxes. J. Mar. Res. 65, 345–416. doi:10.1357/002224007781567621

Buesseler, K.O., Boyd, P.W., 2009. Shedding light on processes that control particle export and flux attenuation in the twilight zone of the open. Limnol. Oceanogr. 54, 1210–1232.

Buesseler, K.O., Pike, S., Maiti, K., Lamborg, C.H., Siegel, D.A., Trull, T.W., 2009. Thorium-234 as a tracer of spatial , temporal and vertical variability in particle flux in the North Pacific. Deep. Res. Part I 56, 1143–1167. doi:10.1016/j.dsr.2009.04.001

Buesseler, K.O., Trull, T.W., Steinberg, D.K., Silver, M.W., Siegel, D.A., Saitoh, S., Lamborg, C.H., Lam, P.J., Karl, D.M., Jiao, N.Z., Honda, M.C., Elskens, M., Dehairs, F., Brown, S.L., Boyd, P.W., Bishop, J.K.B., Bidigare, R.R., 2008. VERTIGO (VERtical Transport In the Global Ocean): A study of particle sources and flux attenuation in the North Pacific. Deep. Res. II 55, 1522–1539. doi:10.1016/j.dsr2.2008.04.024

Choy, C.A., Popp, B.N., Kaneko, J.J., Drazen, J.C., 2009. The influence of depth on mercury levels in pelagic fishes and their prey. Proc. Natl. Acad. Sci. U. S. A. 106, 13865–13869. doi:10.1073/pnas.0900711106

Costa, L.G., Giordano, G., Faustman, E.M., 2010. Domoic acid as a developmental neurotoxin. Neurotoxicology 31, 409–23. doi:10.1016/j.neuro.2010.05.003

Fitzgerald, W.F., Lamborg, C.H., Hammerschmidt, C.R., 2007. Marine biogeochemical cycling of mercury. Chem. Rev. 107, 641–62. doi:10.1021/cr050353m

Goldstein, T., Mazet, J. a K., Zabka, T.S., Langlois, G., Colegrove, K.M., Silver, M., Bargu, S., Van Dolah, F., Leighfield, T., Conrad, P. a, Barakos, J., Williams, D.C., Dennison, S., Haulena, M., Gulland, F.M.D., 2008. Novel symptomatology and changing epidemiology of domoic acid toxicosis in California sea lions (Zalophus californianus): an increasing risk to marine mammal health. Proc. Biol. Sci. 275, 267–276. doi:10.1098/rspb.2007.1221

Honjo, S., Manganini, S.J., Krishfield, R.A., Francois, R., 2008. Particulate organic carbon fluxes to the ocean interior and factors controlling the biological pump: A synthesis of global sediment trap programs since 1983. Prog. Oceanogr. 76, 217–285. doi:10.1016/j.pocean.2007.11.003

Karl, D.M., Church, M.J., Dore, J.E., Letelier, R.M., Mahaffey, C., 2012. Predictable and efficient carbon sequestration in the North Pacific Ocean supported by symbiotic nitrogen fixation. Proc. Natl. Acad. Sci. U. S. A. 109, 1842–9. doi:10.1073/pnas.1120312109

Kvitek, R., Goldberg, J., Smith, G., Doucette, G., Silver, M., 2008. Domoic acid contamination within eight representative species from the benthic food web of Monterey Bay, California, USA. Mar. Ecol. Prog. Ser. 367, 35–47. doi:10.3354/meps07569

Lam, P.J., Marchal, O., 2015. Insights into Particle Cycling from Thorium and Particle Data. Ann. Rev. Mar. Sci. 7, 159–184. doi:10.1146/annurev-marine-010814-015623

Lam, P.J., Ohnemus, D.C., Auro, M.E., 2015. Size-fractionated major particle composition and concentrations from the US GEOTRACES North Atlantic Zonal Transect. Deep. Res. Part II Top. Stud. Oceanogr. 116, 303–320. doi:10.1016/j.dsr2.2014.11.020

Lamborg, C.H., Hammerschmidt, C.R., Bowman, K.L., 2016. An examination of the role of particles in oceanic mercury cycling. Philos. Trans. R. Soc. A 374.

Lelong, A., Hegaret, H., Soudant, Ph., Bates, S.S., 2012. Pseudo-nitzschia (Bacillariophyceae) species , domoic acid and amnesic shellfish poisoning : revisiting previous paradigms. Phycologia 51, 168–216. doi:10.2216/11-37

Maiti, K., Benitez-nelson, C.R., Rii, Y., Bidigare, R., 2008. Deep-Sea Research II The influence of a mature cyclonic eddy on particle export in the lee of Hawaii. Deep Sea Res. II 55, 1445–1460. doi:10.1016/j.dsr2.2008.02.008

McDonnell, A.M.P., Buesseler, K.O., 2010. Variability in the average sinking velocity of marine particles. Limnol. Oceanogr. 55, 2085–2096. doi:10.4319/lo.2010.55.5.2085

Munson, K.M., Lamborg, C., Swarr, G.J., Saito, M.A., 2015. Mercury species concentrations and fluxes in the Central Tropical Pacific Ocean. Global Biogeochem. Cycles 29, 656–676. doi:10.1002/2015GB005120.Received

Owens, S.A., Pike, S., Buesseler, K.O., 2015. Thorium-234 as a tracer of particle dynamics and upper ocean export in the Atlantic Ocean. Deep Sea Res. Part II Top.

Stud. Oceanogr. 116, 42–59. doi:10.1016/j.dsr2.2014.11.010

Puigcorbé, V., Benitez-nelson, C.R., Masqué, P., Verdeny, E., White, A.E., Popp, B.N., Prahl, F.G., Lam, P.J., 2015. Small phytoplankton drive high summertime carbon and nutrient export in the Gulf of California and Eastern Tropical North Pacific. Global Biogeochem. Cycles 1309–1332. doi:10.1002/2015GB005134.Received

Richardson, T.L., Jackson, G.A., 2007. Small Phytoplankton and Carbon Export from the Surface Ocean. Science (80-.). 838–840. doi:10.1126/science.1133471

Ryan, J.P., Kudela, R.M., Birch, J.M., Blum, M., Bowers, H.A., Chavez, F.P., Doucette, G.J., Hayashi, K., Marin III, R., Mikulski, C.M., Pennington, J.T., Scholin, C.A., Smith, G.J., Woods, A., Zhang, Y., 2017. Causality of an extreme harmful algal bloom in Monterey Bay, California, during the 2014–2016 northeast Pacific warm anomaly. Geophys. Res. Lett. 44, 5571–5579. doi:10.1002/2017GL072637

Savoye, N., Benitez-Nelson, C.R., Burd, A., Cochran, J.K., Charette, M., Buesseler, K.O., Jackson, G.A., Roy-Barman, M., Schmidt, S., Elskens, M., 2006. Th-234 sorption and export models in the water column : a review. Mar. Chem. 100, 234–249.

Scholin, C.A., Gulland, F., Doucette, G.J., Benson, S., Busman, M., Chavez, F.P., Cordaro, J., Delong, R., Vogelaere, A. De, Harvey, J., Haulena, M., Lefebvre, K., Lipscomb, T., Loscutoff, S., Lowenstine, L.J., Marin III, R., Miller, P.E., Mclellan, W.A., Moeller, P.D.R., Powell, C.L., Rowles, T., Silvagni, P., Silver, M., Spraker, T., Trainer, V., Dolah, F.M. Van, 2000. Mortality of sea lions along the central California coast linked to a toxic diatom bloom. Lett. to Nat. 403, 80–84.

Sekula-Wood, E., Benitez-Nelson, C., Morton, S., Anderson, C., Burrell, C., Thunell, R., 2011. Pseudo-nitzschia and domoic acid fluxes in Santa Barbara Basin (CA) from 1993 to 2008. Harmful Algae 10, 567–575. doi:10.1016/j.hal.2011.04.009

Sekula-Wood, E., Schnetzer, A., Benitez-Nelson, C.R., Anderson, C., Berelson, W.M., Brzezinski, M. a., Burns, J.M., Caron, D. a., Cetinic, I., Ferry, J.L., Fitzpatrick, E., Jones, B.H., Miller, P.E., Morton, S.L., Schaffner, R. a., Siegel, D. a., Thunell, R., 2009. Rapid downward transport of the neurotoxin domoic acid in coastal waters. Nat. Geosci. 2, 272–275. doi:10.1038/ngeo472

Siegel, D.A., Buesseler, K.O., Doney, S.C., Sailley, S.F., Behrenfeld, M.J., Boyd, P.W., 2014. Global assessment of ocean carbon export by combining satellite observations and food-web models. Global Biogeochem. Cycles 28, 181–196. doi:10.1002/2013GB004743.Received

Timmerman, A.H.V., McManus, M. a., Cheriton, O.M., Cowen, R.K., Greer, A.T., Kudela, R.M., Ruttenberg, K., Sevadjian, J., 2014. Hidden thin layers of toxic diatoms in a coastal bay. Deep Sea Res. Part II Top. Stud. Oceanogr. 101, 129–140. doi:10.1016/j.dsr2.2013.05.030

Trainer, V.L., Adams, N.G., Bill, B.D., Stehr, C.M., Wekell, J.C., Moeller, P., Busman, M., Woodruff, D., Helena, M., Sellner, K., Cordaro, J., Thomas, N., Lowenstein, L., Chec-, M., Lefebvre, K., Reidarson, T., Langlois, G., 2000. Domoic acid production near California coastal upwelling zones , June 1998. Limnol. Oceanogr. 45, 1818–1833.

Trainer, V.L., Bates, S.S., Lundholm, N., Thessen, A.E., Cochlan, W.P., Adams, N.G.,

Trick, C.G., 2012. Pseudo-nitzschia physiological ecology, phylogeny, toxicity, monitoring and impacts on ecosystem health. Harmful Algae 14, 271–300. doi:10.1016/j.hal.2011.10.025

Watanabe, K.H., Andersen, M.E., Basu, N., Carvan, M.J., Crofton, K.M., King, K. a, Suñol, C., Tiffany-Castiglioni, E., Schultz, I.R., 2011. Defining and modeling known adverse outcome pathways: Domoic acid and neuronal signaling as a case study. Environ. Toxicol. Chem. 30, 9–21. doi:10.1002/etc.373

Weinstein, S.E., Moran, S.B., 2005. Vertical flux of particulate Al, Fe, Pb, and Ba from the upper ocean estimated from234Th/238U disequilibria. Deep. Res. Part I Oceanogr. Res. Pap. doi:10.1016/j.dsr.2005.03.008

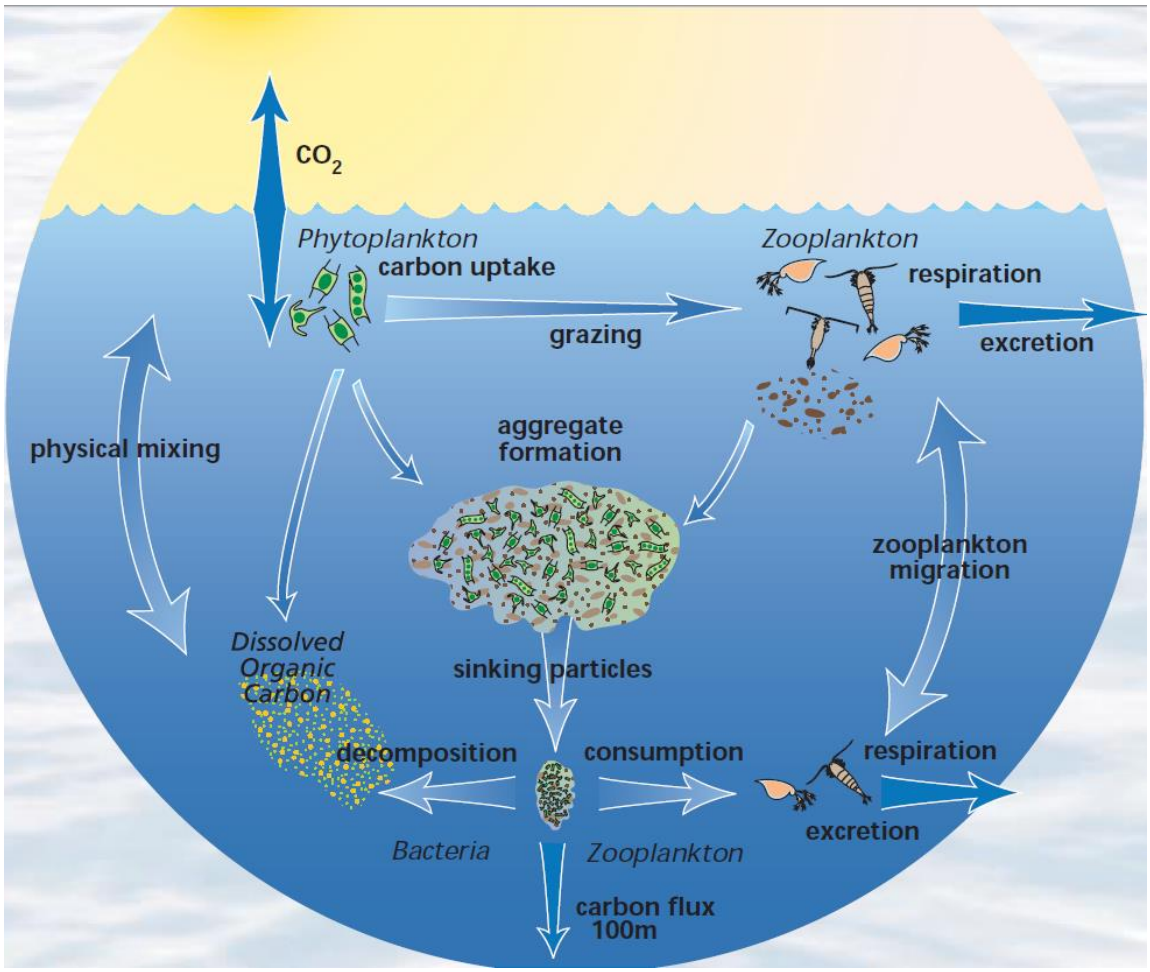

Figure 1.1Diagram of the biological pump showing carbon's path from the atmosphere to the deep ocean (Buesseler et al. 2001)

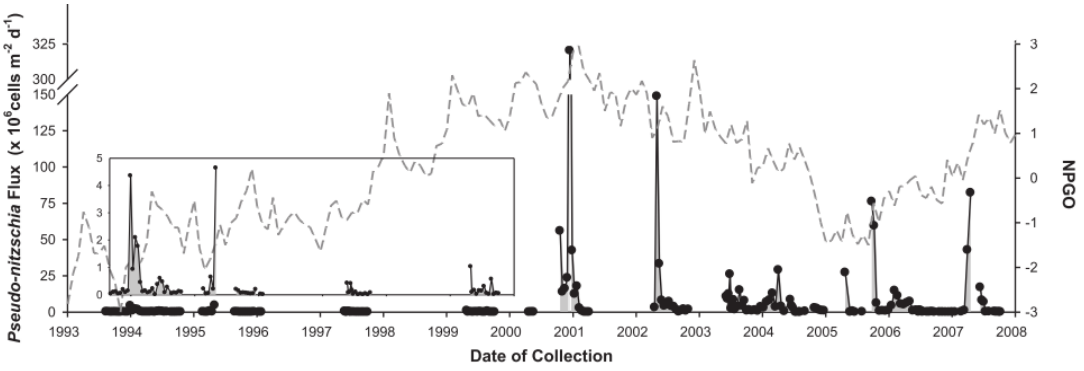

Figure 1.2. Plot of Pseudo-nitzschia flux in the Santa Barbara Basin over time (black circles) and the North Pacific Gyre Oscillation (NPGO). Adapted from Sekula-wood et al. (2011).

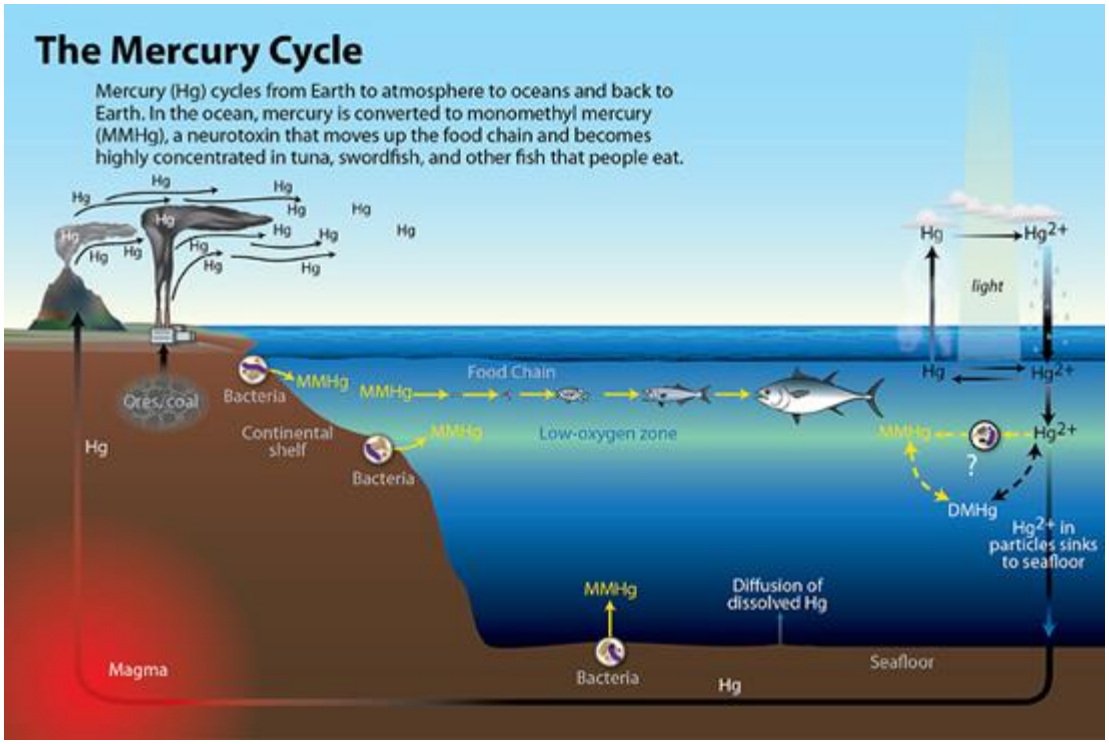

Figure 1.3 Schematic of the mercury cycle (Cook 2010)

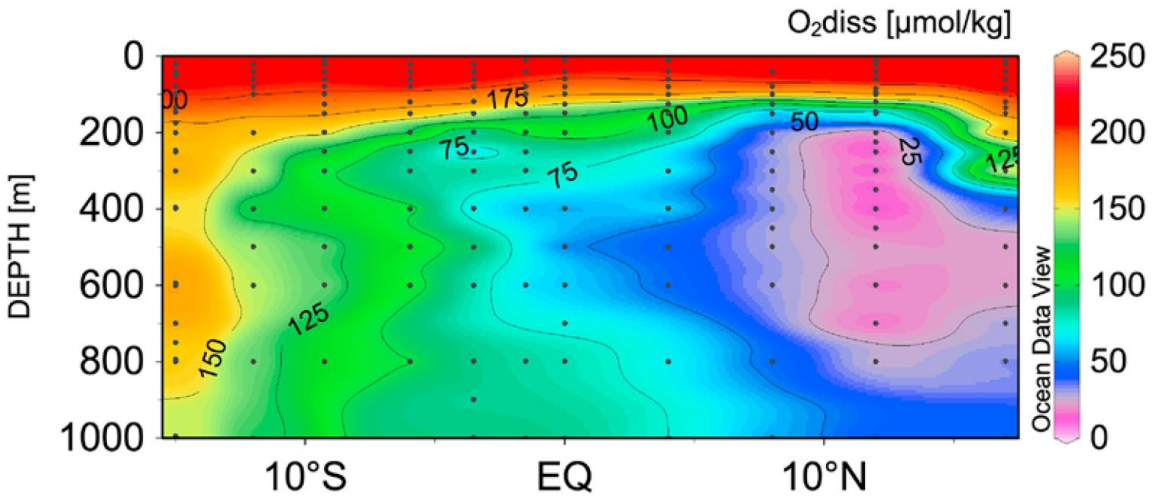

Figure 1.4 Dissolved oxygen profile along 155ºW (adapted from Munson et al., 2015)

CHAPTER 2: A TIME SERIES OF WATER COLUMN DISTRIBUTIONS AND SINKING PARTICLE FLUX OF *PSEUDO-NITZSCHIA* AND DOMOIC ACID IN THE SANTA BARBARA BASIN, CALIFORNIA[1]

[1] Blaire P. Umhau, Claudia R. Benitez-Nelson, Clarissa R. Anderson, Robert C. Thunell, Kelly McCabe, and Christopher Burrell. Submitted to *Harmful Algae* 4/30/2018.

Abstract

Water column bulk *Pseudo-nitzschia* abundance and dissolved and particulate domoic acid (DA) concentrations were measured in the coastal waters of the Santa Barbara Basin (SBB), California from 2009-2013 and compared to bulk *Pseudo-nitzschia* abundance and DA concentrations and fluxes in sinking particles collected using moored sediment traps at 147 m and 509 m. *Pseudo-nitzschia* were prevalent throughout the study period and were spatially heterogeneous (ranging from below detection to 3.8×10^6 cells L^{-1}, and averaging $2 \times 10^5 \pm 5 \times 10^5$ cells L^{-1} across the basin) with no significant relationship to environmental factors such as temperature or nutrient abundance associated with upwelling. Total DA (tDA) concentrations were also spatially and temporally diverse (ranging from below detection to 2.2×10^5 ng L^{-1} and averaging $7.8 \times 10^3 \pm 2.2 \times 10^4$ ng L^{-1}) and showed no significant correlation with bulk *Pseudo-nitzschia* abundance. This indicates that while a variety of *Pseudo-nitzschia* spp. exist in the SBB, specific species likely drive toxicity in response to a suite of environmental conditions that are complicated by physical processes and bloom stage. Dissolved (dDA) and particulate (pDA) DA were significantly and positively correlated ($p < 0.01$) and both comprised major components of the total DA pool (pDA = 57 ± 35%, and dDA = 42 ± 35%) with substantial water column concentrations (> 1000 cells L^{-1} and tDA = 200 ng L^{-1}) measured as deep as 150 m. Surface measurements therefore underestimate the potential for DA toxicity in the SBB. Our results also highlight that dDA is a significant component of the water column and should not be ignored when examining potential allelopathic impacts on competitors or deterrents to grazers. Dissolved DA may further serve as an indicator of toxigenic *Pseudo-nitzschia* spp. presence when no other

measurements are available. Water column *Pseudo-nitzschia* abundance and pDA concentrations were poorly correlated with sediment trap concentrations and fluxes, with *Pseudo-nitzschia* trap fluxes decreasing by an order of magnitude with increasing depth and DA fluxes increasing by a factor of three. While disparate sampling intervals and temporal differences between plankton blooms and the aggregation and sinking of particles to depth obscure differentiation of specific transport pathways, DA toxicity is likely associated with senescent blooms that rapidly sink to the seafloor, adding another potential source of DA to benthic organisms.

2.1. Introduction

The genus *Pseudo-nitzschia* is a marine diatom found worldwide (Trainer et al., 2012), with 26 of the 49 known species capable of producing a potent neurotoxin, domoic acid (DA) . Domoic acid contamination is caused predominantly by trophic transfer; particulate material (e.g., diatoms) containing DA is consumed by zooplankton and fish or ingested by filter feeding shellfish, which are subsequently consumed by marine mammals, seabirds and humans (Bargu et al., 2002; Leandro et al., 2010; Lefebvre et al., 2010; Trainer et al., 2000, 2012, Tammilehto et al., 2015). Toxin-producing blooms of *Pseudo-nitzschia* have been implicated in widespread marine mammal strandings and mortalities, as well as shellfish bed and beach closures (Scholin et al., 2000; Goldstein et al., 2008; Schnetzer et al., 2013; McCabe et al., 2016; Nash et al., 2017). Domoic acid toxicity, also known as amnesic shellfish poisoning (ASP) in humans, can cause headaches, nausea, seizures, short term memory loss, and in more severe cases, coma and death (Costa et al., 2010; Watanabe et al., 2011; Lelong et al., 2012). While toxic *Pseudo-nitzschia* spp. form blooms in both open and coastal settings, they are particularly

prominent during and immediately following coastal upwelling events, when cold nutrient rich waters enter the euphotic zone (e.g., Trainer et al. 2012; Ryan et al., 2017). Identifying a common set of conditions that promote these blooms across regions and seasons, however, remains elusive (Trainer et al., 2012). Indeed, DA production varies greatly within and between blooms and appears to be influenced by a variety of additional environmental conditions including pH, light intensity, and salinity (Lelong et al., 2012; Macintyre et al. (2010), relative nutrient (nitrogen, phosphorus, and silicic acid) availability and composition (Anderson et al., 2006, 2009; Schnetzer et al., 2007; Howard et al. 2007, Lane et al., 2009), trace metal abundance (e.g., Wells et al., 2005), and even carbon dioxide concentration (Tatters et al., 2012). Other factors include the presence of zooplankton (Haroardottir et al., 2015; Tammilehto et al., 2015), the composition of the bacterial community (Sison-Mangus et al., 2014; 2016), the specific *Pseudo-nitzschia* spp. present (e.g., Trainer et al., 2012) and population growth phase (Thorel et al., 2014; Schnetzer et al., 2016)

Once produced, DA may persist in the environment for days to months depending on food web ecology, particulate versus dissolved form, and water column location (i.e., euphotic zone versus deep waters or sediments) (Bouillon et al., 2006; Sekula-Wood et al., 2009; Timmerman et al., 2014). As DA has been hypothesized to be produced predominantly in the upper water column and photodegradation is considered an important degradation pathway (e.g., Bouillon et al. 2006), many studies have focused on targeting marine biota and sampling surface waters for DA, rarely sampling below 10 m (e.g., Trainer et al., 2012 and references therein).

It is now recognized that significant particulate DA (pDA) is produced throughout the upper water column, with particle-laden DA sinking to waters as deep as 800 m (Hagström et al., 2007; Schnetzer et al., 2013, 2007; Sekula-Wood et al., 2009). For example, Sekula -Wood et al. (2009, 2011) found high quantities of DA in sediment traps at a depth of 540 m in the Santa Barbara Basin, (>20,000 ng/g sediment), thereby providing a source of DA to benthic and pelagic feeders. The transport of DA to sub-surface waters is likely mediated by secondary processes, such as fecal pellet production and marine snow aggregation and adsorption onto the surfaces of particles (Maneiro et al., 2000; Burns and Ferry 2007; Sekula-Wood et al., 2011; Schnetzer et al., 2016) that sink rapidly, exceeding 100 m d^{-1} (Alldredge and Gotschalk 1989; Sekula-Wood et al., 2009, 2011). These results help to explain the presence of DA in benthic food webs in the absence of an ongoing surface bloom (e.g., Vigilant and Silver 2007; Kvitek et al., 2008), thereby allowing for the possibility of DA poisoning long after a toxic *Pseudo-nitzschia* bloom subsides (Hagström et al., 2007; Sekula-Wood et al., 2009).

The focus on pDA has also resulted in a relative paucity of dissolved DA (dDA) measurements, which may also impact marine biota. For example, Liu et al. (2007) found that dDA exposure reduced the survival and growth of larval king sea scallops, and Bargu et al. (2006) showed that increasing levels of dDA suppressed the grazing rates of krill. In zebrafish, dDA exposure has been shown to cause irregular cardiovascular development (Hong et al. 2015). More recently Van Meerssche and Pinckney (2017) found that at increased salinities, the concentration of dDA inhibited the growth of certain estuarine phytoplankton species, such as cryptophytes. Other studies suggest that dDA may provide *Pseudo-nitzschia* spp. with a competitive advantage over other organisms in low

iron environments, although the mechanism is not well understood (Rue and Bruland, 2001; Prince et al., 2013). Combined, studies of dDA and pDA suggest that there are multiple pathways and timescales for DA to enter and impact the marine food web.

As mentioned earlier, many of the conditions hypothesized to facilitate toxic *Pseudo-nitzschia* blooms are specifically associated with coastal upwelling, including off the coasts of Southern Africa, Western Europe, South America and the United States (Trainer et al., 2012 Schnetzer et al., 2013; Husson et al., 2016; Louw et al., 2017; McKibben et al., 2017; Odebrecht et al., 2001). The coast of southern California, in particular, experiences regular outbreaks of toxic *Pseudo-nitzschia* blooms with a majority of them linked to either seasonal upwelling (Anderson et al., 2006; Fryxell et al., 1997, Kudela et al., 2005; Trainer et al., 2012), regional circulation (e.g., mesoscale eddies; Anderson et al., 2006), and/or larger scale circulation patterns linked to climate (McCabe et al., 2016; McKibben et al, 2017)). Recent studies further suggest that there has been an increase in the frequency of southern California toxic *Pseudo-nitzschia* blooms and specifically in the Santa Barbara Basin (SBB) over the past decade and perhaps the last century (Sekula-Wood et al., 2011; Barron et al., 2013). The SBB is a hotspot for toxic *Pseudo-nitzschia* and numerous studies have identified links between seasonal upwelling conditions, *Pseudo-nitzschia* growth, and DA production in the basin (e.g., Anderson et al., 2008; 2009; Trainer et al., 2000; Schnetzer et al., 2013; Seubert et al., 2013).

This study examined the partitioning of DA between dissolved and particulate phases relative to the presence of *Pseudo-nitzschia* throughout the upper water column, especially with regards to upwelling and non-upwelling periods in order to verify the

upwelling association with blooms that was demonstrated in some previous SBB studies. The timing and magnitude of toxic *Pseudo-nitzschia* blooms and the downward transport of *Pseudo-nitzschia* and DA from the surface ocean to depth in the water column was also explored. Results are placed in context of current knowledge regarding toxic *Pseudo-nitzschia* blooms not only along the California coast, but worldwide.

2.2. Study Area

The SBB, located off the coast of southern California (Figure 1), is a region of high primary production and particle export (Kahru et al., 2012; Krause et al., 2013). Phytoplankton blooms, dominated by diatoms, generally occur in the spring and summer in response to wind-driven upwelling and mesoscale eddies (Anderson et al., 2006, 2008; Brzezinski and Washburn, 2011). The SBB is located at the confluence of two different water masses: the surface equatorward flowing California Current (CC) that originates in the subarctic Pacific, and the poleward deeper (200-300 m) flowing California Undercurrent (CUC) that forms in the tropical northeastern Pacific (Hickey, 1979, 1998; Lynn and Simpson, 1987). These two currents are comprised of different nutrient concentrations and ratios. Changes in the relative magnitude and nutrient composition of the CC and CUC flow into the SBB has therefore been argued to play a role in the increase of toxic *Pseudo-nitzschia* blooms over the past two decades (Bograd et al., 2015). The SBB is bounded by the California coast to the north and south by a shallow continental margin sill that restricts water exchange with the open ocean resulting in a well-developed oxygen minimum zone below ~ 475 m.

2.3. Methods

2.3.1 Pier stations

Pier station data were collected at Stearns Wharf (34° 24.48' N, 119° 41.10' W) and Goleta Pier (32° 52.02' N,117° 15.42' W) in Santa Barbara, CA through the Southern California Coastal Ocean Observing System (SCCOOS, Figure 1) HAB monitoring program. The pier data used in this study range from January 2009 - December 2013. Samples were collected weekly and analyzed for pDA, *Pseudo-nitzschia* abundance, and a suite of other water quality parameters in accordance with SCCOOS and Harmful Algal Bloom Monitoring and Alert Program (HABMAP) monitoring protocols (see Seubert et al. 2013). Water samples for pDA were filtered through GF/F filters and pDA was measured using the ELISA bioassay (Seubert et al. 2013). Dissolved DA was not measured, therefore tDA data are not available. Cellular DA concentrations were determined by dividing the measured pDA by the total *Pseudo-nitzschia* abundance. *Pseudo-nitzschia* were divided into two size classes and designated as either the *P. delicatissima* type (frustule widths < 3 µm) or the *P. seriata* type (frustule width >3 µm) (Seubert et al., 2013). The reason for the size class distinction is to provide a rough estimate of toxigenic species abundance *in lieu* of routinely using scanning electron microscopy to definitively identify *Pseudo-nitzschia* at the species level. *P. delicatissima*, or the narrow size class, is rarely associated with toxic blooms, while *P. seriata*, or the wide size class, may contain highly toxigenic species, such as *P. multiseries* and *P. australis* (Seubert et al., 2013). As no scanning electron microscopy was conducted during this study, we use narrow and wide to describe the *Pseudo-nitzschia* size class data collected at the piers.

2.3.2 Offshore Stations

Water samples were collected monthly at seven stations located along a transect through the middle of the SBB as part of the University of California Santa Barbara Plumes and Blooms project from March 2009 - June 2013 (Figure 2.1). Only surface samples were collected at stations 1-3 and 5-7 using Niskin bottles attached to a standard rosette. At Station 4, located in the center of the SBB (34°15'N, 119°54'W), samples were typically collected at seven standard depths (0, 10, 20, 30, 75, 100, and 150 m) as well as at the deep chlorophyll maximum. Samples from Niskin bottles were collected for dDA and pDA concentrations, and *Pseudo-nitzschia* cell abundances. Conductivity, temperature and depth (CTD) profiles and photosynthetically active radiation (PAR) were also measured at all stations as part of the Plumes and Blooms core measurements using the methods described in Anderson et al. (2008).

Pseudo-nitzschia samples were preserved in borate buffered formalin with a final concentration of 2%. *Pseudo-nitzschia* cell abundances were counted using the Utermöhl method (Hasle 1978; Sekula-Wood et al., 2009). Aliquots (10 mL) were settled and cells over 5 □m were counted at 400X magnification with a minimum cell count of 100 cells per sample. Unlike the pier stations, there was no distinction made between narrow or wide *Pseudo-nitzschia* frustules in the offshore station samples. Approximately 500 mL seawater samples were filtered through a Whatman 25 mm GF/F and the filters were immediately frozen and stored at -80°C. Whole water samples were filtered using 0.45 µm GF/F syringe filters into acid cleaned scintillation vials and stored refrigerated prior to measurement of dDA. Particulate and dissolved DA concentrations were measured for each water sample using the method described in Sekula-Wood et al. (2009, 2011).

Briefly, samples were analyzed using tandem Liquid Chromatography Mass Spectrometry (LC-MS/MS) with a mobile phase of 0.1% formic acid in deionized water and 0.1% formic acid in acetonitrile with a detection limit of 1.3 ng DA mL^{-1}. Total DA (tDA) concentrations are the sum of pDA and dDA concentrations. Cellular DA (cDA) is calculated as the amount of pDA per total *Pseudo-nitzschia* cell abundance in a known volume. To better link water column observations to the concentration and fluxes of material captured in the moored sediment traps, *Pseudo-nitzschia* cell abundance and pDA concentrations from the upper 150 m of the water column at Station 4 were depth-integrated by trapezoidal rule using the midpoint between sample depths and the measured concentrations at that sample depth. In other words, the mid depth between specific sampling points was used to define a depth range. The concentration measured at a specific sampling point was then multiplied by that depth range to obtain an integrated concentration. These integrated "boxes" were then summed over a specific depth interval of interest to determine an inventory of DA (mg DA m^{-2}) or *Pseudo-nitzschia* cell abundance (cells m^{-2}) (See Trainer et al., 2009).

2.3.3 Sediment Traps

Sinking particulate samples were obtained from two moored Mark IV sediment traps deployed at 147 ± 2 and 509 ± 23 m located near the center of the SBB (34º14'N, 120º2'W) in a total water depth of ~ 590 m (Figure 2.1). In the shallow 147 m trap, samples for this study were collected from October 2009 – October 2011. Deep trap (509 m) sample collection began in August 1993 with data collected from 1993 to 2008 reported in Sekula-Wood et al. (2011), and data from 2009 - 2012 reported here. Gaps in sediment trap data are due mainly to trap clogging, failure to retrieve the sediment trap,

and to a much lesser extent, insufficient sample size because of very low mass flux. Trap deployments lasted approximately six months with each trap cup (n = 13) collecting sediment continuously for ~ two-week periods. The sample cups were deployed filled with filtered seawater containing a solution of 10% sodium azide and 1% sodium borate for sample preservation (Sekula-Wood et al., 2011). Sediment trap samples were analyzed for *Pseudo-nitzschia* cell abundance using the Utermöhl method described above (Hasle, 1978; Sekula-Wood et al., 2009). Particulate DA within freeze dried and ground sediment was extracted using 1.3 mL of 50% methanol and analyzed as detailed in Sekula-Wood et al. (2011, 2009). Sediment trap supernatant solutions were filtered and measured directly using the same process as the water column dDA samples described above. Total DA (tDA) is the sum of the supernatant and pDA within the sediment trap normalized for supernatant volume and sediment trap mass. Sediment trap fluxes of *Pseudo-nitzschia* and tDA were determined by multiplying their concentration by the total grams of sediment captured during the ~ two-week collection period into the 0.5 m^2 opening of each sediment trap and dividing by the number of days in the collection period.

2.3.4 Statistics

All statistical analyses were done using IBM SPSS Statistics Version 24. None of the dependent variables were normally distributed, and data transformations (e.g., Log(x+1), 1/x, √x, etc.) resulted in non-normal distributions. Because variances were not homogeneous and data were not normally distributed, significance testing required the use of non-parametric tests. For comparisons between non-upwelling and upwelling conditions, the Kruskal-Wallis test was used to determine significant differences, and the

level of significance was set at □ = 0.05. Correlations were determined using Spearman's rho testing, and the level of significance was conservatively set at □ = 0.01. Mann-Whitney U testing was conducted to determine differences between surface stations with a Bonferroni correction setting the significance level at □ < 0.0014. Linear regressions were performed to determine the mathematical relationships between pDA and dDA and tDA and *Pseudo-nitzschia* abundance.

2.4. Results

2.4.1 Water Column

In order to examine the role of upwelling on *Pseudo-nitzschia* abundance and DA toxicity, upwelling events were defined as the shoaling of the 12°C isotherm above 30 m at Station 4 (Figure 2.2). Note that the specific mechanisms that induce upwelling, e.g. wind direction and strength as well as mesoscale eddies, require a more detailed analysis of basin physics, such as cross shelf transport and eddy strength (e.g., Henderikx Freitas et al., 2016). These analyses are beyond the scope of the present study.

2.4.1.1 Surface waters

Bulk surface *Pseudo-nitzschia* cell abundances (< 5 m) along the SBB transect and at two shore-based sampling locations, Stearns Wharf and Goleta Pier (http://www.habmap.info/data.html, Figure 2.1), were highly variable, with concentrations ranging from below detection to > 3×10^6 cells L^{-1} (average $2.5 \times 10^5 \pm 4.9 \times 10^5$ cells L^{-1}) across the SBB and from below detection to 8×10^5 cells L^{-1} (average $4.1 \times 10^4 \pm 9.0 \times 10^4$ cells L^{-1}) at the piers (Table 1, Figure 2.3). While the timing of higher *Pseudo-nitzschia* cell abundances measured offshore were reflected in the pier measurements, absolute concentrations often differed by an order of magnitude. Adjacent

SBB transect stations often differed by more than an order of magnitude in *Pseudo-nitzschia* cell abundance as well (Figure 2.3A). Stearns Wharf *Pseudo-nitzschia* abundances are significantly lower (average ~ 4.3 x 10^5 cells L^{-1}) compared to Goleta Pier (average ~ 5.0 x 10^5 cells L^{-1}) (Mann Whitney U, $p < 0.001$), and both piers are lower on average than the offshore stations by at least a factor of three. Significant differences between piers and the offshore stations were only found at stations 4, 6, and 7 due to the high variability in offshore *Pseudo-nitzschia* concentrations (Mann Whitney U, $p < 0.001$). At Stearns Wharf and Goleta Pier, total *Pseudo-nitzschia* abundance and the wide class of *Pseudo-nitzschia* are significantly higher during upwelling versus non-upwelling time periods ($p < 0.05$). However, at the offshore stations, the high spatial and temporal variability in total *Pseudo-nitzschia* abundance resulted in no significant difference between upwelling and non-upwelling periods (Kruskal-Wallis $p > 0.05$) (Figure 2.4A). It is important to note that while seasonal rains are often associated with increased nutrients from river discharge (data not shown, ncdc.noaa.gov Severe Weather Data Inventory, daily precipitation records), they did not coincide with upwelling periods or with changes in *Pseudo-nitzschia* abundance or dDA and pDA concentrations (Kruskal-Wallis $p > 0.05$), similar to previous studies in the basin (Sekula-Wood et al., 2011; Henderikx Freitas et al., 2016). At the Goleta and Stearns Wharf piers, there were significantly higher pDA concentrations during upwelling versus non-upwelling periods, which resulted in a significantly higher cDA during upwelling as well (Kruskal-Wallis test $p < 0.05$,) (Figure 2.4). While the wide *Pseudo-nitzschia* were significantly correlated with pDA (Spearman's rho, $p < 0.01$, linear regression, $p < 0.05$, adj. $r^2 = 0.203$), narrow

Pseudo-nitzschia were not (spearman's rho, $p > 0.01$, linear regression $p > 0.05$, adj. $r^2 = -0.005$).

Particulate DA concentrations measured at Goleta Pier were significantly lower than those measured at either Stearns Wharf or the offshore stations (Mann-Whitney U, $p < 0.001$). Stearns Wharf pDA, however, showed no similar relationship, again due to the large variations in pDA concentrations measured. In the offshore stations, tDA surface water concentrations showed no significant differences between stations (Mann Whitney U, $p > 0.0013$) and concentrations were relatively evenly distributed between particulate (57.3 ± 34.8 %) and dissolved (42.7 ± 34.8 %) forms (average tDA = $7.8 \times 10^3 \pm 2.2 \times 10^4$ ng DA L^{-1}, ranging from below detection to 2.2×10^5 ng DA L^{-1}) (Figure 2.5A, Table 1). Similar to *Pseudo-nitzschia* cell abundance, surface tDA concentrations at the offshore stations were spatially and temporally variable with no seasonal or upwelling trends (Kruskal-Wallis, $p > 0.05$).

There is a significant correlation between tDA and *Pseudo-nitzschia* abundance in the offshore stations (Figure 2.5B, Spearman's rho, $r = 0.621$, $p < 0.01$), however, total *Pseudo-nitzschia* abundance is a poor predictor of tDA concentration (linear regression, adj. $r^2 = 0.025$, $p < 0.05$) Figure 2.5B) across all pier (regardless of the *Pseudo-nitzschia* group) and transect stations. There was no temporal offset between surface bulk *Pseudo-nitzschia* and tDA concentrations either at a specific station or across all stations over the sampling period. In contrast, pDA and dDA concentrations across all transect stations and depths are significantly correlated (Spearman's rho, $r = 0.831$, $p < 0.01$), and dDA is a strong predictor of pDA (linear regression, adj $r^2 = 0.896$ $p < 0.05$ Figure 2.5A).

Concentrations of cDA range from below detection to 1400 pg cell^{-1} with higher cellular DA concentrations associated with the transect stations (average across all offshore stations = 37 ±124 pg cell^{-1}) relative to Goleta Pier and Stearns Wharf (average across both piers = 18 ± 65 pg cell^{-1}) (Mann-Whitney U, $p < 0.05$) (Figures 3 and 4). There is no significant difference in mean cDA concentrations across the offshore stations or between the offshore stations and the piers (Mann Whitney U, $p < 0.001$). There is no difference between upwelling versus non-upwelling periods (Kruskal-Wallis, $p > 0.05$).

2.4.1.2 Depth distributions

High *Pseudo-nitzschia* abundances occurred in August 2009, July-December 2010, August 2012 and July 2013. At Station 4, *Pseudo-nitzschia* comprised > 50% of the microphytoplankton (20-200 µm) community. Moderately high *Pseudo-nitzschia* abundances (> 10^4 cells L^{-1}) were measured throughout the water column to depths as deep as 150 m multiple times during the sampling period (n = 6/23 at 150m), particularly when *Pseudo-nitzschia* abundance at the surface was high (Figure 2.6A). During upwelling periods, *Pseudo-nitzschia* abundance was generally greatest at the surface and decreased rapidly with depth. In contrast, during non-upwelling periods, average *Pseudo-nitzschia* abundances were lower at the surface, such that bulk abundances decreased more slowly with increasing depth (Figure 2.6A). *Pseudo-nitzschia* abundances were significantly lower during upwelling versus non-upwelling periods at 150 m (Kruskal-Wallis, $p < 0.05$).

At Station 4, the highest tDA concentrations (Figure 2.6) typically occurred in the upper 25 m, although high tDA concentrations (> 200 ng L^{-1}) were observed as deep as

100 m several times (n = 5/21 at 100 m) throughout the time-series (Figure 2.6). Both particulate DA and dDA concentrations were not significantly different during upwelling versus non-upwelling periods at any depth (Kruskal-Wallis $p > 0.05$) (Figure 2.4). Total DA concentrations were generally higher during upwelling periods (although not statistically significant due to high variability, Kruskal-Wallis $p > 0.05$) and rapidly decline with depth regardless of upwelling intensity (Figure 2.4D). Total DA concentrations also differ from *Pseudo-nitzschia* cell abundance in that peak tDA concentrations occurred both prior to (e.g., in August-September, 2010) and following (e.g., September, 2011) peaks in *Pseudo-nitzschia* cell abundance. Furthermore, not all instances of high *Pseudo-nitzschia* abundance resulted in an associated increase in tDA (n = 4, August 2009, February 2010, March 2010, November 2011 for high *Pseudo-nitzschia* cell abundance with low tDA concentrations) (Figure 2.6).

Cellular DA concentrations at Station 4 ranged from below detection to as high as 320 pg cell^{-1} (average 18 ± 46 pg cell^{-1}) and remained relatively constant down to 75 m, averaging 22 pg cell^{-1}, before declining to less than 6 pg cell^{-1} below 100 m (Figure 2.6). There was no significant difference between average cDA concentrations measured during upwelling versus non-upwelling periods above 150 m, (Kruskal-Wallis, $p > 0.05$, Figure 2.4F), but there is a significant difference at 150 m, where cDA concentrations measured during non-upwelling (9.4 pg cell^{-1}) were almost double those measured during upwelling (5.1 pg cell^{-1}) (Kruskal-Wallis $p < 0.05$).

2.4.2 Water column inventories and flux comparison

Temporal differences in sampling (one day versus ~ two weeks) makes comparisons between water column sampling and sediment trap concentrations and fluxes difficult. Nonetheless, comparisons were made in an attempt to identify specific processes influencing both data sets. The absolute magnitude of *Pseudo-nitzschia* cell abundance and tDA concentrations in the water column during a specific sampling interval were not significantly correlated with the concentrations and fluxes measured in either of the sediment traps. Less than 5% of water column inventories were captured per day (inventory divided by daily flux) in either trap throughout the sampling period (Figure 2.7).

2.4.3 Sediment Traps

During the study period, there are two significant periods of missing data from the 509 m trap due to clogging (April-Sept 2010 and July-Oct. 2011). This is not an uncommon occurrence and is often associated with high flux events that interfere with trap cup rotation (Sekula-wood et al., 2011). The average concentration of *Pseudo-nitzschia* in the 147 m trap was $7.2 \times 10^6 \pm 2.1 \times 10^7$ frustules gram sediment^{-1} and ranged from below detection to 1.03×10^8 frustules gram sediment $^{-1}$ (Figure 2.7). These concentrations are not significantly different than those measured in the 509 m trap, which averaged $8.7 \times 10^5 \pm 10^6$ frustules gram sediment $^{-1}$ and ranged from below detection to 9.5×10^6 frustules gram sediment $^{-1}$ (Kruskal-Wallis $p > 0.05$). Total DA concentrations in each trap were not significantly different and ranged from below detection to 79.9 µg tDA gram of sediment $^{-1}$ and averaged 7.4 ±16.5 and 6.8±14.1 µg tDA gram of sediment^{-1} in the 147 and 509 m sediment traps, respectively (Figure 2.7,

Table 1). It is important to note that DA degradation occurs in the sediment traps throughout deployment, such that sediment trap tDA concentrations may be underestimated by as much as 50% (Sekula-Wood et al., 2011). There was no relationship between sediment trap *Pseudo-nitzschia* abundance and DA concentrations.

Sediment trap fluxes varied considerably throughout the times-series, with the flux of *Pseudo-nitzschia* ranging from < 1000 to > 5.9 x 10^7 frustules m^{-2} d^{-1} and averaging 3.2 x 10^6 ± 10^7 frustules m^{-2} d^{-1} in the 147 m trap. Total DA in the 147 m trap ranged from < 0.01 to > 70 µg DA m^{-2} d^{-1} and averaged 4.9 ± 12.3 µg DA m^{-2} d^{-1}. The flux of *Pseudo-nitzschia* into the 509 m trap was considerably lower than that measured at shallower depths, ranging from < 1000 to > 1.5 x 10^7 frustules m^{-2} d^{-1} and averaging 1.3 x 10^6 ±3.1 x 10^6 frustules m^{-2} d^{-1} (Figure 2.7). In contrast, tDA fluxes showed an opposite trend, with higher tDA fluxes at depth, averaging 4.9 versus 13 µg tDA m^{-2} d^{-1}, but this difference was not significant given the high variability in the datasets (Kruskal-Wallis $p > 0.05$). Given the similarities in tDA concentrations between the two depths, differences in flux were almost entirely driven by the total mass flux (0.7 versus 1.7 g m^{-2} d^{-1} at 147 and 509 m, respectively).

Although data are limited, both traps show periods of high tDA and *Pseudo-nitzschia* fluxes in mid-winter and summer of each year (Figure 2.7). There was no significant difference between *Pseudo-nitzschia* concentrations or fluxes during upwelling versus non-upwelling in either trap (Kruskal-Wallis $p > 0.05$) when compared directly to surface upwelling periods. However, when the trap data was lagged two weeks behind the start of the upwelling period, *Pseudo-nitzschia* concentrations and fluxes were significantly higher during upwelling in the 509 m trap (Kruskal-Wallis, $p < 0.05$).

Total DA concentrations and fluxes had different trends. In the 147 m trap, tDA concentrations were significantly lower and fluxes were higher during upwelling versus non-upwelling (with no time lag), respectively (Kruskal-Wallis, $p < 0.05$). During non-upwelling, the average DA concentration was 8.7 µg tDA per g sediment and the average tDA flux was 8.1 µg DA m^{-2} day^{-1}. During upwelling, the average tDA concentration was lower, 6.4 µg per g sediment, and the average tDA flux was more than three times lower, 2.4 µg m^{-2} day^{-1}. When tDA concentrations and fluxes in 147 m trap were lagged relative to upwelling by two weeks, there was no significant difference in tDA fluxes between upwelling and non-upwelling periods, while tDA concentration differences remained (Krusal-Wallis, $p < 0.05$). Total DA concentrations and fluxes within the 509 m trap were not significantly different during upwelling versus non-upwelling either with or without time lags due to the high variability in the dataset (Kruskal-Wallis, $p > 0.05$).

2.5. Discussion

2.5.1 Water Column

Toxic *Pseudo-nitzschia* blooms occur worldwide and are commonly associated with eastern boundary currents, such as along the West Coast of the United States where upwelling of nutrient rich waters is supplemented by nutrients from riverine runoff and upwelling induced mesoscale circulation patterns that promote diatom growth (Horner et al., 2000; Marchetti et al., 2004; Anderson et al., 2006; Schnetzer et al., 2007; Trainer et al., 2009, 2012). Within the SBB, toxic *Pseudo-nitzschia* blooms have become a regular occurrence since they were first observed in 1998, when a widespread bloom resulted in the mass mortality of more than 400 sea lions (Scholin et al., 2000; Trainer et al., 2000). Since then, efforts to understand the mechanisms that foster toxic *Pseudo-nitzschia*

blooms have proliferated (e.g., see reviews by LeLong et al., 2012; Trainer et al., 2012), along with attempts to develop predictive models of when and where *Pseudo-nitzschia* blooms will occur (e.g., Anderson et al., 2009, 2011, 2016).

Numerous studies have linked bulk *Pseudo-nitzschia* abundance and growth rates along the western United States to increased nutrients supplied by seasonal upwelling conditions (e.g., Trainer et al., 2000; Kudela et al., 2005; Schnetzer et al., 2013; Du et al., 2016). In the SBB, the dominant species in the basin, *Pseudo-nitzschia australis* (Anderson et al., 2006; Sekula-Wood et al., 2011; Barron et al., 2013), is associated with the warming of cold, high salinity upwelled waters, and peaks in abundance late within the primary diatom bloom season (Anderson et al., 2009; Schnetzer et al., 2013). These increases in *Pseudo-nitzschia australis* abundance are further associated with a decline in nutrient availability in source waters (Bograd et al., 2015; Ryan et al. 2017) and warming ocean temperatures on longer time scales (McCabe et al., 2016; McKibben et al. 2017).

In this study, we observed wide temporal and spatial variations in bulk *Pseudo-nitzschia* abundance and spatial distributions that did not correspond with upwelling conditions. Instead, *Pseudo-nitzschia* were almost always present in the SBB with *Pseudo-nitzschia* generally occurring in the upper 20 m of the water column in a range of cellular abundances similar to those found in other studies in this area (e.g., Anderson et al., 2006; Schnetzer et al., 2013). The lack of seasonal differences in bulk *Pseudo-nitzschia* abundance may be due to climate induced warming of waters enabling blooms nearly year-round (Barron et al., 2013; McCabe et al., 2016; Mckibben et al., 2017) or due to biogeochemical changes in the ambient nutrient regime (i.e., low Si:N and N:P

ratios) that allow bulk *Pseudo-nitzschia* to maintain a robust population year round (Bograd et al. 2015).

Spatially, surface *Pseudo-nitzschia* abundances observed offshore rarely matched those measured in the pier-based sampling stations (Goleta and Stearns Wharf Piers) or even in adjacent transect stations, often differing by more than an order of magnitude. This is consistent with results from a skill assessment of the California Harmful Algae Risk Mapping (C-HARM) System that showed that weekly samples from Stearns Wharf were decoupled from the 3-km pixel predictions of blooms and DA concentrations (Anderson et al. 2016). It also supports the possibility that offshore *Pseudo-nitzschia* blooms that were forecasted by the model reflect conditions that are suitable for year-round *Pseudo-nitzschia* growth in offshore waters.

At least some of this nearshore - offshore difference may be attributed to the physical circulation patterns related to mesoscale eddies, cyclonic currents, and the progression of upwelling within the central SBB (Anderson et al., 2006; Brzezinski and Washburn, 2011) as well as potential diversity in *Pseudo-nitzschia* spp. For example, Bialonski et al. (2016) found that SBB circulation dynamics play a role in transporting phytoplankton from one area of the basin to another. While some of the sampling sites were considered sources of phytoplankton seed populations, the source areas changed seasonally and annually, suggesting that allocthonous sources may also influence *Pseudo-nitzschia* abundance. Given that there is some seasonality to the HAB pier monitoring dataset relative to the offshore Plumes and Blooms data, however, it may be that offshore waters, which have been previously undersampled, are revealing perennial populations that support bloom incubation.

The single depth profiles in the center of the SBB also reveal that *Pseudo-nitzschia* inhabit the entire mixed layer, with significant cell abundances (> 50,000 cells L^{-1}) occurring below the surface at 10-30 m in depth. Our measurements are likely underestimates, as it is possible that conventional bottle sampling may miss thin layers of high *Pseudo-nitzschia* cell abundance. The presence of these subsurface *Pseudo-nitzschia* support the hypothesis put forth by Seegers et al. (2015) that subsurface *Pseudo-nitzschia* could "seed" surface blooms following upwelling events. These "hidden" or "cryptic" blooms are prevalent worldwide, with thin layers of toxic *Pseudo-nitzschia* measured in nearby Monterey Bay at depths of 10-15 m (McManus et al., 2008; Timmerman et al., 2014). The presence of significant, deep *Pseudo-nitzschia* cell abundances (> 10^4 cells L^{-1}), at times reaching 150 m (our deepest water column sampling point) are almost always associated with high *Pseudo-nitzschia* abundance in overlying surface waters (n = 6). We therefore hypothesize that these deep *Pseudo-nitzschia* cells are likely the result of aggregation and flocculation (Alldredge and Gotschalk 1990), consistent with Timmerman et al. (2014), who further demonstrated that thin layers where dominated by diatom flocs, as opposed to single cells.

The toxicity of *Pseudo-nitzschia* within the SBB is more complex (Figures 3 and 6). Shore based tDA concentrations were consistently two to three orders of magnitude lower than those measured offshore (e.g., Nov. 2009 and Jul. 2012; Figure 2.3). While these average tDA concentrations were generally higher than those previously measured in this region, they were well within the range of reported tDA concentrations (Anderson et al., 2009; Schnetzer et al., 2013; McCabe et al., 2016). In the central SBB (Station 4), highest tDA concentrations occurred before (e.g., Aug. to Sept. 2010), during (June and

July 2011), and after (Oct. to Nov. 2009) the peak in bulk *Pseudo-nitzschia* cell abundance, with no relationship to seasonal upwelling. Furthermore, significant water column tDA concentrations (> 200 ng L^{-1}) were measured as deep as 100 m (Figure 2.6). These findings argue that bulk *Pseudo-nitzschia* cell abundance is a poor predictor of toxicity and that measuring DA concentrations independently of *Pseudo-nitzschia* abundance is needed, as DA may be present in the water column in the absence dense *Pseudo-nitzschia* at the surface, i.e., summer 2011.

Cellular DA concentrations varied considerably, with an average of 18.3 ± 43.6 pg $cell^{-1}$ at station 4 over all depths, and an average of 37 ± 124 pg $cell^{-1}$ at the surface stations. They were generally within the range of published values (0 - 117 pg $cell^{-1}$), although among the higher end of concentrations previously measured; the maximum cDA found here (1400 pg $cell^{-1}$) is higher than any previously published values (Baugh et al., 2006; Schnetzer et al., 2007; Anderson et al., 2009; Trainer et al., 2012; McCabe et al., 2016). However, unlike tDA or *Pseudo-nitzschia* abundance, cDA concentrations were relatively constant with increasing depth down to 75 m (Figure 2.6). Consistent with previous work, *Pseudo-nitzschia* toxicity in the SBB over our short sampling period appears to depend on a variety of factors other than bulk *Pseudo-nitzschia* cell abundance (e.g., Lelong et al., 2012). While the exact mechanisms that promote *Pseudo-nitzschia* toxicity are complex (LeLong et al., 2012), the majority of research along the West Coast of the United States argues that increasing toxicity occurs in response to increasing physiological stress and is often associated with the stationary phase of cell growth (e.g., see review by Trainer et al., 2012). In laboratory cultures, Schnetzer et al. (2016) showed that cellular toxicity of *Pseudo-nitzschia* increased by an order of magnitude as the bloom

progressed from the exponential growth phase to senescence and marine snow formation (See Surface to Depth Transport). Environmental factors such as temperature likely facilitate cell toxicity as well, although it can be difficult to separate temperature from nutrients and growth phase. For example, Anderson et al. (2008) found diatom dominant assemblages and increased bulk *Pseudo-nitzschia* abundances occur at the end of the upwelling season in the Santa Barbara Channel, when nutrients were still plentiful, but waters were warming. In follow-up studies, Anderson et al. (2009) found that models driven by lower Si:N ratios, which occur towards the end of a diatom bloom, provided the best predictor of DA toxicity in the SBB. In their study of the largest DA-producing bloom measured along the western United States, McCabe et al. (2016) found that the *Pseudo-nitzschia* bloom was initiated by nutrients from upwelled waters and then sustained by warmer temperatures once upwelling ceased. Similar results have been found internationally. Off the coast of Namibia, Louw et al. (2017) found highest bulk *Pseudo-nitzschia* abundances to occur at the more moderate temperatures following upwelling events and Durson et al. (2018) found that DA concentrations in a Turkish estuary increased with increasing temperature. Species and strain identification of *Pseudo-nitzschia* spp. were beyond the scope of this work, but the variation in tDA production by species and strains likely plays an important role in the decoupling observed between tDA concentrations and bulk *Pseudo-nitzschia* biomass in the SBB during our study period (Thessen et al., 2009; Trainer et al., 2012; Martin-Jezequel et al., 2015). While highly toxigenic strains of *P. australis* and *P. multiseries* have been identified in SBB blooms (Sekula-Wood et al., 2011; Trainer et al., 2012), so have less toxigenic species, e.g., *P. fraudulenta* (Trainer et al., 2012). Using samples from the

SBB, Seubert et al. (2013) found that differentiating between these two size classes, which is possible via light microscopy, provides a rough approximation of the presence of highly toxic versus less toxic or non-toxic species when more precise methods of species identification are not available. At the pier stations, where size classes were used to differentiate between rarely toxic and usually toxic cells, wide *Pseudo-nitzschia* (often toxic, e.g., *P. australis*) was significantly correlated with pDA (Spearman's rho, $p<0.01$) while narrow *Pseudo-nitzschia* (rarely toxic, e.g., *P. delicatissima*) was not (Spearman's rho, $p>0.01$). In nearby San Pedro Channel, Smith et al. (2018) found similar results. While bulk *Pseudo-nitzschia* abundance increased after medium strength upwelling intervals, pDA concentrations did not. Rather, Smith et al. (2018) found that DA concentrations were strongly influenced by *Pseudo-nitzschia* speciation, with higher pDA concentrations occurring with more toxigenic species (based on ribosomal analyses) towards the end of an upwelling event when silicic acid concentrations had declined (along with other important nutrients). In the SBB, the relative dominance of the wide and narrow *Pseudo-nitzschia* varied temporally. However, only the abundance of the wide size class was significantly higher during upwelling. These results are therefore consistent with previous work in the SBB and elsewhere linking the appearance of potentially toxic *Pseudo-nitzschia* with upwelling to post-upwelling conditions, at least in the nearshore (e.g., Seubert et al. 2013).

Particulate DA concentrations and toxic *Pseudo-nitzschia* have been the focus of most of the extant studies due to potential impacts on human health due to the bioaccumulation of toxic particles by shellfish populations. However, our results confirm that dDA is a significant component of the tDA pool; tDA concentrations were almost

evenly distributed between dissolved and particulate phases (Figure 2.5). Previous investigations of dDA and pDA concentrations suggest that their distribution may be species-dependent. In a study of a *P. cuspidata* bloom off the coast of Washington state, Trainer et al. (2009) found that partitioning between pDA and dDA was highly variable. In contrast, Baugh et al. (2006) found that more toxic *Pseudo-nitzschia* spp. produced significantly higher pDA concentrations relative to dDA. In field samples containing ten times lower *P. australis* (highly toxigenic) than *P. delicatisssima* (barely toxigenic), pDA concentrations were half that of dDA concentrations (Baugh et al. 2006). In field samples with approximately equal concentrations of *P. australis* and *P. delicatissima*, pDA and dDA concentrations were similar (Baugh et al. 2006). While variations in the pDA:dDA ratio did occur in our study (Figure 2.5A) and may be due to changes in the specific mixture of *Pseudo-nitzschia* species present or other factors affecting bloom toxicity, the strong linear regression between dDA and pDA (adj $r^2 = 0.896$, $p < 0.05$) indicates that variations are relatively small, regardless of when the samples were collected or the species present. Our results of a near equal distribution of pDA and dDA within the SBB during our field campaign therefore suggests that *Pseudo-nitzschia* were likely comprised of a more even mixture of toxic and less toxic *Pseudo-nitzschia* spp., consistent with the pier results.

The existence of high amounts of dDA throughout the upper 75 m of the water column that persists for several months is an intriguing finding (Figure 2.6). Once produced, DA is water-soluble and has little to no particle reactivity at the particle loads typical of the marine water column (Lail et al., 2007). Dissolved DA may photochemically degrade with degradation rates declining rapidly with depth (Bates et

al., 2003; Boullion et al., 2006). The rate of degradation, however, depends on the depth of light penetration, temperature, and potentially dissolved organic matter and iron concentrations, (Bouillion et al., 2006; Fisher et al., 2006), such that degradation rates exponentially decrease with increasing water depth and are essentially negligible by 5 m due to light attenuation (Bouillion et al., 2006). Bacteria also likely degrade DA depending on the bacterial assemblages present. However, information is limited as studies either focus on bacteria associated with specific species of *Pseudo-nitzschia*, e.g., *P. multiseries* (Hagström et al., 2007; Stewart, 2008; Sison-Mangus et al., 2016), or with higher trophic levels, i.e., bacteria from blue mussels, sea scallops, and anchovies (Stewart et al., 1998; Stewart, 2008). Bacterial degradation rates are likely underestimated, as current studies of photochemical versus bacterial degradation do not completely eliminate the influence of the other pathway (e.g., Hagström et al., 2007). Our results suggest that while dDA may undergo degradation, significant dDA concentrations remain present throughout the upper water column (Figures 5 and 6). The ecosystem impact of dDA remains ambiguous, specifically the potential effect on feeding behavior, bioaccumulation, or the health of higher trophic-level animals. Current research has shown dDA exposure can cause developmental defects in zebra fish and scallops (Liu et al., 2007; Hong et al., 2015), and lower krill grazing rates (Bargu et al., 2006). Van Meerssche and Pinkney (2017) found that dDA, in concert with salinity, inhibits growth of some phytoplankton groups in an allelopathic manner. Regardless of the mechanism and potential direct impact on biota, dDA concentrations may provide an indication of the *Pseudo-nitzschia* spp. present in the SBB water column and potential toxicity, i.e., the pDA available for bioaccumulation. These results are particularly valuable given the

recent developments of *in situ* techniques for rapid monitoring of dDA concentrations (Lane et al., 2010; Colas et al., 2016).

2.5.2 Surface to depth transport

The absolute magnitudes of *Pseudo-nitzschia* and tDA inventories in the water column as well as the concentrations and fluxes measured in the sediment traps varied significantly, with less than 5% of water column inventories captured on a daily basis in either sediment trap throughout the sampling period. These results are lower than that of Krause et al. (2013) who found that, on average, 10% of the biogenic silica (which includes *Pseudo-nitzschia* frustules) measured in the upper 75 m within the SBB is exported to the deep sediment trap on a daily basis. Lower biogenic silica export efficiencies are likely related to plankton composition. While *Pseudo-nitzschia* may dominate microphytoplankton communities during a bloom event, they are not the only diatom or siliceous organisms present in the system. For example, *Chaetoceros* spp., *Rhizosolenia*-related *spp.*, and silicoflagellates are also common during SBB blooms (Shipe and Brzezinski, 2001; Venrick et al., 2008; Barron et al., 2013). Furthermore, *Pseudo-nitzschia* spp. are generally lightly silicified and therefore subject to more rapid and extensive dissolution upon cell senescence and death (Marchetti et al., 2004; Lundholm et al., 2010). Remineralization of *Pseudo-nitzschia* is supported by the large-scale difference in *Pseudo-nitzschia* frustule abundance between the two sediment traps, with deep traps containing *Pseudo-nitzschia* frustule concentrations an order of magnitude lower than those observed in the shallow trap.

Previous work in the SBB has demonstrated strong seasonal differences in the flux of nutrients, carbon, and opal to the deepest trap, with significantly higher fluxes

occurring during upwelling ($p < 0.001$, Sekula-Wood et al., 2012), consistent with peak plankton biomass. Krause et al. (2013) further found that peaks in opal fluxes in the 509 m sediment trap lagged peaks in upper water column opal (diatom) inventories by two weeks to two months. Sekula-Wood et al. (2009), however, found no such lag between bulk surface water *Pseudo-nitzschia* abundance and tDA concentrations and fluxes measured as deep at 800 m in the SBB and San Pedro Basin, and argued for rapid transport, with particle sinking rates in excess of 100 m d^{-1}.

In this study, there was no correlation between *Pseudo-nitzschia* water column inventories and *Pseudo-nitzschia* fluxes measured in either of the sediment traps when compared in real time (Spearman's rho, $p > 0.01$). However, there was a significant difference between upwelling and non-upwelling *Pseudo-nitzschia* concentration and flux when a two-week delay was imposed on the 509 m sediment trap data, similar to the difference seen in the water column at 150 m (Kruskal-Wallis $p < 0.05$). There were also significant differences (Kruskal-Wallis, $p < 0.05$) between upwelling and non-upwelling *Pseudo-nitzschia* fluxes and abundances when the deeper trap was lagged by one moth and, to a lesser extent, two months. Hence, our results are consistent with Krause et al. (2003) and Sekula-Wood et al. (2009) in that *Pseudo-nitzschia* fluxes are rapidly transported to depth, but on average, bulk sinking rates are closer to or less than 50 m d^{-1} during this study.

In contrast, tDA concentrations in the upper sediment trap were significantly lower and fluxes were higher during upwelling versus non-upwelling (with no time lag), respectively (Kruskal-Wallis, $p < 0.05$). Total DA concentrations and fluxes within the 509 m trap, however, were not significantly different during upwelling versus non-

upwelling either with or without time lags due to the high variability in the dataset (Kruskal-Wallis, $p > 0.05$).

The difference in water column export efficiency between biogenic silica, *Pseudo-nitzschia*, and DA in the sediment traps likely occurs for several reasons including: spatial and temporal heterogeneity, variations in remineralization patterns, and issues associated with water column and sediment trap collection methods. First and foremost, spatial sampling of the SBB as a whole suggests that single day and point depth profiles do not capture the full temporal and spatial variability of tDA and *Pseudo-nitzschia* cell abundance occurring in the SBB. For example, *Pseudo-nitzschia* blooms form aggregate layers below the surface along isopycnals that persist on the order of days to weeks (Rines et al., 2002; Timmerman et al., 2014). As stated earlier, these thin layers easily missed by conventional water column sampling.

It is also possible that subsurface *Pseudo-nitzschia* are horizontally advected to other areas of the basin before reaching the sediment, similar to how surface blooms can be transported horizontally (see section 5.1). The SBB is host to an array of complex circulation patterns that have the potential to transport blooms from one area of the basin to another, including mesoscale eddies and wind-induced cross-shelf transport (Anderson et al., 2006; Brzezinski and Washburn, 2011; Bialonski et al., 2016). Horizontal advection of blooms could therefore decouple upper water column *Pseudo-nitzschia* and tDA from those measured in the sediment traps located directly below.

Differences in water column inventories and fluxes into the 147 and 509 m traps and between traps may also be due to variations in trap collection area and efficiency.

Shallow traps suffer from hydrodynamic effects associated with advective shear of water flow over the trap surface (e.g., Buesseler et al., 2007). While the SBB traps use baffles to reduce this sheer, both under and over collection of trap material may occur. Due to the depth difference between the surface and deep traps, the deep trap has a collection area two to four times larger depending on where in the upper water column particles originate. Given the spatial heterogeneity observed across the SBB, it is quite possible that the surface and bottom traps collect different material. This is most evident in the tDA. While tDA concentrations are similar between trap depths, tDA fluxes into the deeper 509 m trap, (12.9 µg DA m^{-2} d^{-1}) were almost three times higher, than that measured at 147 m and were almost entirely driven by differences in total mass flux (0.7 versus 1.7 g m^{-2} d^{-1} at 147 and 509 m, respectively). Krause et al. (2013) argued that a significant fraction of the biogenic silica flux measured in the deepest SBB trap originated from outside of the SBB and was likely advected into the SBB via strong and seasonally changing coastal currents. Unfortunately, our limited data set does not allow us to differentiate external versus locally sourced sinking particles.

Pseudo-nitzschia fluxes decrease by almost an order of magnitude at depth relative to that measured in the surface. This suggests that either bulk *Pseudo-nitzschia spp.* are much more rapidly remineralized than particle-associated DA or that toxic *Pseudo-nitzschia* are much more efficiently exported, perhaps through repackaging in rapidly sinking zooplankton fecal pellets (Miesner et al., 2016). In addition, *Pseudo-nitzschia* also produce transparent exopolymers (TEP) during physiological stress and bloom decline (Gotschalk and Alldredge, 1989; Drapeau et al., 1994; Engel, 2000). TEP is a critical component of diatom flocculation and the formation of aggregates, a key

precursor to sinking (e.g., Passow et al. 1994). A recent laboratory study by Schnetzer et al. (2016) found that DA production within *P. australis* occurred rapidly during marine snow formation and in response to N stress, with pDA loss rates of less than 2% d^{-1}. Thus, we argue that toxic *Pseudo-nitzschia* may also be more effectively transported to depth within the SBB due to the similar mechanisms that promote DA and marine snow formation.

Although < 5% of the water column DA inventory sinks to depth on a daily basis, sinking particle concentrations and fluxes are still cause for environmental concern. Total DA concentrations in the 147 and 509 m sediment traps averaged 6.8 to 7.4 µg tDA gram of $sediment^{-1}$, with six events exceeding 20 µg per g sediment between January 2009 and June 2012. Again, this is considered a minimum estimate as DA is known to degrade in sediment trap cups (Sekula-Wood et al., 2011). Thus, sinking particles laden with DA are a likely source of the toxin to pelagic and benthic food webs even when no surface *Pseudo-nitzschia* blooms have been observed (e.g., Vigilant and Silver, 2007; Goldstein et al., 2008; Kvitek et al., 2008, McCabe et al. 2016). The most dramatic example of such benthic contamination was observed in the closure of the Dungeness and rock crab fisheries along the U.S. West Coast during the 2015-2016 season due to high DA levels in crab tissues. At least $49 million dollars in revenue was lost in California alone (Callahan, 2016). Mitigating losses due to such closures is a key goal of harmful algal bloom analysts and policy makers.

2.6. Conclusions

Pseudo-nitzschia blooms occur worldwide, and as blooms increase in frequency and new species are described, it has become increasingly important to have effective tools for monitoring and modeling toxic blooms and their impact on ecosystems and economies. Previous work has shown that toxic *Pseudo-nitzschia* blooms typically occur immediately following coastal upwelling events throughout the world, in Southern Africa, Western Europe, South America and the United States (Trainer et al., 2012 Schnetzer et al., 2013; Husson et al., 2016; Louw et al., 2017; McKibben et al., 2017; Odebrecht et al., 2001). In this study, bulk *Pseudo-nitzschia* concentrations are spatially and temporally heterogeneous and are always present in the SBB. Furthermore, bulk *Pseudo-nitzschia* blooms were not significantly correlated with upwelling versus non-upwelling conditions. While tDA concentrations tended to be higher during upwelling conditions and there was a significant correlation between tDA and *Pseudo-nitzschia* abundance in offshore waters, total *Pseudo-nitzschia* abundance was a poor predictor of tDA concentration across all stations. These results, combined with the *Pseudo-nitzschia* size classifications measured at the SCCOOS/HABMAP pier stations indicates that a variety of *Pseudo-nitzschia* spp. exist in the SBB, and that variability at the species and strain level likely drives toxicity in response to a suite of environmental conditions, such as upwelling, that are complicated by bloom stage.

This study contributes to the growing body of evidence that dDA is significant and should not be ignored. *Pseudo-nitzschia* blooms and DA concentrations were often found throughout the upper water column, with significant water column DA concentrations measured at depths as deep as 150 m. The combination of relatively high

pDA and high concentrations of dDA supports the argument that DA in all phases should be considered in studies of DA allelopathic and ecosystem effects. Given the predictable partitioning of DA between particulate and dissolved phases, dDA may further serve as an indicator of toxigenic *Pseudo-nitzschia* spp. presence when no other measurements are available. Despite decoupled water column inventory and sediment trap measurements, the flux of DA to depth is relatively rapid, with minimal degradation as particles sink through the water column. We argue that this flux is likely due to the formation of toxic marine snow that occurs with bloom senescence and results in significant DA export to the seafloor. Our work adds to the growing body of literature on domoic acid toxicity in marine ecosystems and highlights the necessity of measuring both dissolved and particulate DA forms, *Pseudo-nitzschia* spp., and water column measurements below surface. Although only a small fraction of DA produced in the water column reaches the seafloor, our results confirm that concentrations remain significantly high that monitoring benthic organisms in this region should occur regularly.

2.7. Acknowledgements

We wish to thank the Santa Barbara Coastal LTER and the California Coastal Ecosystem LTER program for their support of the sediment traps and National Science Foundation OCE Grants: OCE 0850425 (CBN). We also wish to thank Nathalie Guillocheau and Sarah Amiri for assistance collecting water column samples on Plumes and Blooms cruises, Dr. Mark Brzezinski, his laboratory and the Southern California Coastal Ocean Observing System (SCCOOS), for *Pseudo-nitzschia* and particulate DA data from Goleta Pier and Stearns Wharf, Dr. Dave Siegel and his laboratory for allowing

us to participate on cruises in his Plumes and Blooms program, and Eric Tappa for assistance in sediment trap deployment and recovery and ancillary sediment trap analyses. BU was supported by a University of South Carolina Presidential Fellowship.

2.8 References

Anderson, C.R., Brzezinski, M.A., Washburn, L., Kudela, R., 2006. Circulation and environmental conditions during a toxigenic Pseudo-nitzschia australis bloom in the Santa Barbara Channel, California. Mar. Ecol. Prog. Ser. 327, 119–133. doi:10.3354/meps327119

Anderson, C.R., Siegel, D.A., Kudela, R.M., Brzezinski, M.A., 2009. Empirical models of toxigenic Pseudo-nitzschia blooms: Potential use as a remote detection tool in the Santa Barbara Channel. Harmful Algae 8, 478–492. doi:10.1016/j.hal.2008.10.005

Bargu, S., Powell, C., Coale, S., Busman, M., Doucette, G., Silver, M., 2002. Domoic acid detection in krill: a potential vector in marine food webs. Mar. Ecol. Prog. Ser. 237, 209–219. doi:10.3354/meps237209

Bouillon, R.-C., Knierim, T.L., Kieber, R.J., Skrabal, S. a., Wright, J.L.C., 2006. Photodegradation of the algal toxin domoic acid in natural water matrices. Limnol. Oceanogr. 51, 321–330. doi:10.4319/lo.2006.51.1.0321

Costa, L.G., Giordano, G., Faustman, E.M., 2010. Domoic acid as a developmental neurotoxin. Neurotoxicology 31, 409–23. doi:10.1016/j.neuro.2010.05.003

Goldstein, T., Mazet, J. a K., Zabka, T.S., Langlois, G., Colegrove, K.M., Silver, M., Bargu, S., Van Dolah, F., Leighfield, T., Conrad, P. a, Barakos, J., Williams, D.C., Dennison, S., Haulena, M., Gulland, F.M.D., 2008. Novel symptomatology and changing epidemiology of domoic acid toxicosis in California sea lions (Zalophus californianus): an increasing risk to marine mammal health. Proc. Biol. Sci. 275, 267–76. doi:10.1098/rspb.2007.1221

Hagström, J. a., Granéli, E., Maneiro, I., Barreiro, A., Petermann, A., Svensen, C., 2007.

Release and degradation of amnesic shellfish poison from decaying Pseudo-nitzschia multiseries in presence of bacteria and organic matter. Harmful Algae 6, 175–188. doi:10.1016/j.hal.2006.08.002

Lane, J.Q., Raimondi, P.T., Kudela, R.M., 2009. Development of a logistic regression model for the prediction of toxigenic pseudo-nitzschia blooms in monterey bay, California. Mar. Ecol. Prog. Ser. 383, 37–51. doi:10.3354/meps07999

Lefebvre, K. a., Robertson, A., Frame, E.R., Colegrove, K.M., Nance, S., Baugh, K. a., Wiedenhoft, H., Gulland, F.M.D., 2010. Clinical signs and histopathology associated with domoic acid poisoning in northern fur seals (Callorhinus ursinus) and comparison of toxin detection methods. Harmful Algae 9, 374–383. doi:10.1016/j.hal.2010.01.007

Lelong, A., Hegaret, H., Soudant, Ph., Bates, S.S., 2012. Pseudo-nitzschia (Bacillariophyceae) species , domoic acid and amnesic shellfish poisoning : revisiting previous paradigms. Phycologia 51, 168–216. doi:10.2216/11-37

Schnetzer, a., Jones, B.H., Schaffner, R. a., Cetinic, I., Fitzpatrick, E., Miller, P.E., Seubert, E.L., Caron, D. a., 2013. Coastal upwelling linked to toxic Pseudo-nitzschia australis blooms in Los Angeles coastal waters, 2005-2007. J. Plankton Res. 35, 1080–1092. doi:10.1093/plankt/fbt051

Schnetzer, A., Miller, P.E., Schaffner, R. a., Stauffer, B. a., Jones, B.H., Weisberg, S.B., DiGiacomo, P.M., Berelson, W.M., Caron, D. a., 2007. Blooms of Pseudo-nitzschia and domoic acid in the San Pedro Channel and Los Angeles harbor areas of the Southern California Bight, 2003–2004. Harmful Algae 6, 372–387. doi:10.1016/j.hal.2006.11.004

Scholin, C.A., Gulland, F., Doucette, G.J., Benson, S., Busman, M., Chavez, F.P., Cordaro, J., Delong, R., Vogelaere, A. De, Harvey, J., Haulena, M., Lefebvre, K., Lipscomb, T., Loscutoff, S., Lowenstine, L.J., Marin III, R., Miller, P.E., Mclellan, W.A., Moeller, P.D.R., Powell, C.L., Rowles, T., Silvagni, P., Silver, M., Spraker, T., Trainer, V., Dolah, F.M. Van, 2000. Mortality of sea lions along the central California coast linked to a toxic diatom bloom. Lett. to Nat. 403, 80–84.

Sekula-Wood, E., Schnetzer, A., Benitez-Nelson, C.R., Anderson, C., Berelson, W.M., Brzezinski, M. a., Burns, J.M., Caron, D. a., Cetinic, I., Ferry, J.L., Fitzpatrick, E., Jones, B.H., Miller, P.E., Morton, S.L., Schaffner, R. a., Siegel, D. a., Thunell, R., 2009. Rapid downward transport of the neurotoxin domoic acid in coastal waters. Nat. Geosci. 2, 272–275. doi:10.1038/ngeo472

Tatters, A.O., Fu, F.X., Hutchins, D.A., 2012. High CO 2 and silicate limitation synergistically increase the toxicity of pseudo-nitzschia fraudulenta. PLoS One 7. doi:10.1371/journal.pone.0032116

Timmerman, A.H.V., McManus, M. a., Cheriton, O.M., Cowen, R.K., Greer, A.T., Kudela, R.M., Ruttenberg, K., Sevadjian, J., 2014. Hidden thin layers of toxic diatoms in a coastal bay. Deep Sea Res. Part II Top. Stud. Oceanogr. 101, 129–140. doi:10.1016/j.dsr2.2013.05.030

Trainer, V.L., Adams, N.G., Bill, B.D., Stehr, C.M., Wekell, J.C., Moeller, P., Busman, M., Woodruff, D., Helena, M., Sellner, K., Cordaro, J., Thomas, N., Lowenstein, L., Chec-, M., Lefebvre, K., Reidarson, T., Langlois, G., 2000. Domoic acid production near California coastal upwelling zones , June 1998. Limnol. Oceanogr. 45, 1818–1833.

Trainer, V.L., Bates, S.S., Lundholm, N., Thessen, A.E., Cochlan, W.P., Adams, N.G., Trick, C.G., 2012. Pseudo-nitzschia physiological ecology, phylogeny, toxicity, monitoring and impacts on ecosystem health. Harmful Algae 14, 271–300. doi:10.1016/j.hal.2011.10.025

Watanabe, K.H., Andersen, M.E., Basu, N., Carvan, M.J., Crofton, K.M., King, K. a, Suñol, C., Tiffany-Castiglioni, E., Schultz, I.R., 2011. Defining and modeling known adverse outcome pathways: Domoic acid and neuronal signaling as a case study. Environ. Toxicol. Chem. 30, 9–21. doi:10.1002/etc.373

Wells, M.L., Trick, C.G., Cochlan, W.P., Hughes, M.P., Trainer, V.L., 2005. Domoic acid: The synergy of iron, copper, and the toxicity of diatoms. Limnol. Oceanogr. 50, 1908–1917. doi:10.4319/lo.2005.50.6.1908

Table 2.1. Table of descriptive statistics for surface stations and for station 4 water column profile depths.

		N	Minimum	Maximum	Mean	Stnd. Dev.
Pier Stations	Total *Pseudo-nitzschia* (cells L^{-1})	465	BD	8.03 X 10^5	4.08 X 10^4	8.97 X 10^4
	P. delicatissima (cells L^{-1})	463	BD	7.86 X 10^5	2.23 X 10^4	7.57 X 10^4
	P. seriata (cells L^{-1})	463	BD	3.77 X 10^5	1.86 X 10^4	4.74 X 10^4
	pDA (ng L^{-1})	193	BD	9.33 X 10^3	409	1.04 X 10^3
	cDA (pg $cell^{-1}$)	182	BD	833	17.6	65.2
	P. delicatissima DA (pg $cell^{-1}$)	144	BD	2.14 X 10^3	92.7	274
	P. seriata DA (pg $cell^{-1}$)	149	BD	833	26.5	72.7
Surface Stations (1-7)	*Pseudo-nitzschia* (cells L^{-1})	223	BD	3.56 X 10^6	2.45 X 10^5	4.94 X 10^5
	Pseudo-nitzschia % of Total Microphytoplankton	223	BD	135%	26.30%	26.30%
	Total Microphytoplankton (cells L^{-1})	223	5.64 X 10^3	6.75 X 10^6	8.00 X 10^5	1.04 X 10^6
	Chl *a* (ng L^{-1})	251	83.4	2.76 X 10^4	2.90 X 10^3	3.31 X 10^3
	tDA (ng L^{-1})	235	BD	2.23 X 10^5	7.82 X 10^3	2.22 X 10^4
	pDA (ng L^{-1})	224	BD	1.10 X 10^5	3.65 X 10^3	1.07 X 10^4
	dDA (ng L^{-1})	233	BD	1.13 X 10^5	4.38 X 10^3	1.21 X 10^4
	cDA (pg $cell^{-1}$)	203	BD	1.44 X 10^3	37	124
Station 4 (0-150m)	*Pseudo-nitzschia* (cells L^{-1})	178	BD	3.83 X 10^6	1.48 X 10^5	4.78 X 10^5
	Pseudo-nitzschia % of Total Microphytoplankton	178	BD	181%	22.40%	28.50%
	Total Microphytoplankton (cells L^{-1})	178	3.60 X 10^3	5.11 X 10^6	5.05 X 10^5	8.35 X 10^5

	Chl *a* (ng L^{-1})	187	20	1.18 X 10^4	2.22 X 10^3	2.38 X 10^3
	tDA (ng L^{-1})	243	BD	4.27 X 10^4	2.69 X 10^3	6.81 X 10^3
	pDA (ng L^{-1})	234	BD	2.18 X 10^4	1.17 X 10^3	3.12 X 10^3
	dDA (ng L^{-1})	242	BD	2.61 X 10^4	1.58 X 10^3	4.02 X 10^3
	cDA(pg $cell^{-1}$)	159	BD	323	18.3	45.6
147m Trap	*Pseudo-nitzschia* (cells g $sed.^{-1}$).	52	BD	1.03 X 10^8	7.23 X 10^6	2.10 X 10^7
	Pseudo-nitzschia flux (cells m^{-2} day^{-1})	52	BD	6.00 X 10^7	3.20 X 10^6	1.04 X 10^7
	DA concentration (µg g $sed.^{-1}$)	52	BD	79.9	7.39	16.5
	DA flux (µg m^{-2} day^{-1})	52	BD	70.8	4.91	12.3
509m Trap	*Pseudo-nitzschia* (cells g $sed.^{-1}$).	52	BD	9.54 X 10^6	8.65 X 10^5	1.98 X 10^6
	Pseudo-nitzschia flux (cells m^{-2} day^{-1})	52	BD	1.48 X 10^7	1.30 X 10^6	3.06 X 10^6
	DA concentration (µg g $sed.^{-1}$)	33	BD	58.4	6.77	14.1
	DA flux (µg m^{-2} day^{-1})	33	BD	139	12.9	28.2

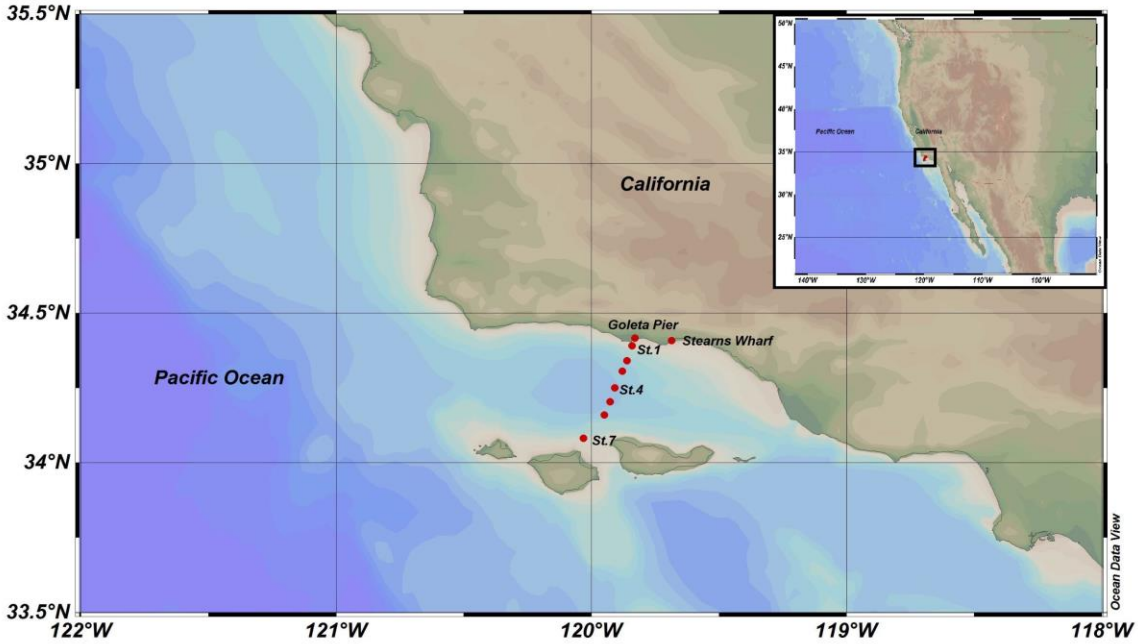

Figure 2.1Map of station locations in the Santa Barbara Basin. Stars indicate pier stations. Red circles indicate offshore stations and the yellow triangle denotes the location of the sediment traps.

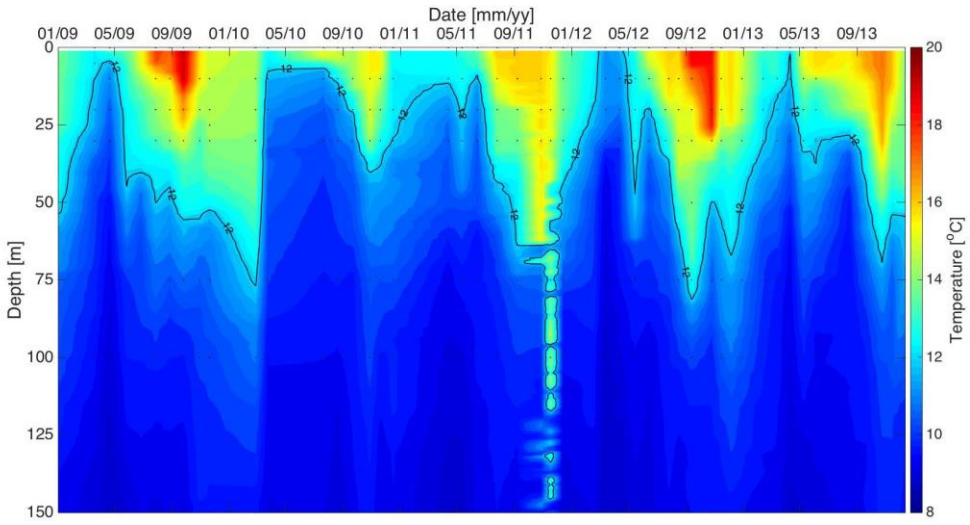

Figure 2.2 Temperature profiles throughout the study period at station 4. The contour line indicates the 12oC isotherm used to define upwelling when it shoals above 30 m as depicted by the dashed line.

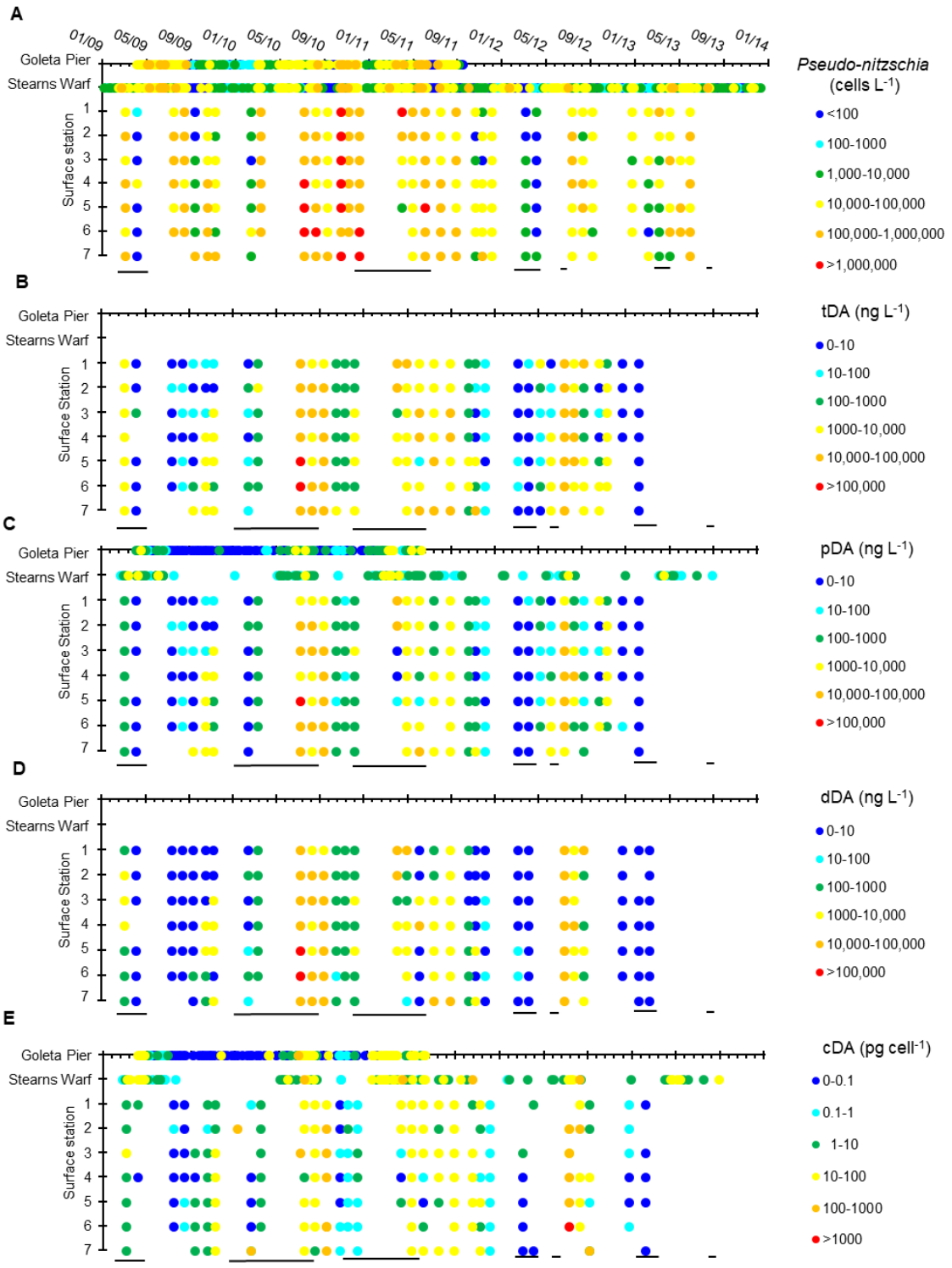

Figure 2.3 Pseudo-nitzschia concentrations (A), pDA concentrations (B), cDA concentrations, (C), dDA concentrations (D), and tDA concentrations (E)at pier and surface stations across the SBB from 2009-2013. Upwelling periods (12^{o}C isotherm shoals above 30m) are identified by dark lines located underneath each panel.

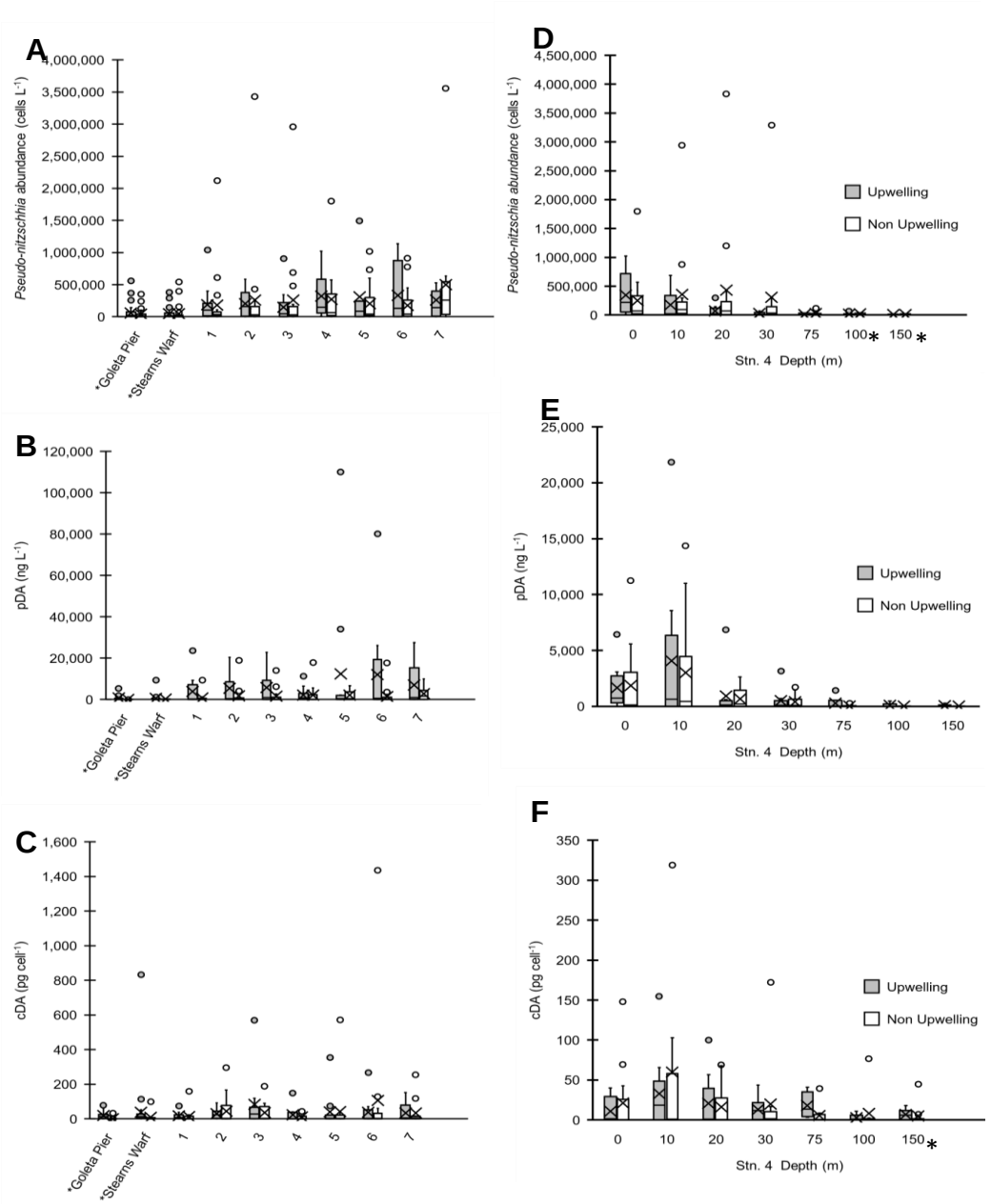

Figure 2.4 Box and whisker plots of *Pseudo-nitzschia* abundances at pier and surface stations (A) pDA concentrations at pier and surface stations (B) and cDA concentrations at pier and surface stations (C), station 4 Pseudo-nitzschia abundances with depth(D), station 4 pDA concentrations with depth (E) and Station 4 cDA concentrations with depth in the SBB during upwelling (shaded) and non-upwelling periods (open). X indicates the average, the horizontal bar indicates the median, the box represents the 2nd and 3rd quartiles, and the vertical bars indicate the 1st (lower) and 4th (upper) quartiles. Circles indicate statistical outliers that were included in the data because they are valid data points* indicates significant difference between upwelling and non-upwelling (Kruskal-wallis, $p < 0.05$).

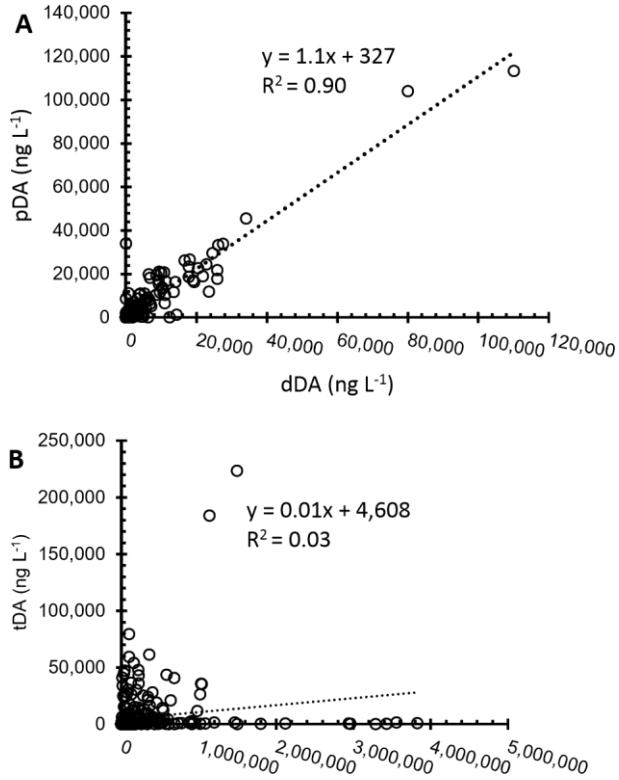

Figure 2.5 Plot of tDA vs. Pseudo-nitzschia abundance dDA vs. pDA (A) and tDA vs. *Pseudo-nitzschia* abundance (B) for stations 1-7 at all depths.

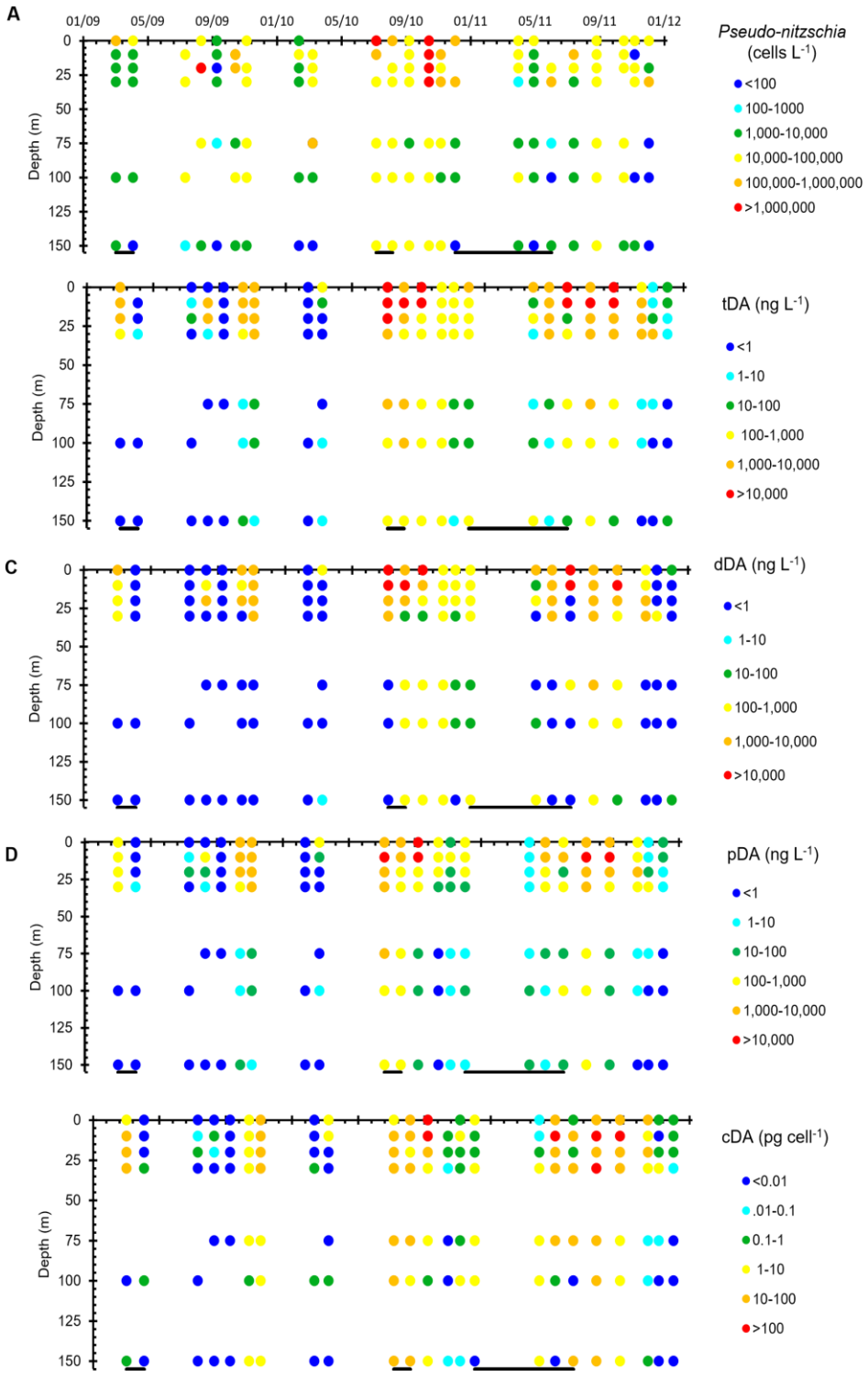

Figure 2.6 Pseudo-nitzschia abundances (A), dDA concentrations (B), pDA concentrations (C) cDA concentrations (D) and tDA concentrations (E) from 0-150m at station 4 throughout 2009-2011. Upwelling periods (12oC isotherm shoals above 30m) are identified by dark lines located underneath each panel

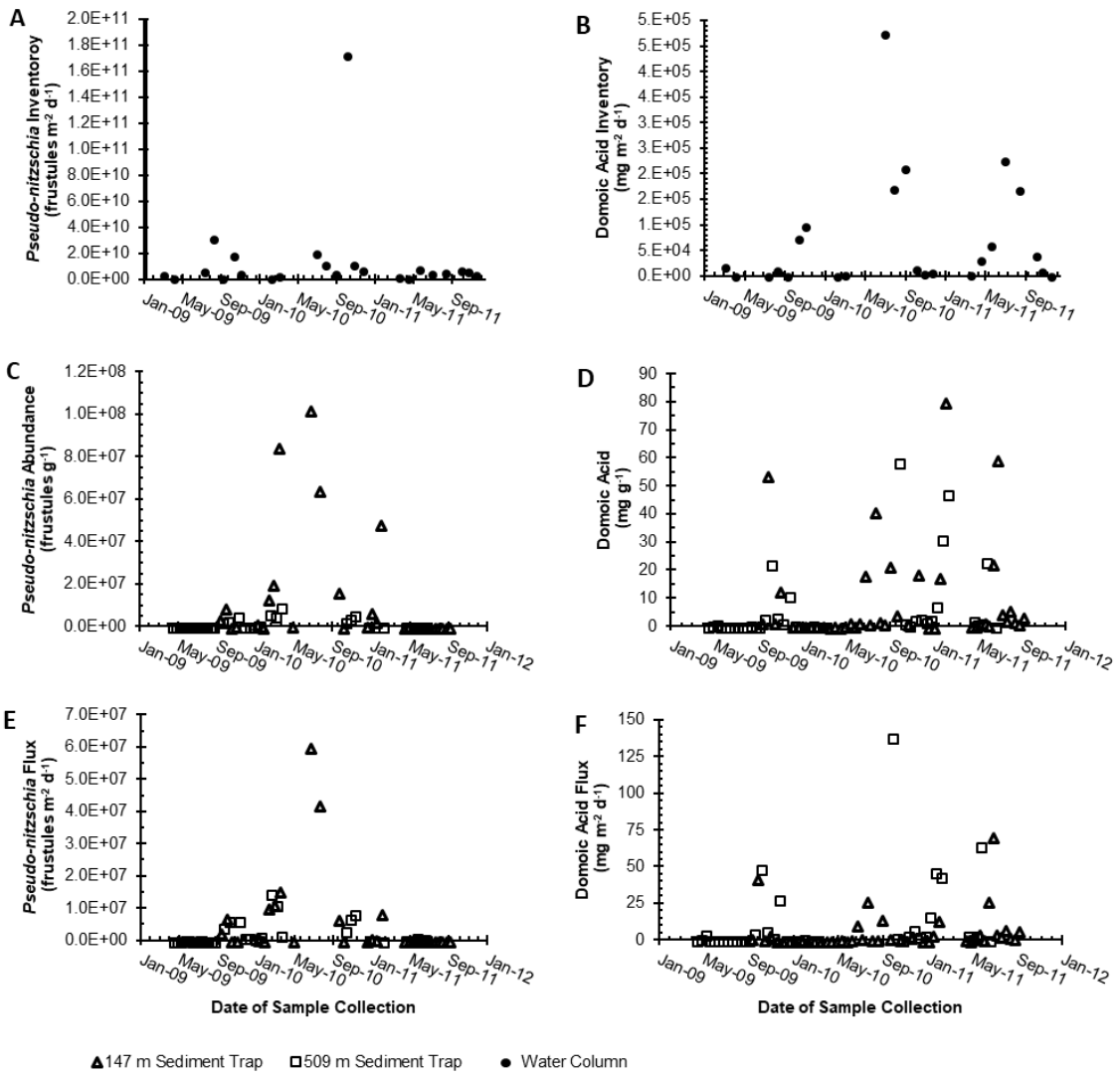

Figure 2.7 Plots of Pseudo-nitzschia abundance (A) and DA inventory (B) integrated over the upper 150m of water column (black circles), Pseudo-nitzschia abundance (C), tDA abundance (D), Pseudo-nitzschia flux (E), and tDA flux (F) into the 147m (triangles) and 509 m (squares) sediment traps from 2009-2011. Inventory over 150 m is calculated by multiplying DA or *Pseudo-nitzschia* by the distance from the midpoint from the overlying sampling point to the midpoint from the sampling point below the targeted depth and adding these products together from 0-150 m.

CHAPTER 3: SEASONAL VARIATIONS IN THORIUM-234 DERIVED MERCURY, CARBON AND NUTRIENT PARTICLE FLUXES AT STATION ALOHA[2]

[2] Blaire P. Umhau, Laura Motta, Hilary G. Close, Brian N. Popp, Cecelia C. S. Hannides, Claudia R. Benitez-Nelson, Joel D. Blum and Jeffrey C. Drazen. To be submitted to *Marine Chemistry*

Abstract

Particle dynamics are an essential component of global ocean biogeochemistry. Particles transport essential nutrients, carbon, and trace metals through the water column and facilitate the removal of pollutants, such as mercury (Hg), from surface waters. Station ALOHA is the site of the long-running Hawaiian Ocean Time-series located in the North Pacific Subtropical Gyre (NPSG) and is characterized by a well-defined summer export pulse that influences the composition and structure of the biological community within the mesopelagic zone. In three contrasting seasons we determined the downward fluxes of particles and associated carbon (PC), nitrogen (PN) and total mercury (PHg) over the upper 400 m at Station ALOHA using a combination of sediment traps and *in situ* pumps coupled with ^{238}U -^{234}Th disequilibria. February PC fluxes ranged from 920 µmol C m^{-2} day^{-1} at the surface to near zero at 400 m. September and May PC fluxes were significantly higher and increased with depth to a maximum flux of 4670 µmol C m^{-2} day^{-1} at 400 m in September which coincided with the seasonal summer export pulse associated with diazatrophs. Even though the highest absolute PC fluxes were observed during summer, our findings indicate that zooplankton exert more influence over both small and large PC (and PN) fluxes in February than in September or May, when heterotrophic bacteria play a proportionally larger role in particle remineralization and cycling. PHg fluxes were also seasonally variable and highest in May and September yet were influenced by different biogeochemical cycling processes than carbon in the subsurface. The ratio of Hg/C increased dramatically below the deep chlorophyll maximum at 150 -200 m, likely due to a shift in microbial degradation patterns that increased Hg surface adsorption and produced methylmercury that is more efficiently

bioaccumulated. PHg fluxes in May and September were higher than those previously measured in the equatorial Pacific at the depth of 150 m and continue to be high (> 250 pmol Hg m^{-2} d^{-1}) down to 400 m, thereby providing a significant source of Hg that may be incorporated into the mesopelagic food web.

Keywords: Particle flux, Uranium-238, Thorium-234, Mercury, Station ALOHA

3.1 Introduction

A critical component of trace element, carbon, and nutrient biogeochemical cycling is understanding the magnitude and composition of particles as they sink from surface waters to deep within the ocean interior (Buesseler et al., 2008). These particles include materials ranging from senescent phytoplankton and zooplankton molts to lithogenic and other inorganic materials that form larger aggregates, which may sink more efficiently than smaller particles (Buesseler et al., 2008; Lam et al., 2015). The formation, composition, and remineralization of sinking particles is mediated in part by complex food webs that span the water column and determine the efficiency of the biological pump (Buesseler et al., 2008; Buesseler and Boyd, 2009; Siegel et al., 2014). Scavenging of dissolved seawater constituents onto particles is an important mechanism for the introduction and subsequent bioaccumulation of trace elements in marine biota (Lam et al., 2015; Lamborg et al., 2016). While much work has focused on large (100-1000s µm) particles as the major mechanism of particle transport from surface waters into the mesopelagic (Michaels and Silver, 1988), numerous studies also now recognize the important contributions of small, slowly settling particles to vertical fluxes (1-10s µm; Puigcorbé et al., 2015; Richardson and Jackson, 2007). Indeed, small particles are now recognized as an important component in trace element and isotope scavenging and

cycling due to their high surface area (Lam et al., 2015) and are also a potential food source for higher trophic levels (Alonso-Gonzalez et al., 2010; Choy et al., 2015; Durkin et al., 2015; Lam et al., 2015).

Thorium-234 (^{234}Th) is one isotope that is effectively scavenged onto small and large marine particles and has therefore proven to be a valuable proxy for measuring sinking particle flux on timescales of days to weeks (Benitez-Nelson et al., 2001; Buesseler et al., 2009). Uranium-238 (^{238}U) is a long-lived radioisotope ($t_{½}$ =4.5 x 10^9 years) and a conservative component of seawater; its radiogenic daughter, ^{234}Th, is short-lived ($t_{½}$=24.1 days) and highly particle reactive. As such, the particulate distribution of ^{234}Th has been used to constrain carbon (Buesseler et al., 2009; Haskell et al., 2013; Owens et al., 2015), nutrient (Kadko et al., 1994; Maiti et al., 2008; Puigcorbé et al., 2015), and trace metal export in a range of environments (Lamborg et al., 2016; Weinstein and Moran, 2005).

Mercury (Hg) is a potent toxin, both in its elemental form and in the form of methylated compounds; dimethylmercury (DMHg) and monomethylmercury (MMHg) (Fitzgerald and Lamborg, 2003). MMHg is especially toxic and of concern because once it is introduced into the ecosystem, it bioaccumulates within fish which are commercially harvested for human consumption (Fitzgerald and Lamborg, 2003; Selin, 2009). Choy et al. (2009) found that Hg concentrations in pelagic fish increased with depth and that the mesopelagic was an important source of Hg to the marine food web. Recent work further indicates that Hg methylation occurs below the surface mixed layer (Blum et al., 2013). These observations suggest that both surface and subsurface processes are important in determining the magnitude of Hg incorporation into the mesopelagic marine food web

(See Cossa et al., 2012). Unfortunately, information regarding the flux and transformation of Hg in the water column remains very limited. In one of the few studies to examine particulate Hg export, Munson et al. (2015) found PHg fluxes to range from below detection (< 1.52 pmol m^{-2} day^{-1}) to as high as 123 pmol m^{-2} day^{-1} at 150 m in the central North Pacific.

Using a combination of free floating sediment traps and *in situ* pumps, we used ^{238}U:^{234}Th disequilibria to determine particulate carbon (PC), nitrogen (PN), and Hg (PHg) export throughout the upper 400 m at Station ALOHA (A Long-Term Oligotrophic Habitat Assessment) located in the North Pacific Subtropical Gyre (NPSG) (22°N, 158°W). Samples were collected over a seasonal cycle in February 2014, September 2014, and May 2015. Results were integrated with measurements of Hg stable isotope measurements (Motta et al. Submitted) and particle and food web trophic dynamics using speciation measurements and the ^{15}N of amino acids (Hannides et al., submitted, Close et al. in prep, Gloeckler et al. 2018).

3.2 Study Area

Station ALOHA is the site of the long-running Hawaii Ocean Time-series (HOT) Program and is believed to be representative of processes occurring throughout the North Pacific subtropical gyre (Karl and Lukas, 1996). While the thermocline and halocline remain relatively stable at this oligotrophic site throughout the year (varying from 40 to 100 m), a rapid particle export pulse is typically observed from mid-July to mid-August that delivers PC and PN to below the mixed layer (150 m) and into the deep ocean (4000 m) at rates up to three times higher than other times of the year (Karl et al. 2012, Böttjer et al. 2017). This consistent summer export pulse is associated with increased N_2 fixation

by symbiotic cyanobacteria-diatom assemblages (Böttjer et al., 2017; Karl et al., 2012). The exact mechanism underlying the increase in N_2 fixation remains ambiguous, but it has been connected to both increased day length (Karl et al. 2012) and mesoscale eddies (Guidi et al., 2012).

3.3 Methods

3.3.1 Sample Collection

Seasonal samples were collected at Station ALOHA on cruises ranging from 10 to 14 days in February 2014, September 2014, and May 2015, representing seasons previously identified as having low, high, and intermediate sinking particle fluxes, respectively (Karl et al., 2012). Total ^{234}Th samples were collected using the methods described in Buesseler et al. (2001) and Benitez-Nelson et al. (2001). Briefly, 2 L of seawater was collected at selected depths (N = 11-13) from 5 - 2500 m using Niskin bottles mounted on a carousel. Samples were spiked with ^{230}Th as a yield tracer and acidified to pH ~ 1 using concentrated nitric acid. After equilibration, ~ 6 hours later, $KMnO_4$ and $MnCl_2$ were added and the pH adjusted to ~ 9 with concentrated NH_4OH in order to co-precipitate Th via the formation of MnO_2. After eight hours, total ^{234}Th samples were filtered onto 25 mm QMA filters, air dried, and frozen. Initial sample counts were made ~2 weeks after collection on shore using a low level RISO beta counter. Samples were recounted after 6 months to obtain background counts. Thorium recoveries were measured using ICP-MS according to the methods described in Pike et al., (2005). Briefly, after background counts were obtained, precipitate was removed from filters with a solution of 8M HNO_3/10% H_2O_2 then spiked with ^{229}Th as a recovery tracer. This solution was sonicated for 30 min and left overnight. The solution was then

evaporated down to less than 1mL and rinsed with HNO_3 and evaporated down again. A 10% HNO_3/1% HF solution was then added to reach a final 2 ml volume. Samples were filtered through a 0.2 µm filter to avoid clogging the ICP-MS capillary. ^{238}U was calculated using equation 3.1 from Owens et al. (2011) and salinity measurements.

$$^{238}U \text{ (dpm } L^{-1}) \pm 0.047 = 0.0786 \times \text{Salinity} - 0.315 \quad \text{(Eq 3.1)}$$

Salinity, temperature, fluorescence and oxygen measurements were obtained from a Seabird SBE 9/11plus CTD deployed with two Sea-Bird SBE 3P temperature sensors, two Sea-Bird SBE 4C conductivity sensors and two Sea-Bird SBE 43 dissolved oxygen sensors and a Wetlabs ECO FLNTU Chlorophyll Fluorometer & Turbidity sensor.

A set of McLane WTS-LV pumps were deployed with two sequential filters sizes mounted on metal-free filter holders to capture small and large sinking particulates in the >53 µm and 1-53 µm size range using 142 mm Nitex and QMA filters, respectively, according to the methods described by Lam et al (2015). QMA filters used for Hg collection were pre-combusted and stored in acid pre-cleaned petri dishes in plastic bags. Filters used for PC and PN were pre-combusted and stored in combusted foil prior to use. Pumps were deployed at depths between 10 and 400 m (N = 10) and pumped between ~ 600-6000 L per deployment at a rate of 3-8 L min^{-1}. The QMA filters were subsampled under trace metal clean conditions in triplicate using a ~ 25 mm Delrin punch for particulate ^{234}Th analysis and the remaining filter was analyzed for total mercury and mercury isotopes ratios (see Motta et al., submitted). The majority of samples for 1-53 µm PC and PN were also collected from the same filter using the Delrin punch. All samples were immediately frozen at -80˚C. Large particle (> 53 µm) samples were

collected using acid cleaned (10% hydrochloric acid) Nitex filters, rinsed onto 25 mm QMA filters using filtered seawater, mounted onto RISO discs, and immediately frozen at -80˚C prior to analysis for ^{234}Th, PC, and PN. Additional large particle samples for Hg analyses were collected on separate deployments at rates of 15-20 L min^{-1} using acid cleaned (10% trace-metal grade HCl) Nitex screens (53 μm) and were frozen whole and stored in trace metal clean petri dishes. In addition to using the McLane pumps, particle interceptor style (PIT) sediment traps were deployed for ~ 3 days at 150 and 155 m and material filtered onto 142 mm QMAs that were subsampled and analyzed for particulate ^{234}Th, PC, and PN (Knauer et al., 1979).

3.3.2 Analyses

All total Hg concentrations of particles (PHg) were measured at the University of Michigan according to the methods described in Motta et al. (Submitted). Small particles underwent microwave assisted digestion, then samples were measured for total Hg by cold vapor atomic absorption spectroscopy (CV-AAS; Nippon Instruments) (eg., Biswas et al., 2008). Large particle samples from the same depth were combined and rinsed onto QMA filters that were then lyophilized. Total Hg was extracted from filters by combustion, trapping in an oxiding $KMNO_4$ solution and then analysis of the solution for Hg using CV-AAS. Particulate C and PN samples were analyzed at the University of Hawaii according to the methods described in Kennedy et al. (2005). Once ashore, samples were dried overnight at 60°C and then encapsulated in tin cups for analysis of PC and PN concentrations. Carbon and nitrogen content and isotopic composition of all filters were determined using an isotope ratio mass spectrometer (IRMS; Delta ^{Plus}XP) coupled to an elemental analyzer (Conflo IV/Costech ECS 4010). Several samples were

also analyzed for particulate organic carbon (POC) and were subjected to decarbonation using sulfurous acid prior to analysis (Kennedy et al., 2005). POC and PC concentrations were within 10-15% of one another indicating that particulate inorganic C concentrations were minimal during our study period.

3.4 Results

3.4.1 Study Area

Station ALOHA is an oligotrophic site with little seasonal variation in salinity, temperature or oxygen (Buesseler et al., 2008; Church et al., 2013). During this study, oxygen concentrations decreased gradually from the surface (~200 µmol kg^{-1}) down to ~175 m before declining more rapidly down to the oxygen minimum zone at 700 m (~33 µmol kg^{-1}) for all seasons. The mixed layer depth varied with season from 100 m in February to 45 m in May and September. Surface temperatures were slightly warmer in September (27.4^{o}C) than in February and May (24.5^{o}C). Fluorescence was lowest in February and highest in September, with fluorescence maxima observed at ~ 125 m for all seasons (0.4-0.9 mg m^{-3}) (Figure 3.3.1).

3.4.2 Total ^{234}Th

Total ^{234}Th activities ranged from 1.91 to 2.67 dpm L^{-1}, with depth profiles indicating higher sinking particle formation in the upper 50 m and between 100 - 150 m (^{238}U activity > ^{234}Th activity = ^{234}Th deficit, particle formation) and remineralization below 200 m (^{234}Th activity > ^{238}U activity = ^{234}Th excess, remineralization) in February and May. Deeper deficits in ^{234}Th activity in February and May were associated with the deep chlorophyll maximum as evidenced by a peak in fluorescence at ~ 125 m. No similar subsurface ^{234}Th deficit peak was observed in September, even though the peak in

fluorescence was significantly larger and broader than in May or February (t-test, $P < 0.05$) (Figure 3.3.1). The September ^{234}Th profile shows a small, but consistent ^{234}Th deficit (~0.2 dpm L^{-1}) throughout the upper 300 m.

3.4.3 Particle Concentrations

Small particle ^{234}Th activities (1- 53 µm) ranged from below detection (>0.4 dpm per sample) to 0.25 dpm L^{-1} (Table 1) and averaged 0.15 ± 0.04. There were no significant seasonal differences and no clear trends with depth. In contrast, small PC concentrations were highest at the surface with highest concentrations measured in September (1528 nmol L^{-1}) that were almost double those measured in May and February. PC concentrations generally decreased with increasing depth down to ~ 400 nmol L^{-1} by 150 m for all cruises (Table 1). Small PN concentrations followed similar trends (Table 1). Small PHg also had highest concentrations at the surface that declined with depth. Unlike PC and PN, however, seasonal differences in surface PHg concentrations were small (60 – 90 fmol L^{-1} at 25 m, Table 1), with highest concentrations measured in September, followed by February, and then May. PHg concentrations declined by only 30 - 50% with increasing depth, reaching relatively constant concentrations of 20 - 40 fmol L^{-1} by 150 m.

Large particle (> 53 µm) ^{234}Th activities ranged from below detection to 0.033 dpm L^{-1} and were an order of magnitude lower than those measured in the small particles. Large ^{234}Th activities also did not change with season or depth and averaged 0.015 ± 0.007 dpm L^{-1}(Table 1). In surface waters (25 m), large PC concentrations were again highest in September (212 nmol L^{-1}), followed by lower concentrations in May (130 nmol L^{-1}) and February (70 nmol L^{-1}). Differences between surface September PC and May

and February PC, however, were much more pronounced in the large versus small particles; September PC was 3 times higher than February PC in the > 53 µm, compared to 1.5 times higher in the 1 - 53 µm fraction. Large PC concentrations also declined rapidly with increasing depth, reaching an average concentration of ~ 20 nmol L^{-1} by 400 m. PN concentrations followed similar trends. There is not enough large particle PHg data to discern trends, however PHg concentrations were an order of magnitude lower than those measured in the smaller particle fraction at the same depths and averaged 2.2 ± 0.1 fmol L^{-1}.

3.4.4 Elemental Ratios

Ratios of small particle PC to ^{234}Th (PC/Th) were significantly higher in September compared to other seasons (t test, $P < 0.05$) and remained relatively high (10 µmol dpm^{-1}) throughout the mixed layer (~ 50 m) before decreasing sharply to a constant ratio of ~2 µmol dpm^{-1} at ~ 125 m. Small particle February and May PC/Th ratios were the same, within error, decreasing rapidly from the surface (7 µmol dpm^{-1}) to a constant ratio of ~ 1.5 µmol dpm^{-1} at 150 m (Figure 3.3.2). PN/Th ratios followed a similar pattern (Figure 3.3.2). Variations in PC and PN to Th across seasons and depth were almost entirely driven by PC and PN concentrations rather than ^{234}Th activity.

Large particle PC/Th ratios for May and February were similar to one another, with highest ratios (12 µmol dpm^{-1}) in the upper 50 m that decreased to 2.4 µmol dpm^{-1} at 100 m (Figure 3.3.2). September PC/Th ratios were again much higher, 77 µmol dpm^{-1} in the upper 50 m, relative to the other months, and rapidly declined with depth to match February and May ratios at 125 m. Large particle PN/Th ratios followed similar trends. Compared to the PC/Th ratios measured in the sediment trap, pump PC/Th ratios (1 - 53

µm and > 53 µm) were 4 and 2 times lower in May and February, respectively. Trap and pump ratios are similar in September.

Small particle PHg/Th ratios also varied seasonally over the upper 200 m, but not to the same extent or with similar timing to PC and PN/Th ratios. These differences were again driven almost entirely by changes in PHg concentrations. Highest surface ratios occurred in September (750 fmol dpm^{-1}), decreased in February (610 fmol dpm^{-1}), and were lowest in May (430 fmol dpm^{-1}). Ratios of PHg/Th on small particles declined with increasing depth in the water column, reaching constant values of ~ 200 fmol dpm^{-1} at ~ 150 m, with the exception of a subsurface PHg/Th peak at 175 m in May (Figure 3.3.2). Given the limited PHg data on large particles, it is impossible to discern significant seasonal and depth trends; the May Hg/Th ratio was higher than the September Hg/Th ratio (250 versus 30 fmol dpm^{-1}) at 150 m (Figure 3.3.2). THg was not measured in the sediment traps.

In order to determine potential differences in bioaccumulation versus surface adsorption, we further examined Hg/C ratios. Ratios of Hg/C are relatively constant over the upper 150 m, with significantly higher ratios measured in February (t-test, $p < 0.01$) relative to May and September. In all seasons, there was an abrupt increase in the Hg/PC ratio at ~ 175-200 m that ranged from ~55 fmol μmol^{-1} in September to ~90 fmol mol^{-1} in May. Although both Hg and PC generally decline with increasing depth, this increase in the Hg/PC ratio is almost entirely driven by a reduction in PC concentrations.

3.4.5 Elemental particle fluxes derived using ^{234}Th:^{238}U disequilibrium

Particle fluxes derived using ^{234}Th:^{238}U disequilibrium were determined by first calculating the ^{234}Th flux (dpm m^{-2} d^{-1}) using Equation (2), which assumes steady state and minimal physical processes:

$$(A_{238U}-A_{234Th})*\lambda_{234Th}*z = {}^{234}\text{Th flux} \quad \text{(Eq. 2)}$$

Where, A_{238U} is the ^{238}U activity (dpm L^{-1}) determined using the salinity relationship of Owens et al. (2011), A_{234Th} is the measured ^{234}Th activity (dpm L^{-1}), λ_{234Th} is the radioactive decay constant for ^{234}Th (0.02876 d^{-1}) and z is the depth interval of interest (in m). Using trapezoidal integration, the ^{234}Th flux was calculated at specific depths in the water column. ^{234}Th fluxes were calculated across specific depth ranges based on sampling depths, then added to the fluxes calculated from overlying depths to find the total flux across a specific depth horizon(Buesseler et al., 2009). Physical processes are assumed to be negligible as there was no evidence of mesoscale features during sample collection (i.e., upwelling). While non-steady state temporal fluxes likely occur in September due to the summer export pulse, the lack of time series sampling precludes the inclusion of a non-steady state term. In February and May 1999, Benitez-Nelson et al. (2001) found that there was little difference between fluxes calculated using steady state versus non-steady state assumptions at Station ALOHA.

Water column derived ^{234}Th fluxes ranged from -10 (February) to 1546 (September) dpm m^{-2} day^{-1}, with both of these extremes measured at 400 m. Surface fluxes ranged from 125 (February) to 30 (September) dpm m^{-2} day^{-1} (Table 2). In May and September, fluxes generally increased with increasing depth, while in February ^{234}Th

fluxes peaked at 175 m before decreasing to ~ 0 at 400 m. ^{234}Th fluxes determined from ^{234}Th:^{238}U disequilibria at 150 m were the same, within error, as those determined using the sediment traps deployed at 150 m and did not vary significantly with season (Table 3).

Small and large particle element to ^{234}Th ratios at a given depth horizon (e.g., PHg/Th) were multiplied by the ^{234}Th flux at that depth horizon to determine ^{234}Th derived fluxes of PC, PN, and PHg throughout the water column (Buesseler et al., 2006). Small and large particle element to ^{234}Th ratios were each used to determine fluxes as well as element to ^{234}Th ratios measured in the sediment traps deployed at 150 m. These various flux calculations therefore provide a range in the absolute flux of material to depth, with comparisons between size classes and sample collection providing information regarding the processes influencing particle formation across space and time.

In February PC fluxes using small and large particle ratios show a similar pattern in the upper 50 m before rapidly attenuating with depth until ~ 100 m. A subsurface peak in PC flux occurs at 175 m, just below the base of the euphotic zone. In May, small and large ^{234}Th-derived PC fluxes differ in their trends, with small PC fluxes remaining relatively constant at 1270 ± 506 μmol m^{-2} d^{-1} over the upper 400 m. Large PC fluxes in May were significantly more variable, with subsurface peaks at 50, 150, and 400 m that were 2-3 times greater than PC fluxes measured directly above or below (Figure 3.3.3). In September, small and large particle PC fluxes are similar and high throughout the water column, from the surface down to 400 m (1771 ± 967 and 2194 ± 992 μmol m^{-2} d^{-1} for small and large PC fluxes, respectively). Unlike February and May, there were no

significant subsurface peaks associated with the base of the euphotic zone in September. PN fluxes followed the same seasonal and depth trends of the PC fluxes (Figure 3.3.4).

Particulate Hg fluxes ranged from ~ 0 to 373 pmol m^{-2} day^{-1} depending on the use of small versus large particle Hg/Th ratios. Generally, PHg fluxes followed similar depth trends to PC and PN fluxes. They attenuate with increasing depth in February, and gradually increase with depth in May and September when using the small particle Hg/^{234}Th ratio. Both February and May have subsurface peaks in PHg fluxes occurring below the deep chlorophyll maximum at 150 – 200 m. Large particle Hg fluxes are difficult to compare given the limited data. At 150 m the large particle Hg flux in May is more than two times higher than the small particle flux, whereas in September, small particle Hg flux at 150 m is more than 5 times higher than large particle flux. In February at 25 m, Hg fluxes are the same for both small and large particles. It is important to note that in February at 400 m, the large particle flux was estimated using particulate Th at 250 m (no data available at 400 m) and Hg concentrations measured at 400 m. This is reasonable considering that large particulate ^{234}Th concentrations remain relatively constant below 150 m (see Table 1 and Figure 3.3.5).

Sediment trap fluxes were calculated both by direct measurement of material per square meter per time deployed, and by multiplying the water column derived ^{234}Th flux by the element to ^{234}Th ratio measured in the trap material (Table 3). Seasonal differences are almost entirely driven by the C/Th ratio used (Figure 3.3.2). Mercury concentrations were not determined in sediment trap material due to contamination concerns. Directly measured sediment trap PC and PN fluxes in February, May and September are consistently higher than those determined using both small or large C

(N)/Th ratios and water column ^{234}Th:^{238}U disequilibria (Table 3, Figure 3.3.3,4). There is no difference between the two sediment trap-calculated PC fluxes in February, although they were twice as high as those determined using the *in situ* pump C/Th ratios and water column derived ^{234}Th fluxes. In September, the PC flux derived from trap C/Th ratios was about half that directly measured using sediment traps, but similar to those determined using *in situ* pump C/Th ratios and water column derived ^{234}Th fluxes.

3.5 Discussion

Sinking particles are a major pathway for transporting material from the surface ocean to the mesopelagic and play a critical role in processes ranging from the oceans' capacity to act as a sink for atmospheric carbon dioxide to serving as a food source and a mechanism for the transfer of contaminants through the food web (Buesseler et al., 2006; Siegel et al., 2014). Because organic matter is a large component of most particles in the open ocean, aggregation and remineralization are largely controlled by biotic processes, and sinking particles are of fundamental importance to the benthic and mesopelagic food web (Hannides et al., 2013; Lam et al., 2015; Puigcorbé et al., 2015). As a result, C and essential nutrients such as N have been the focus of many particle flux studies, with less attention focusing on trace elements and contaminants, such as mercury (Buesseler et al., 2009, 2006; Lam et al., 2015; Owens et al., 2015). Furthermore, C and N cycling through the biological pump are fundamentally different from Hg because MMHg, bioaccumulates in organism tissues (Lamborg et al., 2014).

3.5.1 Thorium activities

^{234}Th:^{238}U disequilibria measurements provide a mechanism for understanding where in the water column particle formation and remineralization occur on a relatively

high resolution spatial scale (Buesseler et al., 2009). When ^{234}Th is measured in conjunction with particulate element (i.e., C) to ^{234}Th ratios, a profile of elemental (PC) fluxes versus depth can be determined. Furthermore, because ^{234}Th is radioactive, activities reflect processes integrated over the mean life of the radionuclide prior to measurement, in this case, ~ 35 days.

Although previous studies in the region are limited, total ^{234}Th:^{238}U disequilibria profiles, ^{234}Th fluxes, and small and large particulate ^{234}Th activities are similar to those previously measured at Station ALOHA. For example, subsurface deficits in ^{234}Th activities relative to ^{238}U (i.e., particle formation) at the depth of the deep chlorophyll maximum are a common feature over the summer months, as are peaks in remineralization at depths immediately below the deep chlorophyll maximum (Benitez-Nelson et al., 2001). However, the extent of the remineralization peaks measured by Benitez-Nelson et al. (2001) were smaller and there was no surface to 350 m depth disequilibria measured in their July – August 1999 profiles. Buesseler et al. (2009), however, did observe significant ^{234}Th deficits throughout the upper 350 m in their ^{234}Th data collected during June and July of 2004, consistent with our September profile.

Station ALOHA is characterized by low ^{234}Th deficits, which, when combined with error propagation and repeated measurement profiles, leads to relatively high uncertainties on ^{234}Th derived water column fluxes using the 1-D steady state model (Buesseler et al., 2009). As we were only able to measure a single profile during each cruise, our flux errors should be considered minimum estimates as they are based solely on measurement uncertainties. Regardless, our cumulative range of direct sediment trap and water column ^{234}Th fluxes at 150 m (414 to 692 dpm m^{-2} d^{-1}) are similar to the 377 ±

395 dpm m^{-2} d^{-1} determined by Buesseler et al. (2009) in June and July (2004) and the 765 ± 628 dpm m^{-2} d^{-1} determined over a seasonal cycle (1999-2000) by Benitez-Nelson et al. (2001). Note that Benitez-Nelson et al. (2001) measured steady state ^{234}Th fluxes as high as 2311 dpm m^{-2} d^{-1} in October, which may have reflected a late summer export pulse during that year.

3.5.2 Particulate C, N, and Hg Concentrations

Although Station ALOHA has been characterized as a static environment in terms of seasonal changes in nutrients, temperature, salinity, etc. (Buesseler et al., 2008; Church et al., 2013), primary production varies by a factor of two over the course of the year, with highest rates observed in the summer due to late summer blooms of symbiotic cyanobacteria-diatom assemblages that induce a rapid pulse of material to depth (Böttjer et al., 2017; Church et al., 2013; Karl et al., 2012). High concentrations of PC and PN across both size classes in September and in larger particles in May relative to February reflect the summer increase in primary productivity observed by Church et al. (2013). May appears to coincide with the beginning of the summer increase in productivity, while September reflects the middle to end of the bloom. High small particle PC concentrations in September were likely caused by the accumulation of particles over the course of the summer's high biological production that either resulted from disaggregation of large particles or was due to production of small particles over the course of the bloom (Karl et al., 2012; Lam and Marchal, 2015). Both small and large PC concentrations rapidly attenuate to similar concentrations with increasing depth irrespective of season. This suggests that PC, regardless of bloom stage or "freshness",

was rapidly remineralized with increasing depth, indicating an active microbial foodweb. PN shows the same trends. (See section 3.4.3)

Particulate Hg does not show the same seasonal differences as those observed for PC or PN. Unlike PC and PN, particulate Hg concentrations are a function of atmospheric deposition and scavenging in addition to biological activity(Lamborg et al., 2014). While seasonal changes in atmospheric Hg deposition to this region may be possible (Chen et al., 2014), there are no measurements that suggest this is the case, and seasonal variability in PHg concentrations measured in this study was relatively low. In surface waters at stations south of ALOHA, Munson et al. (2015) found that both PHg and total Hg concentrations were lower at the equator (20 and 300 fmol L^{-1}) and higher at 17°N (30 and 500 fmol L^{-1}). They hypothesized that the higher concentrations at 17°N resulted from greater atmospheric deposition caused by increased rainfall in the intertropical convergence zone (ITCZ). Higher PHg and total Hg concentrations (Motta et al., submitted) at Station ALOHA compared to Munson et al at 17°N are spatial changes in Hg concentrations in ocean basins (Bowman et al., 2016; Munson et al., 2015).

3.5.3 Element/Th ratios

Element to thorium ratios are a critical component of estimating ^{234}Th based water column fluxes of an element or compound of interest (Buesseler et al., 2006). Ratios can change with depth due to a variety of physical, biological and chemical processes, ranging from changes in particle surface area to bacterial reworking, and thus will vary based on particle size and water column dynamics (Buesseler et al., 2006; Lam et al., 2015). PC/Th ratio profiles in both small and large size classes in May and February were similar throughout the water column (Figure 3.2), suggesting similar processes are

influencing both particle sizes, such as aggregation of small particles into larger ones, or disaggregation of large particles. In September PC/Th ratios in both the small and large fractions were much higher over the upper 100 m than those observed during the rest of the year. Large PC/Th ratios were also significantly higher than small PC/Th ratios. This difference in September PC/Th ratios between size fractions is likely due in part to the higher volume (C content) to surface area (surface-reactive Th) ratio inherent in larger particles, assuming a roughly spherical shape (Buesseler et al., 2006). Large colonies of *Trichodesmium* spp comprise a much larger component of the phytoplankton assemblage in the late summer and early fall at Station ALOHA compared to the rest of the year when the ecosystem is dominated by picoplankton (Pasulka et al., 2013). There was visual evidence of *Trichodesmium* spp. cells on the Nitex filters collected in September, but not in February or May (H. Close, pers. comm.). The $\delta^{15}N$ values of source amino acids in particles collected on these cruises also indicate the presence of diazotrophs in the summer large particle fraction (Close et al., submitted). Combined, variations in PC/Th ratios seasonally and across size fractions over the upper 100 m were largely driven by changes in phytoplankton assemblage. Below 100 m, PC/Th ratios converge, averaging 2.0±0.7 μmol dpm^{-1} for small PC/Th ratios and 3.1 ±0.6 μmol dpm^{-1} for large PC/Th ratios at 150 m. These ratios are similar to those found at 150 m by Benitez-Nelson et al. (2001) and Buesseler et al. (2009) at Station ALOHA, which ranged from 1.9 to 5.4 μmol dpm^{-1} and 3.6 to 7.5 μmol dpm^{-1} for small and large particles, respectively. Sediment trap PC/Th ratios previously reported at Station ALOHA range from 3.9-14.9 μmol dpm^{-1} at 150m (Benitez-Nelson et al., 2001; Buesseler et al., 2009), which is higher than those measured in this study (1.3-6.4 μmol dpm^{-1}) (Figure 3.2).

Similar to PC/Th ratios, PHg/Th ratios decrease rapidly from the surface to 150 m, but there are some distinct seasonal differences. These differences suggest that separate processes influence PHg concentraion and remineralization. While PHg/Th ratio measurements in large particles are limited, they are the same or lower than those measured at the same depths in small particles. Thus, PHg/Th ratios do not appear to be driven by differences in volume to surface area ratios. Lamborg et al. (2016) found that the Hg sorption capacity of particles in the North Atlantic was not saturated. This appears to be the case here as well; changes in Hg/Th ratios reflect Hg concentrations rather than Th activity (Figure 3.2).

Closer examination of PHg/PC ratios in small particles shows a sharp increase, by a factor of 2 – 3, between 100-150 m. This increase is smallest in September and largest in May, indicating either abrupt remineralization of PC relative to PHg and/or preferential incorporation of Hg into particles. The increase in PHg/PC coincides with a transition zone in particle degradation from food web dominated to microbial hydrolysis dominated based on the ^{15}N signature of source amino acids by Close et al. (submitted). Mende et al. (2017) also found this depth range to be a transition zone in microbial community makeup. A change in microbial communities and increased bacterial degradation at depth is consistent with increased Hg methylation (Lamborg et al., 2016), and increased MMHg concentrations below 150 m (Munson et al., 2015). Increased MMHg at depth provides another mechanism for subsurface uptake and bioaccumulation of Hg into particles. Motta et al. (submitted) found that there was evidence of increased Hg adsorption onto particles at 150m based on Hg isotope data, which could also be a factor in the increase in PHg/PC on particles near 150m.

3.5.4 PC and PN Fluxes

Seasonal changes in primary productivity and food web assemblage at Station ALOHA were reflected in our sinking particle data with PC and PN fluxes generally increasing from February to September, coincident with the late summer export pulse (Karl et al., 2012). Our PC fluxes were typically higher than those measured by Benitez-Nelson et al. (2001) at 150 m; their fluxes averaged 1.52 ± 0.20 mmol C m^{-2} day^{-1} and 0.85 ± 0.08 mmol C m^{-2} day^{-1} for ^{234}Th derived and sediment trap derived PC fluxes, respectively. They were within the range measured by Buesseler et al. (2009), however, which spanned from below detection (excess Th results in Th flux set at 0) to 7 mmol C m^{-2} day^{-1}. In this study, sediment trap fluxes were consistently higher than *in situ* pump derived fluxes at 150 m, regardless of the flux calculation method (direct or C/Th ratio), with the exception of September, which supports the possibility that timing is an important consideration when comparing sediment traps deployed for several days to ^{234}Th derived fluxes which integrate over longer time periods. It is important to note that Böttjer et al. (2017) suggested that sediment traps at Station ALOHA under-collect certain particle classes, and biases have been observed in under- or over-collection of particles during high and low flux events (Benitez-Nelson et al., 2001; Buesseler et al., 2007).

While the absolute magnitude of PC and PN fluxes across 150 m were consistent with seasonal variations in upper ocean phytoplankton assemblages (i.e., highest fluxes were coincident with an increase in *Trichodesmium* spp.), small and large PC and PN flux profiles throughout the upper 400 m were also seasonally influenced by a combination of zooplankton grazing and microbial reworking. Hannides et al. (submitted) found that

zooplankton biomass at Station ALOHA varied seasonally, being 1.7-2 times higher in September than in February throughout the euphotic zone (0 - 150 m). Although larger biomass differences were observed in the upper 50 m versus deeper (100 - 150 m), there were no significant differences in speciation or size class. Using the $\delta^{15}N$ values of source and trophic amino acids, Hannides et al. (submitted) further found little to no indication of seasonal differences in the feeding strategies or food sources for zooplankton above 300 m, but they did find significant differences below 300 m and into the deeper mesopelagic. In February, deep zooplankton altered their feeding strategy, switching from in situ large particles that were more readily available in September (highest PC fluxes) to either in situ small particles or nighttime vertical migration to feed on epipelagic particles. We hypothesize that this preferential zooplankton grazing on large particles between 150-250 m in February resulted in very similar small and large derived PC flux profiles due to biologically mediated aggregation and disaggregation processes. Efficient grazing further resulted in reduced PC fluxes to depth.

In May, large PC-derived fluxes were higher at 50 and 150 m relative to small PC derived fluxes, likely due to the production of large particles associated with surface biological production and the deep chlorophyll maximum. Below 200 m, the convergence in small and large PC fluxes indicates rapid disaggregation and remineralization.

September small and large particle fluxes were similar and remained high throughout the water column below 250 m. Close et al. (submitted) found that small and large particles have distinctly different degradation signatures. Small particles appeared to be undergoing increased microbial degradation, while large particles more closely resembled zooplankton fecal pellets. We hypothesize that while zooplankton grazing also

increased in September, it could not maintain the pace of the rapid production of phytodetritus associated with the summer export pulse that typically occurs during this period (Karl et al, 2012). As such, this material escaped zooplankton consumption and repackaging and was instead reworked by bacteria deeper in the water column, thus minimizing differences in small and large PC derived fluxes and explaining the more microbially dominated amino acid ^{15}N signal observed in upper mesopelagic particles (Close et al., submitted).

In oligotrophic environments such as Station ALOHA, where small phytoplankton and picoplankton dominate, small particles are hypothesized to be a major component of particle flux and PC export (Puigcorbé et al., 2015). Our findings are consistent with this hypothesis and showed that small particles, either via aggregation/disaggregation pathways or by direct sinking play an important role in particle export to depth. Choy et al (2015) and Gloeckler et al. (2018) found that in the NPSG, higher trophic levels, i.e., micronekton, rely heavily on small particles for food. Although Hannides et al. (submitted) indicated that large particles were an important food source for zooplankton, our data demonstrated these larger particles were scarce when the summer export pulse was over. Indeed, isotopic signatures of mesopelagic fish are similar to those of small surface particles, indicating that these fish rely on small particles from the surface; any isotopic signature showing evidence of large particle feeding in mesopelagic fish for the short time period of the export pulse would be overwhelmed by signals from the small particles the fish consume the rest of the year (Choy et al., 2015; Hannides et al., 2013).

3.5.5 PHg Fluxes

Quantifying PHg sinking fluxes is a crucial part of understanding Hg cycling and the depths at which Hg may be introduced into the food web (Munson et al., 2015). This study provides some of the first measurements of sinking PHg fluxes in the NPSG using *in-situ* pumps and how those fluxes change with water depth and season. Previous work made use of pumps only for particle concentrations and used sediment traps only for flux measurements (Lamborg et al., 2016; Munson et al., 2015; Strode et al., 2010). In this study, PHg fluxes were influenced by a combination of particle scavenging and biological processes that were distinct from those that influence PC fluxes as evidenced by PHg/Th and PHg/PC ratios. Munson et al. (2015) also found that PHg was preferentially transported to depth compared to PC. Using Hg isotope data, Motta et al. (submitted) found no indication of seasonal differences in Hg adsorption, photodegradation, methylation, and demethylation in the euphotic zone. They further found no differences in isotopic signatures between small and large particles at 150 m, providing an initial indication that both small and large particles may undergo the same methylation, demethylation, and adsorption processes. These results are consistent with the similarities in PHg/Th ratios measured in small and large particles and also with the idea that PHg fluxes at depth are mediated by particle scavenging in the upper water column (e.g., Lamborg et al., 2016; Motta et al., submitted; Munson et al., 2015). Higher PHg fluxes throughout the upper 100 m in September, followed by May and February were due to the more efficient sorption of Hg that occurs with the increased particle concentrations resulting from the summer plankton bloom. The 150 m PHg fluxes measured at Station ALOHA were generally much higher (18 - 174 pmol m^{-2} day^{-1}, Table

2) than the sediment trap fluxes reported by Munson et al. (2015) (30 ± 34 pmol m^{-2} day^{-1}) at 17°N, but similar to fluxes reported at the equator (123 ± 23 pmol m^{-2} day^{-1}).

In May and September, PHg fluxes continue to increase to 400 m, reaching fluxes that are more than double that measured at 150 m. These processes are likely facilitated by an increase in PHg fluxes via MMHg bioaccumulation during feeding (Heimbürger et al., 2010; Sun et al., 2014) and are in agreement with the findings of Close et al. (submitted), who argued that microbial reworking of small particles was more influential in September than zooplankton grazing on the particle pool. High PHg fluxes below 150 m in May and September are further consistent with the "regenerative scavenging" model of Hg particle-dissolution dynamics (adsorption and remineralization rather than desorption) (Lamborg et al., 2016; Siegel et al., 2014) and help to explain the high Hg concentrations measured in pelagic fish that forage in this depth range (Choy et al., 2009). These results further confirm that Hg methylation occurs below the surface mixed layer (Blum et al., 2013; Motta et al, submitted) and is an important source of Hg to the marine food web that must be considered for models exploring marine Hg biogeochemistry.

3.6 Conclusions

^{238}U-^{234}Th was used to measure PC, PN, and for the first time, PHg fluxes throughout the water column during winter, late spring/early summer and late summer at Station ALOHA in the NPSG. Seasonal changes in phytoplankton abundance resulted in the highest particle fluxes in September, greater influence of zooplankton grazing in February (lower PC fluxes), and greater influence of bacterial reworking in September and May (higher PC fluxes). Particulate N followed the same trends as PC across all size

classes, seasons and with depth. These results support hypotheses that small particles can be an important food source to mesopelagic zooplankton and fish during most of the year. While PHg fluxes followed a similar seasonal trend due to increased summer particle production followed by scavenging, higher PHg fluxes at depth were mediated by microbial processes that increased PHg fluxes by more than a factor of two. PHg fluxes at Station ALOHA are significant, with subsurface fluxes explaining the high Hg concentrations measured in pelagic fish and confirming that subsurface Hg cycling is a critical for understanding Hg bioaccumulation in marine systems.

Acknowledgements

This study was funded by National Science Foundation grant OCE 1433313, and BU was supported by a University of South Carolina Presidential Fellowship. We wish to thank the crew of the R/V Kilo Moana for enabling sample collection. We also wish to thank Justin Miyano, Natalie Wallsgrove, Kelly McCabe and Daniel Wade for their assistance with pump deployments.

3.7 References

Alonso-Gonzalez, I.J., Aristegui, J., Lee, C., Sanchez-Vidal, A., Calafat, A., Fabres, J., Sangra, P., Masque, P., Hernandez-Guerra, A., Benitez-Barrios, V., 2010. Role of slowly settling particles in the ocean carbon cycle. Geophys. Res. Lett. doi:10.1029/2010GL043827

Benitez-Nelson, C., Buesseler, K.O., Karl, D.M., Andrews, J., 2001. A time-series study of particulate matter export in the North Pacific Subtropical Gyre based on 234 Th : 238 U disequilibrium. Deep Sea Res. I 48, 2595–2611.

Benitez-Nelson, C.R., Buesseler, K.O., van der Loeff, M.R., Andrews, J., Ball, L., Crossin, G., Charette, M.A., 2001. Testing a new small-volume technique for determining 234 Th in seawater. J. Radioanal. Nucl. Chem. 248, 795–799.

Biswas, A., Blum, J.D., Bergquist, B.A., Keeler, G.J., Xie, Z., 2008. Natural mercury isotope variation in coal deposits and organic soils. Environ. Sci. Technol. 42, 8303–8309. doi:10.1021/es801444b

Blum, J.D., Popp, B.N., Drazen, J.C., Anela Choy, C., Johnson, M.W., 2013. Methylmercury production below the mixed layer in the North Pacific Ocean. Nat. Geosci. 6, 879–884. doi:10.1038/ngeo1918

Böttjer, D., Dore, J.E., Karl, D.M., Letelier, R.M., Mahaffey, C., Wilson, S.T., Zehr, J., Church, M.J., 2017. Temporal variability of nitrogen fixation and particulate nitrogen export at Station ALOHA. Limnol. Oceanogr. 62, 200–216. doi:10.1002/lno.10386

Bowman, K.L., Hammerschmidt, C.R., Lamborg, C.H., Swarr, G.J., Agather, A.M., 2016. Distribution of mercury species across a zonal section of the eastern tropical South Paci fi c Ocean (U . S . GEOTRACES GP16). Mar. Chem. 186, 156–166. doi:10.1016/j.marchem.2016.09.005

Buesseler, K.O., Antia, A.N., Chen, M., Fowler, S.W., Gardner, W.D., Gustafsson, O., Harada, K., Michaels, A.F., van der Loeff, M.R., Sarin, M., Steinberg, D.K., Trull, T., 2007. An assessment of the use of sediment traps for estimating upper ocean particle fluxes. J. Mar. Res. 65, 345–416. doi:10.1357/002224007781567621

Buesseler, K.O., Benitez-nelson, C.R., Moran, S.B., Burd, A., Charette, M., Cochran, J.K., Coppola, L., Fisher, N.S., Fowler, S.W., Gardner, W.D., Guo, L.D., Gustafsson, O., Lamborg, C., Masque, P., Miquel, J.C., Passow, U., Santschi, P.H., Savoye, N., Stewart, G., Trull, T., 2006. An assessment of particulate organic carbon to thorium-234 ratios in the ocean and their impact on the application of 234 Th as a POC flux proxy. Mar. Chem. 100, 213–233. doi:10.1016/j.marchem.2005.10.013

Buesseler, K.O., Boyd, P.W., 2009. Shedding light on processes that control particle export and flux attenuation in the twilight zone of the open. Limnol. Oceanogr. 54, 1210–1232.

Buesseler, K.O., Pike, S., Maiti, K., Lamborg, C.H., Siegel, D.A., Trull, T.W., 2009. Thorium-234 as a tracer of spatial , temporal and vertical variability in particle flux in the North Pacific. Deep. Res. Part I 56, 1143–1167. doi:10.1016/j.dsr.2009.04.001

Buesseler, K.O., Trull, T.W., Steinberg, D.K., Silver, M.W., Siegel, D.A., Saitoh, S., Lamborg, C.H., Lam, P.J., Karl, D.M., Jiao, N.Z., Honda, M.C., Elskens, M.,

Dehairs, F., Brown, S.L., Boyd, P.W., Bishop, J.K.B., Bidigare, R.R., 2008. VERTIGO (VERtical Transport In the Global Ocean): A study of particle sources and flux attenuation in the North Pacific. Deep. Res. II 55, 1522–1539. doi:10.1016/j.dsr2.2008.04.024

Chen, L., Wang, H.H., Liu, J.F., Tong, Y.D., Ou, L.B., Zhang, W., Hu, D., Chen, C., Wang, X.J., 2014. Intercontinental transport and deposition patterns of atmospheric mercury from anthropogenic emissions. Atmos. Chem. Phys. 10163–10176. doi:10.5194/acp-14-10163-2014

Choy, C.A., Popp, B.N., Hannides, C.C.S., Drazen, J.C., 2015. Trophic structure and food resources of epipelagic and mesopelagic fishes in the north pacific subtropical Gyre ecosystem inferred from nitrogen isotopic compositions. Limnol. Oceanogr. doi:10.1002/lno.10085

Choy, C.A., Popp, B.N., Kaneko, J.J., Drazen, J.C., 2009. The influence of depth on mercury levels in pelagic fishes and their prey. Proc. Natl. Acad. Sci. U. S. A. 106, 13865–13869. doi:10.1073/pnas.0900711106

Church, M.J., Lomas, M.W., Muller-karger, F., 2013. Deep-Sea Research II Sea change : Charting the course for biogeochemical ocean time-series research in a new millennium. Deep. Res. Part II 93, 2–15. doi:10.1016/j.dsr2.2013.01.035

Cossa, D., Harmelin-Vivien, M., Mellon-Duval, C., Loizeau, V., Averty, B., Crochet, S., Chou, L., Cadiou, J.-F., 2012. Influences of bioavailability, trophic position, and growth on methylmercury in hakes (Merluccius merluccius) from Northwestern Mediterranean and Northeastern Atlantic. Environ. Sci. Technol. 46, 4885–93.

doi:10.1021/es204269w

Durkin, C.A., Estapa, M.L., Buesseler, K.O., 2015. Observations of carbon export by small sinking particles in the upper mesopelagic. Mar. Chem. doi:10.1016/j.marchem.2015.02.011

Fitzgerald, W.F., Lamborg, C.H., 2003. Geochemistry of Mercury in the Environment. Treatise on Geochemistry 9.

Guidi, L., Calil, P.H.R., Duhamel, S., Björkman, K.M., Doney, S.C., Jackson, G.A., Li, B., Church, M.J., Tozzi, S., Kolber, Z.S., Richards, K.J., Fong, A.A., Letelier, R.M., Gorsky, G., Stemmann, L., Karl, D.M., 2012. Does eddy-eddy interaction control surface phytoplankton distribution and carbon export in the North Pacific Subtropical Gyre? J. Geophys. Res. Biogeosciences. doi:10.1029/2012JG001984

Hannides, C.C.S., Popp, B.N., Anela Choy, C., Drazen, J.C., 2013. Midwater zooplankton and suspended particle dynamics in the North Pacific Subtropical Gyre: A stable isotope perspective. Limnol. Oceanogr. 58, 1931–1936. doi:10.4319/lo.2013.58.6.1931

Haskell, W.Z., Berelson, W.M., Hammond, D.E., Capone, D.G., 2013. Particle sinking dynamics and POC fluxes in the Eastern Tropical South Pacific based on 234Th budgets and sediment trap deployments. Deep. Res. Part I Oceanogr. Res. Pap. 81, 1–13. doi:10.1016/j.dsr.2013.07.001

Heimbürger, L.E., Cossa, D., Marty, J.C., Migon, C., Averty, B., Dufour, A., Ras, J., 2010. Methyl mercury distributions in relation to the presence of nano- and

picophytoplankton in an oceanic water column (Ligurian Sea, North-western Mediterranean). Geochim. Cosmochim. Acta 74, 5549–5559. doi:10.1016/j.gca.2010.06.036

Kadko, D., Feely, R., Massoth, G., 1994. Scavenging of 234Th and phosphorus removal from the hydrothermal effluent plume over the north Cleft segment of the Juan de Fuca Ridge. J. Geophys. Res. doi:10.1029/93JB02952

Karl, D.M., Church, M.J., Dore, J.E., Letelier, R.M., Mahaffey, C., 2012. Predictable and efficient carbon sequestration in the North Pacific Ocean supported by symbiotic nitrogen fixation. Proc. Natl. Acad. Sci. U. S. A. 109, 1842–9. doi:10.1073/pnas.1120312109

Kennedy, P., Kennedy, H., Papadimitriou, S., 2005. The effect of acidification on the determination of organic carbon , total nitrogen and their stable isotopic composition in algae and marine sediment. Rapid Commun. Mass Spectrom. 19, 1063–1068. doi:10.1002/rcm.1889

Knauer, G.A., Martin, J.H., Bruland, K.W., 1979. Fluxes of particulate carbon, nitrogen, and phosphorus in the upper water column of the northeast Pacific. Deep Sea Res. Part A, Oceanogr. Res. Pap. 26, 97–108. doi:10.1016/0198-0149(79)90089-X

Lam, P.J., Marchal, O., 2015. Insights into Particle Cycling from Thorium and Particle Data. Ann. Rev. Mar. Sci. 7, 159–184. doi:10.1146/annurev-marine-010814-015623

Lam, P.J., Ohnemus, D.C., Auro, M.E., 2015. Size-fractionated major particle composition and concentrations from the US GEOTRACES North Atlantic Zonal

Transect. Deep. Res. Part II Top. Stud. Oceanogr. 116, 303–320. doi:10.1016/j.dsr2.2014.11.020

Lamborg, C., Bowman, K., Hammerschmidt, C., Gilmour, C., Munson, K., Selin, N., Tseng, C.-M., 2014. Mercury in the Anthropocene Ocean. Oceanography 27, 76–87. doi:10.5670/oceanog.2014.11

Lamborg, C.H., Hammerschmidt, C.R., Bowman, K.L., 2016. An examination of the role of particles in oceanic mercury cycling. Philos. Trans. R. Soc. A 374.

Lamborg, C.H., Hammerschmidt, C.R., Bowman, K.L., Swarr, G.J., Munson, K.M., Ohnemus, D.C., Lam, P.J., Heimbürger, L.-E., Rijkenberg, M.J. a., Saito, M. a., 2014. A global ocean inventory of anthropogenic mercury based on water column measurements. Nature 512, 65–68. doi:10.1038/nature13563

Maiti, K., Benitez-nelson, C.R., Rii, Y., Bidigare, R., 2008. Deep-Sea Research II The influence of a mature cyclonic eddy on particle export in the lee of Hawaii. Deep Sea Res. II 55, 1445–1460. doi:10.1016/j.dsr2.2008.02.008

Mende, D.R., Bryant, J.A., Aylward, F.O., Eppley, J.M., Nielsen, T., Karl, D.M., Delong, E.F., 2017. Environmental drivers of a microbial genomic transition zone in the ocean's interior. Nat. Microbiol. 2, 1367–1373. doi:10.1038/s41564-017-0008-3

Michaels, A.F., Silver, M.W., 1988. Primary production, sinking fluxes and the microbial food web. Deep. Res. 35, 473–490.

Motta, L.C., Blum, J.D., Johnson, M.W., Washburn, S.J., Popp, B.N., Drazen, J.C., Umhau, B.P., Benitez-nelson, C.R., Hannides, C.C.S., Close, H.G., n.d. Hg cycling

in the North Pacific Subtropical Gyre as revealed by Hg isotopes.

Munson, K.M., Lamborg, C., Swarr, G.J., Saito, M.A., 2015. Mercury species concentrations and fluxes in the Central Tropical Pacific Ocean. Global Biogeochem. Cycles 29, 656–676. doi:10.1002/2015GB005120.Received

Owens, S.A., Buesseler, K.O., Sims, K.W.W., 2011. Re-evaluating the 238 U-salinity relationship in seawater : Implications for the U – 234 Th disequilibrium method. Mar. Chem. 127, 31–39. doi:10.1016/j.marchem.2011.07.005

Owens, S.A., Pike, S., Buesseler, K.O., 2015. Thorium-234 as a tracer of particle dynamics and upper ocean export in the Atlantic Ocean. Deep Sea Res. Part II Top. Stud. Oceanogr. 116, 42–59. doi:10.1016/j.dsr2.2014.11.010

Pasulka, A.L., Landry, M.R., Taniguchi, D.A.A., Taylor, A.G., Church, M.J., 2013. Temporal dynamics of phytoplankton and heterotrophic protists at station ALOHA. Deep. Res. Part II Top. Stud. Oceanogr. 93, 44–57. doi:10.1016/j.dsr2.2013.01.007

Pike, S.M., Buesseler, K.O., Andrews, J., Savoye, N., 2005. Quantification of 234 Th recovery in small volume sea water samples by inductively coupled plasma-mass spectrometry. J. Radioanal. Nucl. Chem. 263, 355–360.

Puigcorbé, V., Benitez-nelson, C.R., Masqué, P., Verdeny, E., White, A.E., Popp, B.N., Prahl, F.G., Lam, P.J., 2015. Small phytoplankton drive high summertime carbon and nutrient export in the Gulf of California and Eastern Tropical North Pacific. Global Biogeochem. Cycles 1309–1332. doi:10.1002/2015GB005134.Received

Richardson, T.L., Jackson, G.A., 2007. Small Phytoplankton and Carbon Export from the

Surface Ocean. Science (80-.). 838–840. doi:10.1126/science.1133471

Selin, N.E., 2009. Global Biogeochemical Cycling of Mercury: A Review. Annu. Rev. Environ. Resour. 34, 43–63. doi:10.1146/annurev.environ.051308.084314

Siegel, D.A., Buesseler, K.O., Doney, S.C., Sailley, S.F., Behrenfeld, M.J., Boyd, P.W., 2014. Global assessment of ocean carbon export by combining satellite observations and food-web models. Global Biogeochem. Cycles 28, 181–196. doi:10.1002/2013GB004743.Received

Strode, S., Jaeglé, L., Emerson, S., 2010. Vertical transport of anthropogenic mercury in the ocean. Global Biogeochem. Cycles 24, 1–10. doi:10.1029/2009GB003728

Sun, R., Sonke, J.E., Heimbürger, L.E., Belkin, H.E., Liu, G., Shome, D., Cukrowska, E., Liousse, C., Pokrovsky, O.S., Streets, D.G., 2014. Mercury stable isotope signatures of world coal deposits and historical coal combustion emissions. Environ. Sci. Technol. 48, 7660–7668. doi:10.1021/es501208a

Weinstein, S.E., Moran, S.B., 2005. Vertical flux of particulate Al, Fe, Pb, and Ba from the upper ocean estimated from234Th/238U disequilibria. Deep. Res. Part I Oceanogr. Res. Pap. doi:10.1016/j.dsr.2005.03.008

Table 3.1 Particulate thorium (P Th), particulate carbon (PC), particulate nitrogen (PN) and particulate mercury (PHg) concentrations in 1-53 and > 53 µm size fractions.

		PTh (dpm/ L)	± Error	PC (nmol/ L)	± Erro r	PN (nmol/L)	± Err or	Hg (fmol/L)	± Err or
1-53 µm	**Feb. 2014**								
	25	0.12	0.01	859	86	137	10	72	4
	50	0.16	0.01	799	80	132	9	67	3
	75	0.24	0.02	727	73	126	9	70	3
	125	0.20	0.02	314	16	59	4		
	150	0.18	0.01	414	41	68	5	39	2
	175	0.15	0.01	251	25	55	3	29	1
	200	0.16	0.01	256	26	39	3	42	2
	400	0.14	0.01	188	19	30	2	26	1
	Sept. 2014								
	25	0.12	0.01	1528	153	223	19	87	4
	50	0.11	0.02	1339	134	236	17	82	4
	100	0.12	0.02	781	78	158	11	38	2
	125	0.11	0.01	548	55	117	10	25	1
	150	0.12	0.01	427	43	95	8	29	2
	175	0.14	0.02	230	23	68	3	25	1
	200	0.14	0.02	286	29	60	4	28	1
	250	0.13	0.01	238	24	68	5	27	1
	400	0.10	0.01	212	21	60	4	23	1

	May 2015								
	25	0.14	0.02	947	95	135	7	58	3
	50	0.19	0.02	961	96	132	7	54	3
	75	0.24	0.04	864	86	120	6	67	3
	150	0.21	0.03	418	42	63	3	25	1
	175	0.08	0.01	217	22	33	2	43	2
	200	0.15	0.01	286	29	40	2	37	2
	250	0.16	0.02	247	25	30	2	29	1
	400	0.07	0.02	180	18	20	1	22	1
>53 µm	**Feb. 2014**								
	25	0.0048	0.0003	70	5	14.9	0.7	3.3	0.2
	74	0.0125	0.0012	53	3	7.8	0.4		
	99	0.0257	0.0010	67	3	9.6	0.5		
	125	0.0192	0.0018	62	3	8.4	0.4		
	150	0.0180	0.0008	36	3	3.9	0.3		
	175	0.0139	0.0004	45	2	6.3	0.3		
	200	0.0093	0.0009	33	2	3.9	0.2		
	250	0.0085	0.0005	18	1	1.9	0.1		

400			17	1	1.6	0.1	1.4	0.1
Sept. 2014								
25	0.0027	0.0003	212	15	28.8	0.1		
50	0.0057	0.0002	112	6	20.0	1.0		
75	0.0110	0.0005	76	4	12.9	0.6		
125	0.0207	0.0019	80	6	9.5	0.1		
150	0.0279	0.0026	86	6	10.3	0.1	0.8	0.0
175	0.0225	0.0021	38	2	6.1	0.3		
200	0.0249	0.0023	56	3	8.8	0.4		
250	0.0132	0.0004	24	2	3.3	0.1		
400	0.0085	0.0004	26	2	2.9	0.2		
May 2015								
25	0.0105	0.0005	130	7	22.1	1.1		
50	0.0133	0.0006	191	10	32.1	1.6		
75	0.0211	0.0010	135	7	18.6	0.9		

125	0.0339	0.0013	82	4	9.6	0.5		
150	0.0133	0.0005	55	3	6.6	0.3	3.3	0.2
175	0.0133	0.0005	35	2	3.9	0.2		
200	0.0147	0.0014	33	2	3.5	0.2		
250	0.0158	0.0015	39	2	4.7	0.2		
400	0.0077	0.0006	20	2	1.8	0.1		

Table 3.2 Fluxes of total thorium (234Th) particulate carbon (PC), particulate nitrogen (PN) and particulate mercury (PHg) in the 1-53 and > 53 µm size fractions from pump samples.

	Depth	**Total Th-234 flux (dpm m^{-2} day^{-1})**	**± Error**	**PC flux (µmol m^{-2} day^{-1})**	**± Error**	**PN flux (µmol m^{-2} day^{-1})**	**± Error**	**PHg flux (pmol m^{-2} day^{-1})**	**± Error**
1-53 µm	**Feb. 2014**								
	25	125	6	920	119	144	24	77	7
	50	108	13	557	95	92	19	47	7
	75	48	13	144	42	25	10	14	4
	125	97	14	558	82	96	11		
	150	414	18	944	120	155	25	90	8
	175	596	18	1021	131	222	21	119	11
	200	355	23	579	98	89	14	95	11
	400	-10	28	-13	-38	-2	-11	-2	-5
	Sept. 2014								
	25	30	9	395	131	58	32	23	7
	50	116	30	1352	403	239	101	83	25
	100	265	34	1722	361	349	96	84	16
	125	469	56	2343	399	389	82	105	16
	150	590	65	2135	406	477	142	146	26
	175	684	34	1088	192	323	50	118	18

	200	836	121	1694	374	354	76	166	35
	250	1139	121	2109	339	664	131	237	33
	400	1546	210	3387	684	670	218	373	70
	May 2015								
	25	77	14	537	130	77	17	33	7
	50	239	16	1199	197	165	23	67	9
	75	269	16	972	191	135	24	75	13
	150	692	47	1392	256	211	34	83	13
	175	644	47	1844	308	283	40	362	52
	200	621	49	1156	155	160	16	150	15
	250	598	49	950	156	116	16	113	16
	400	818	53	2107	663	232	70	259	78
>53 µm	**Feb. 2014**								
	25			2116	186	387	34	84	10
	75			205	57	30	9	-	-
	100			252	41	36	6	-	-
	125			854	107	116	15	-	-
	150			912	73	90	44	-	-
	175			1918	126	272	18	-	-
	200			1250	155	149	18	-	-
	250			490	64	-		-	-
	Sept. 2014								

25	2328	1020	316	138	-	-
50	2797	755	519	140	-	-
75	2131	374	380	67	-	-
100	1266	1278	215	217	-	-
125	1822	411	215	48	-	-
150	1827	394	218	47	18	3
175	1147	132	186	21	-	-
200	1871	335	296	53	-	-
250	2078	357	287	49	-	-
400	4669	1003	525	113	-	-
May 2015						
25	947	187	161	32	-	-
50	3430	326	577	55	-	-
75	1725	153	238	21	-	-
125	1340	141	158	17	-	-
150	2870	267	342	32	174	11
175	1700	165	190	18	-	-
200	1481	200	148	20	-	-
250	1250	165	177	24	-	-
400	4128	567	187	20	-	-

Table 3.3 Sediment trap fluxes of particulate thorium (Th), particulate carbon (PC), and particulate nitrogen (PN) calculated from thorium ratios and directly measurements.

Sediment Trap		**^{234}Th flux** ***(dpm m^{-2} day^{-1})***	**Error** ±	**PC flux** ***(µmol m^{-2} day^{-1})***	**Error** ±	**PN flux** ***(µmol m^{-2} day^{-1})***	**Error** ±
Thorium Derived	**Feb. 2014**						
	150	-	-	2589	279	306	33
	Sept. 2014						
	150	-	-	2318	386	323	40
	May 2015						
	150	-	-	6253	585	842	91
Direct Trap Meas.	**Feb. 2014**						
	150	440	95	2530	127	290	15
	Sept. 2014						
	150	653	9	4169	493	581	22
	May 2015						
	150	454	22	4051	172	545	37

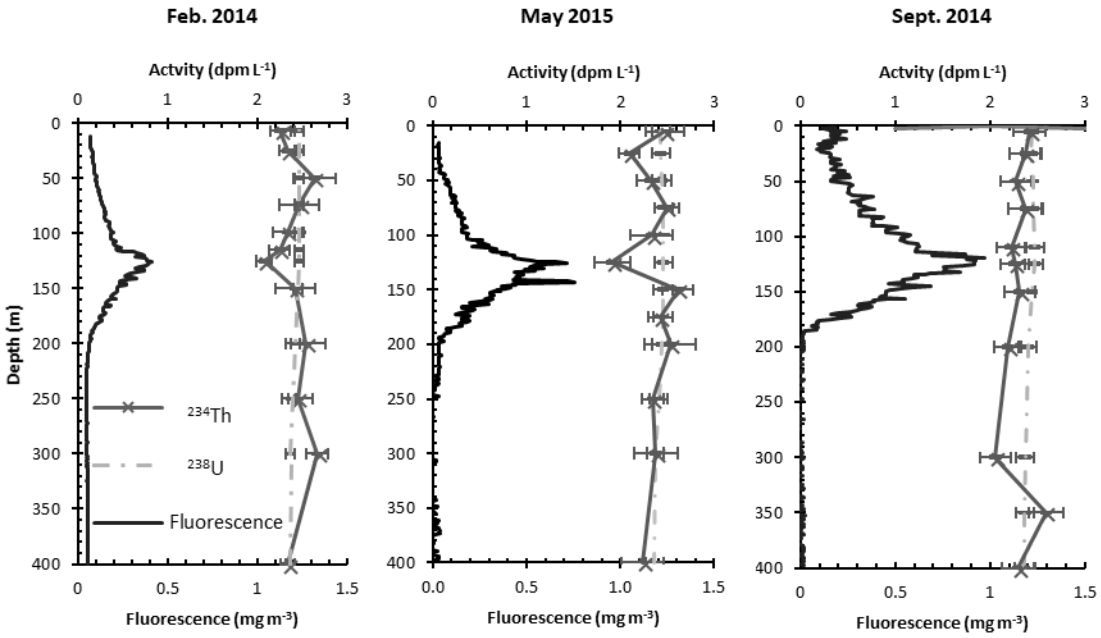

Figure 3.1 Plot of 234Th activity, 238U activity (upper axis), and fluorescence (lower axis) with depth in Feb. 2014, May 2015 and Sept. 2014. Error bars indicate standard error.

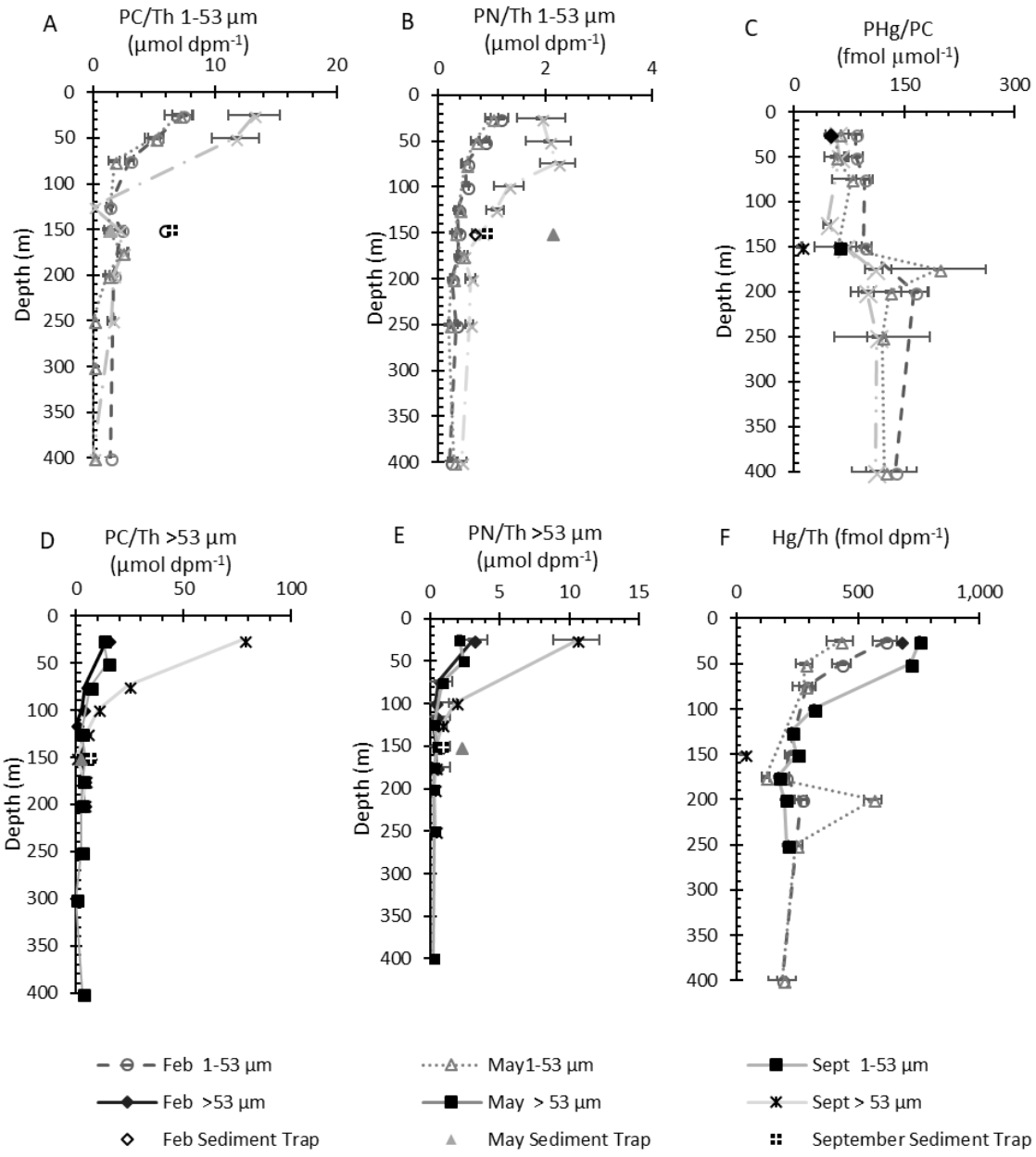

Figure 3.2 Vertical profiles of element ratios for small particle PC:Th (A), PN:Th (B) and large particle PC:Th (D), PN:Th (E), and all particulate PHg:PC(C) and PHg:Th (F). Abbreviations: PC, particulate carbon; POC, particulate organic carbobn; PN, particulate nitrogen; Th, particulate thorium; PHg, particulate mercury.

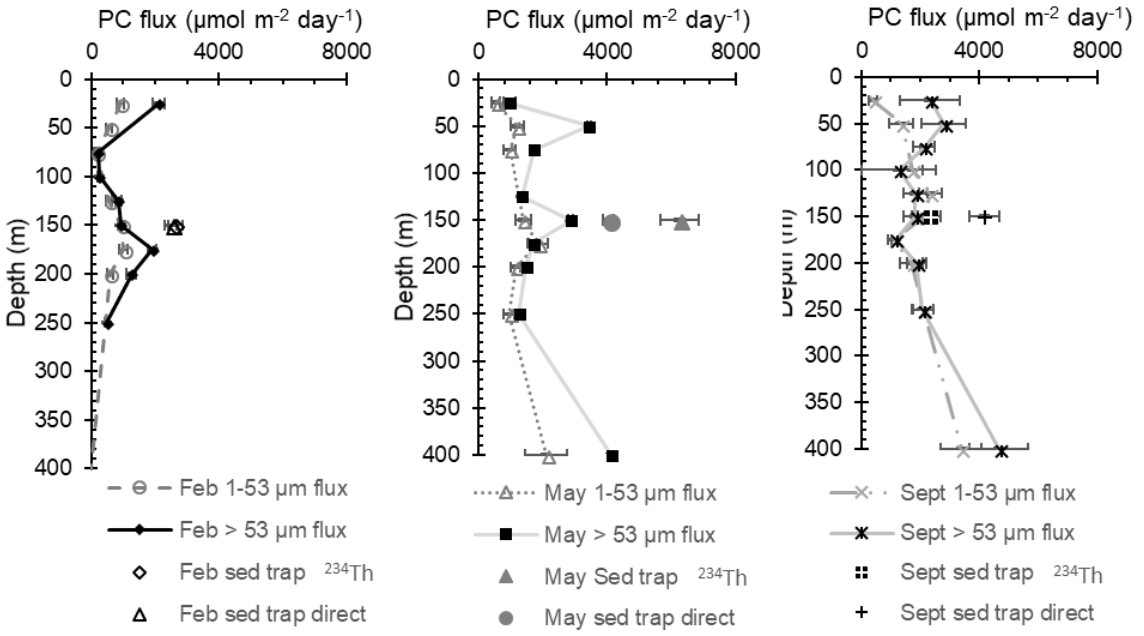

Figure 3.3 Plot of particulate carbon (PC) fluxes with depth for small (1-53 µm) and large (> 53 µm) particles derived using 238U-234Th disequillibria and in-situ pumps and sediment traps. Error bars indicated standard error.

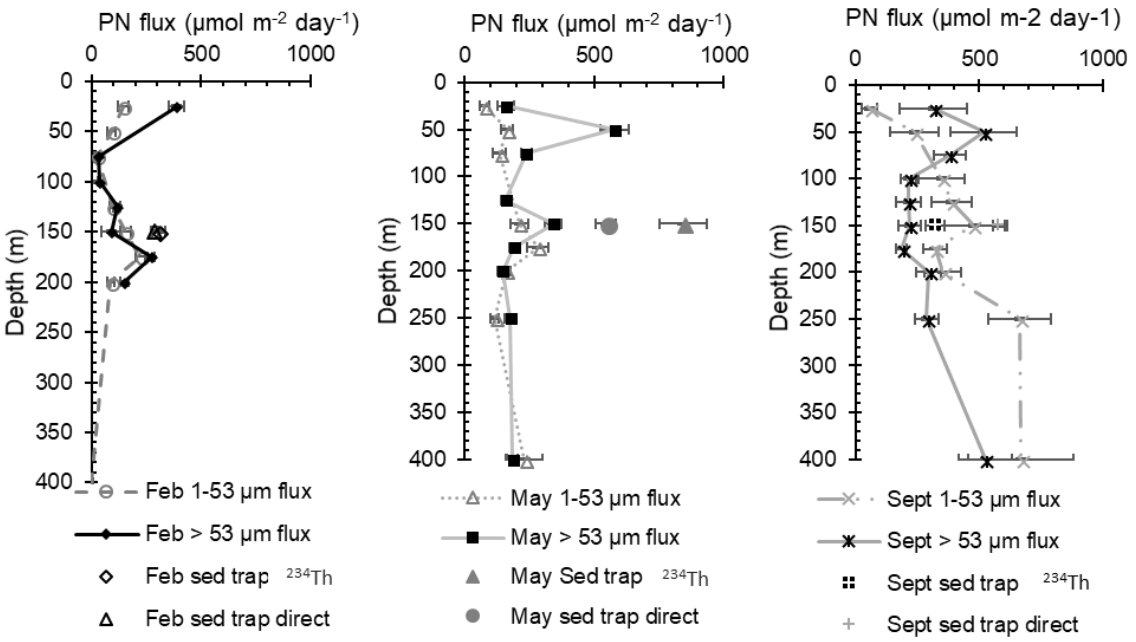

Figure 3.4 Plot of particulate nitrogen (PN) fluxes with depth for small (1-53 µm) and large (> 53 µm) particles derived using 238U-234Th disequillibria and in-situ pumps and sediment traps. Error bars indicated standard error.

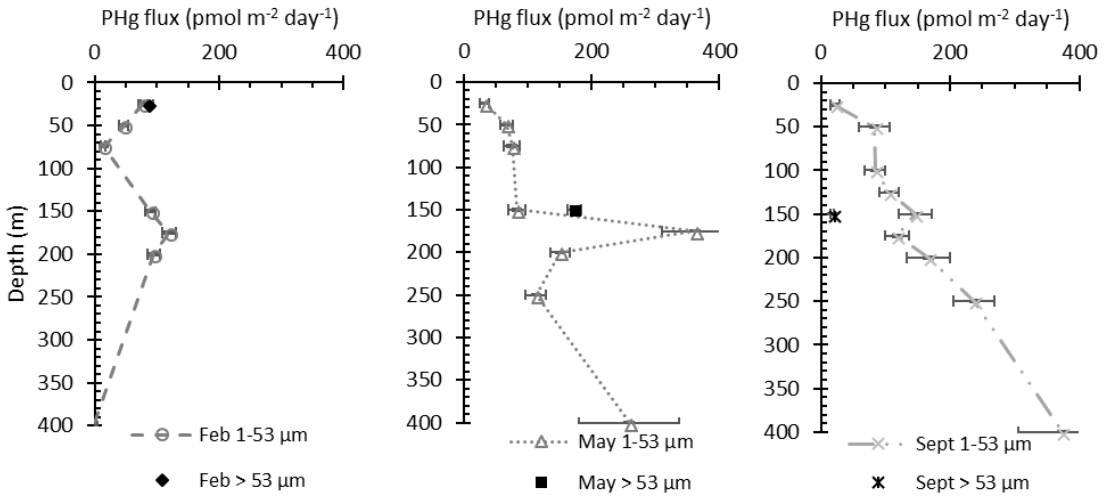

Figure 3.5 Plot of particulate mercury (PHg) fluxes with depth for small (1-53 µm) and large (> 53 µm) particles derived using 238U-234Th disequillibria and in-situ pumps. Error bars indicated standard error.

CHAPTER 4: PARTICULATE FLUXES OF CARBON, NITROGEN AND MERCURY ACROSS AN OXYGEN GRADIENT IN THE CENTRAL EQUATORIAL PACIFIC[3]

[3] Blaire P. Umhau, Laura Motta, Brian N. Popp, Claudia R. Benitez-Nelson, Joel Blum, Cecelia C. Hannides and Jeffrey C. Drazen. To be submitted to *Marine Chemistry*

Abstract

Particle dynamics are an essential component of global ocean biogeochemistry as they transport essential nutrients, carbon, and trace metals through the water column and facilitate the removal of pollutants, such as mercury (Hg), from surface waters. An important factor in particle cycling is dissolved oxygen abundance, which influences chemical speciation and microbial remineralization. The central Equatorial Pacific is the site of an oxygen minimum zone that shoals from below 400 up to 125 m with decreasing latitude toward the equator. In a transect along this gradient at 155°W between 5 and 17°N, the downward fluxes of particulate carbon (PC), nitrogen (PN) and total mercury (PHg) were determined over the upper 400 m using a combination of sediment traps and *in situ* pumps coupled with ^{238}U -^{234}Th disequilibria. PC fluxes at 150 ranged from below detection to 1340 µmol C m^{-2} day^{-1}, with fluxes from the upper 100 m highest at 5°N. All other sites were characterized by minimal PC export. PHg fluxes were also consistently low, except at 5°N where the flux determined from small and large particles was 61 and 36 pmol m^{-2} day^{-1} at 150 m, respectively. While PHg fluxes were similar at these stations, the in peak PHg flux within the upper 125 m was seven times higher at 5°N compared to 8°N, where the water column was fully oxic. Below 200 m, remineralization was again the dominant process. These results suggest that dissolved oxygen plays a very important role in PC and PHg cycling at the base of the euphotic zone, likely due to its influence on food web activity, specifically zooplankton and upper trophic level grazing.

Keywords: Particle flux, Uranium-238, Thorium-234, Mercury, Equatorial Pacific

4.1. Introduction

Characterizing the magnitude and composition of particles as they sink from the ocean's surface to its depths is crucial for describing carbon, trace element, and nutrient biogeochemical cycling (Buesseler et al., 2008). Particles can include lithogenic and other inorganic material, senescent phytoplankton, zooplankton molts and fecal pellets, any of which may form larger aggregates (Buesseler et al., 2008; Lam et al., 2015). Although small particles (1-53 µm) may sink more slowly than larger ones, small particles have been recognized as important contributors to vertical flux as well (Puigcorbé et al., 2015; Richardson and Jackson, 2007) and play an especially vital role in trace element and isotope scavenging and cycling due to their high surface area (Lam et al., 2015). Both particle types provide a potential food source of nutrients and trace elements to higher trophic levels (Alonso-Gonzalez et al. 2010; Choy et al. 2015; Durkin et al. 2015; Lam et al. 2015; Puigcorbé et al. 2015; Hannides et al., submitted). Therefore, scavenging and biologically mediated uptake of dissolved seawater constituents onto and into particles is an important mechanism for the introduction and subsequent bioaccumulation of trace elements in marine biota (Lam et al., 2015; Lamborg et al., 2016).

One valuable proxy for measuring sinking particle flux on the order of days to weeks is the disequilibrium between Uranium-238 (^{238}U) and Thorium-234 (^{234}Th) (Benitez-Nelson et al., 2001; Buesseler et al., 2009). Uranium-238 is a long-lived radioisotope ($t_{½}$ =4.5 x 10^9 years) and a conservative component of seawater; its radiogenic daughter, ^{234}Th, is short-lived ($t_{½}$=24.1 days) and highly particle reactive. As such, the particulate distribution of ^{234}Th has been used to constrain carbon (Buesseler et

al., 2009; Haskell et al., 2013; Owens et al., 2015), nutrient (Kadko et al., 1994; Maiti et al., 2008; Puigcorbé et al., 2015), and trace metal exports in a range of environments (Lamborg et al., 2016; Weinstein and Moran, 2005). The trace metal Mercury (Hg) scavenges onto particles. It is a potent toxin, both in its elemental form and in the form of methylated compounds (MeHg), dimethylmercury (DMHg) and monomethylmercury (MMHg) (Fitzgerald and Lamborg, 2003). MMHg is especially toxic and of concern because once it is introduced into the ecosystem, it bioaccumulates and is biomagnified within fish, which are commercially harvested for human consumption (Fitzgerald and Lamborg, 2003; Selin, 2009). Choy et al. (2009) found that Hg concentrations in pelagic fish increased with depth and an important source of Hg to the marine food web is in the mesopelagic zone. Recent work further indicates that Hg methylation occurs below the surface mixed layer (Blum et al., 2013). These observations suggest that both surface and subsurface processes are important in determining the magnitude of Hg incorporation into the mesopelagic marine food web (See Cossa et al., 2012). Unfortunately, information regarding the flux and transformation of PHg in the water column remains very limited. In one of the few studies to examine PHg export, Munson et al. (2015) found PHg fluxes to range from below detection to as high as 123 pmol m^{-2} day^{-1} at 150 m in the central North Pacific. No other data in this region is currently available.

Particulate mercury has been shown to be methylated at higher rates in low oxygen zones due to increased activity of methylating microbes (Blum et al., 2013; Munson et al., 2015). Additionally, dissolved oxygen concentrations may impact microbial remineralization of other trace elements as most bacterial degradation occurs in very low or anoxic environments (Bianchi et al., 2018; Blum et al., 2013; Choy et al.,

2009). At the same time, however, oxygen minimum zones may also experience increased POC fluxes, and it has been hypothesized that specific remineralization processes that depend on oxygen availability are less effective (Black et al., 2018; Cavan et al., 2017). Therefore, dissolved oxygen concentration is an important parameter to consider when studying particle dynamics, particularly with regards to Hg cycling.

Through the use of free floating sediment traps, *in-situ* pumps and ^{234}Th-^{238}U disequilibria, this study examined how particle fluxes changed along a north-south transect that stretched from 17 to 5^{o}N at 155^{o}W covering a range of oxygen regimes. PHg fluxes were determined using both small and large particles coupled with ^{238}U-^{234}Th disequilibria. Spatial changes in PC and PN fluxes and concentrations as well as dissolved oxygen concentrations were also examined in relation to particulate Hg and particulate Hg fluxes.

4.2. Methods

4.2.1 Sample Collection

Samples were collected at six stations from mid-August to mid-September 2015 (Fig. 4.1). All stations were located on a north-south transect line along 155^{o}W (See Table 4.1). Stations 1-4 were occupied for approximately four hours, with the CTD, 24 Niskin bottle carousel and two pumps deployed within a single cast. Stations 5 and 6 were occupied for nine days, with multiple casts. Salinity, temperature, fluorescence and oxygen measurements (Figure 4.2) were obtained from a Seabird SBE 9/11plus CTD deployed with two Sea-Bird SBE 3P temperature sensors, two Sea-Bird SBE 4C conductivity sensors and two Sea-Bird SBE 43 dissolved oxygen sensors, and a Wetlabs

ECO FLNTU Chlorophyll Fluorometer & Turbidity sensor. ^{238}U was calculated using the equation in Owens et al. (2011) and salinity measurements (Eq. 4.1).

$$^{238}U \text{ (dpm } L^{-1}) \pm 0.047 = 0.0786 \text{ x Salinity} - 0.315 \quad \text{(Eq. 4.1)}$$

Total ^{234}Th samples were collected and analyzed at all stations using 2 L of seawater collected from selected depths between 5 and 400 m (N = 12-14) with two additional samples taken between 2500 m and 4300 m at stations 5 and 6. After collection, samples prepped for analysis using the methods described in Buesseler et al. (2001) and Benitez-Nelson et al. (2001). Briefly, seawater was spiked with ^{230}Th as a yield tracer and acidified to pH ~ 1 using concentrated nitric acid, $KMnO_4$ and $MnCl_2$ were added and the pH adjusted to ~ 9 with concentrated to NH_4OH. After eight hours, samples were filtered onto 25 mm QMA filters and air dried. Once dry, samples were covered with mylar followed by combusted aluminum foil and frozen. Initial ^{234}Th counts were made at sea immediately after collection, using a low level RISO beta counter. Samples were recounted after six months to obtain background counts. Thorium recoveries were measured using ICP-MS according to the methods described in Pike et al., (2005). Briefly, after background counts were obtained, precipitates were dissolved using 8M HNO_3/10% H_2O_2, and the solution spiked with ^{229}Th as a recovery tracer. The solution was sonicated for 30 min, allowed to stand overnight, and then evaporated to less than 1 mL, rinsed with HNO_3 and evaporated again before a 10% HNO_3/1% HF solution was added to obtain a final 2 ml volume. Samples were filtered through a 0.2 µm filter to avoid clogging the ICP-MS capillary.

McLane WTS-LV pumps were deployed with two sequential filters sizes mounted on metal-free filter holders to capture small and large sinking particulates in the >53 µm and 1-53 µm size range using 142 mm Nitex and QMA filters, respectively, according to the methods described by Lam et al (2015). Filters analyzed for PC and PN were pre-combusted and stored in combusted foil prior to use. Pumps were deployed to 145 and 155 m at stations 1 - 4 and at depths between 10 and 400 m (N = 11) at stations 5 and 6. Pump volumes ranged between ~ 600-6000 L per deployment at a rate of 3 - 29 L min^{-1}. Flow rates above 8 L min^{-1} were only used to collect large particles. The QMA filters were sub-sampled under trace metal clean conditions in triplicate using a ~ 25 mm Delrin punch for particulate ^{234}Th analysis and the remaining filter was analyzed for total mercury, and mercury isotopes (see Motta et al., submitted). The majority of samples for 1-53 µm PC and PN were also collected from the same filter using the Delrin punch. All samples were immediately frozen at -80˚C. Large particle (> 53 µm) samples were collected using acid cleaned (10% HCl) Nitex filters, rinsed onto 25 mm QMA filters using filtered seawater, mounted onto RISO discs, and immediately frozen at -80˚C prior to analysis for ^{234}Th, PC, and PN. Additional large particle samples for Hg analyses were collected on separate deployments at rates of 15 - 29 L min^{-1} using acid cleaned Nitex screens (53 µm) and were frozen whole, stored in trace metal clean petri dishes. In addition to using the McLane pumps, particle interceptor style (PIT) sediment traps were deployed for ~ 3 days at 150 and 155 m at Stations 5 and 6 and material filtered onto 142 mm QMAs that were sub-sampled and analyzed for particulate ^{234}Th, PC, and PN (Knauer et al., 1979).

4.2.2 Analyses

Particle fluxes were derived using ^{234}Th:^{238}U disequilibrium, determined by calculating the ^{234}Th flux (dpm m^{-2} d^{-1}) using Equation (4.2), which assumes steady state and minimal physical processes:

$$(A_{238U}-A_{234Th})*\lambda_{234Th}*z = {}^{234}\text{Th flux} \quad \text{(Eq. 4.2)}$$

Where, A_{238U} is the ^{238}U activity (dpm L^{-1}), A_{234Th} is the measured ^{234}Th activity (dpm L^{-1}), λ_{234Th} is the radioactive decay constant for ^{234}Th (0.02876 d^{-1}) and z is the depth interval of interest (in m). ^{234}Th fluxes were calculated across specific depth ranges based on sampling depths, then added to the fluxes calculated from overlying depths to find the total flux across a specific depth horizon (Buesseler et al., 2009). Physical processes are assumed to be negligible as there was no evidence of mesoscale features during sample collection (i.e., upwelling). Small and large particle element to ^{234}Th ratios at a given depth horizon (e.g., PHg/Th) were multiplied by the ^{234}Th flux at that depth horizon to determine ^{234}Th derived fluxes of PC, PN, and PHg throughout the water column (Buesseler et al., 2006). Small and large particle element to ^{234}Th ratios were each used to determine fluxes as well as element to ^{234}Th ratios measured in the sediment traps deployed at 150 m.

All THg samples were measured by the Blum laboratory at the University of Michigan according to the methods described in Motta et al. (Submitted) and Biswas et al. (2008). Briefly, small particles underwent microwave assisted digestion, then samples were measured for total Hg by cold vapor atomic absorption spectroscopy (CV-AAS). Large particle samples from the same depth were combined and rinsed onto QMA filters

that were then lyophilized. Total Hg was extracted from filters using a two-step combustion-oxidation process then measured for Hg using CV-AAS. Particulate C and PN samples were analyzed by the Popp laboratory at the University of Hawaii according to the methods described in Kennedy et al. (2005). Briefly, once ashore, samples were dried overnight at 60°C and then encapsulated in tin cups for analysis of PC and PN concentrations. Carbon and nitrogen content and isotopic composition of all filters were determined using an isotope ratio mass spectrometer (IRMS; Delta ^{Plus}XP) coupled to an elemental analyzer (Conflo IV/Costech ECS 4010). Samples analyzed for particulate organic carbon (POC) and were subjected to decarbonation using sulfurous acid prior to analysis (Kennedy et al., 2005).

4.3. Results

4.3.1 Oxygen, Fluorescence, Temperature and Salinity

Oxygen concentrations varied between 180 and 200 µmol kg^{-1} from the surface down to ~ 50 m, except at Station 3, where concentrations increased above 200 µmol kg^{-1}. The depth of the oxygen minimum zone (< 30 µmol kg^{-1}) decreased with latitude until 8^{o} N. It reached a minimum depth of ~125 m at stations 4 and 5 before dropping down below 400 m at station 6. The mixed layer was shallowest at stations 2 and 3, only reaching 25 m, and deepest at station 6 with a depth of 60 m. Surface salinity also decreased with latitude, from 34.6 at station 1 to 33.8 at station 6. Fluorescence peaked at all stations below the mixed layer, between 50 and 150 m (Figure 4.3).

4.3.2 Total ^{234}Th

Total ^{234}Th activities were generally high, and in many instances were the same, within error as the calculated ^{238}U activities, indicating low particle formation (^{238}U activity > ^{234}Th activity = ^{234}Th deficit, particle formation). In certain instances at depth, ^{234}Th activities were even higher than ^{238}U, indicating extensive particle remineralization (^{234}Th activity > ^{238}U activity = ^{234}Th excess, remineralization). Total ^{234}Th activities ranged from 1.4 to 3.2 dpm L^{-1}, with the most particle formation occurring at station 3 over the upper 100 m. Remineralization features observed at all stations below 125 m (Figure 4.3).

4.3.3 Particle Concentrations

Small particle (1- 53 µm) ^{234}Th activities ranged from 0.13 to 0.72 dpm L^{-1}, with both extremes measured at station 6 (Table 4.1). The average 1-53 µm activity at 150 m across all stations was 0.17 ± 0.04. At Stations 5 and 6, small particulate ^{234}Th activities decreased with increasing depth from 0.72 dpm L^{-1} (Station 6) and 0.48 dpm L^{-1}(Station 5) at the surface to 0.14 dpm L^{-1} (Stations 5 and 6) at 400 m. POC comprised on average 80 ±17 % of small PC, with the lowest (41%) and highest (100%) percentages found at station 5 at 150 and 25 m, respectively. Small POC concentrations peaked at Station 5 (1837 nmol L^{-1}) at a depth of 50 m and again at stations 6 (1237 nmol L^{-1}) at a depth of 75 m, which is just above the fluorescence maximum at both stations. Small POC concentrations at 150 m were lowest at Station 4 (275 nmol L^{-1}) and highest at Station 1 (487 nmol L^{-1} Table 4.1). Small PN and PC concentrations followed similar trends as POC concentrations (Table 4.1). POC concentration at 150 m decreased with latitude at

stations 1-5, but did not appear to change with oxygen concentration at 150 m. At Station 5, small PHg concentrations were highest at the surface (88 fmol L^{-1}) then declined with depth to 24 fmol L^{-1}. At Station 6, PHg concentrations peaked at 25 and 125 m with concentrations of ~ 65 fmol L^{-1}. Similar to PC and PN, there were no trends in small PHg concentrations with latitude (Table 4.1).

Large particulate ^{234}Th activities (> 53 µm) ranged from 0.01 to 0.15 dpm L^{-1} and were an order of magnitude lower those measured in the small particles. At 150 m, large particulate ^{234}Th activities increased with decreasing latitude (Pearson correlation $p<0.01$, Table 4.1). Large PC concentrations ranged from 19 - 166 nmol L^{-1}. Sub-surface maximum PC concentrations were present at both Station 5 (75 m) and Station 6 (125 m). POC concentrations were approximately 10 ± 5% of large PC concentrations, a much smaller percentage compared to the small size fraction (t-test $p<0.01$). At 150 m, POC averaged 4 ± 1 nmol L^{-1} Large PN concentrations were an order of magnitude lower than small PN concentrations and followed similar trends to large PC concentrations. There is not enough large PHg data to discern trends, however large PHg concentrations were an order of magnitude lower than those measured in the smaller particle fraction at the same depths and averaged 2.3 ± 1.2 fmol L^{-1}.

4.3.4 Elemental Ratios

Small particulate PC to ^{234}Th ratios averaged ~ 1.9 ± 0.9 µmol dpm^{-1} throughout the water column at Stations 5 and 6, excluding a single high peak, 6.7 µmol dpm^{-1} at 50 m at station 5, and 16 µmol dpm^{-1} at 75 m at Station 6 (Figure 3). Across stations at 150 m, small PC/Th ratios were highest at station 1 (3.8 µmol dpm^{-1}) and varied with latitude

to Stations 5 (1.2 µmol dpm^{-1}) and 6 (1.4 µmol dpm^{-1}). Small POC/Th ratios followed the same trend as small PC ratios, but the ratio was slightly lower, average 1.5± 0.9 µmol dpm^{-1} at Stations 5 and 6, and the peak at Station 6 only reached 11 µmol dpm. PN/Th ratios also followed a similar pattern (Figure 3). Variations in PC (PN)/Th ratios across all Stations and depths were almost entirely driven by variations in PC (PN) concentrations rather than ^{234}Th activities.

Large particle PC/Th ratios at Station 5 covered a smaller range of values (0.2 - 3.3 µmol dpm^{-1}) than at station 6 (0.2 - 8.1 µmol dpm^{-1}). For both stations, ratios were highest at the surface and decreased rapidly to 25 m and remained low (~ 1.3 µmol dpm^{-1}) down to 400 m except for a small peak at Station 6 at 100 m (Figure 3). Across all stations at 150 m, large PC/Th ratios were lowest at Station 6 (1.0 µmol dpm^{-1}) and highest at Station 1 (2.8 µmol dpm^{-1}). Large POC/Th ratios were much lower than large PC/Th ratios but exhibited the same trend of decreasing rapidly from the surface at Stations 5 and 6. Below 100 m, PC/Th ratios converge, averaging 1.6 ± 0.1 µmol dpm^{-1} and 1.3 ±0.3 µmol dpm^{-1} for small and large PC/Th ratios, respectively. The PN/Th ratio followed the same trends.

Compared to the POC/Th ratios measured in the sediment trap, pump-collected 1 - 53 µm POC/Th ratios were ~ 2.5 times higher at station 6 (Table 4.3, 4.7). At station 5, small POC/Th ratios were only ~ 60% of sediment trap POC/Th and POC/Th ratios. Large POC/Th ratios are much lower, only ~12 % of trap POC/Th, at Stations 5 and 6 (Table 4.4, 4.7). At Station 5, PN/Th ratios from the pumps for both size fractions were slightly higher (avg 1.4 times higher) than trap PN/Th. At Station 6, PN/Th ratios from

both small and large pump size fractions were lower (only 82% and 39% of trap ratios) than sediment trap PN/Th.

In order to determine potential differences in bioaccumulation versus surface adsorption, we further examined PHg/PC ratios. Ratios of small PHg/PC are slightly different between Stations 5 and 6. Station 6 PHg/PC generally increases stepwise from 5 - 400 m, whereas at Station 5, PHg:PC decreases rapidly in the first 25 m, then increases stepwise to 250 m before decreasing to 400 m (Figure 4.4). When comparing all stations at 150 m, PHg:POC was highest at Station 4 (92 fmol μmol^{-1}) and lowest at station 1 (53 fmol μmol^{-1}). In the large particle fraction, PHg:PC was highest at Station 6 at 150 m (99 fmol μmol^{-1}) and lowest at Station 5 at 150 m (31 fmol μmol^{-1}).

Small particle Hg/Th ratios increased with depth down to 25 m at Stations 5 and 6. Ratios spanned a wider range at Station 6 (30 -311 fmol L^{-1}) than at Station 5 (110-232 fmol L^{-1}). Both stations show peaks at 125 m, with PHg/Th ratios increasing gradually below 250 m. These changes with depth were again driven almost entirely by changes in PHg concentrations. Across stations, the highest ratio at 150 m occurred at Station 4 (207 fmol dpm^{-1}) and the lowest at Station 5 (110 fmol dpm^{-1}). This ratio varies across latitude and oxygen concentrations, but there is no discernable trend. Given the limited PHg data on large particles, it was not possible to examine latitudinal and depth trends; the large PHg/Th ratio was highest at 400 m at Station 6 (151 fmol dpm^{-1}) and lowest at Station 5 at 150 m (45 fmol dpm^{-1}). Hg was not measured in the sediment traps.

4.3.5 Elemental particle fluxes derived using ^{234}Th:^{238}U disequilibrium

Water column derived ^{234}Th fluxes ranged from below detection (< 224 dpm $m^{-2}day^{-1}$) to 725 dpm m^{-2} day^{-1} (100 m, Station 3) Across stations at 150 m, small and large particle derived fluxes ranged from below detection (Stations 1, 2, 4, 5) to 515 dpm m^{-2} day^{-1} (Station 3). ^{234}Th fluxes determined from ^{234}Th:^{238}U disequilibria at 150 m were lower than those determined using sediment traps, which averaged 96 dpm $m^{-2}day^{-1}$ (Table 4.7). Small particle derived POC fluxes at Station 5 increased to a max of 1595 µmol m^{-2} day^{-1} at 50 m before decreasing to below detection at 150 m and remaining there to 400 m. At Station 6, the small particle derived POC flux increased from the surface down to 175 m (3629 µmol m^{-2} day^{-1}) before decreasing below detection at 300 m. Fluxes of large particle derived PC at Station 5 were higher than those derived using small particles in the upper 50 m but were similar below 75 m and decreased gradually with depth (Figure 4). At Station 6, small and large particle derived PC fluxes were similar, with the exception of a peak at 75 m observed in the small particle derived PC flux. Across stations, POC fluxes in both size fractions followed the same trend as PC fluxes, although POC fluxes using the large size fraction are much lower than large particle PC flux estimates, 50% and 15% of PC fluxes at Stations 3 and 6, respectively (Table 4.6, Figure 4.5). PN fluxes at Stations 5 and 6 and across all stations at 150 m followed the same trends as PC fluxes (Figure 4.5).

Particulate Hg fluxes ranged from below detection (remineralization) to 140 pmol m^{-2} day^{-1}. Small particle derived PHg fluxes were higher at Station 6, averaging 67 ± 49 pmol m^{-2} day^{-1} between 25 m and 125 m before decreasing below detection [1] at 300 m. At Station 5, small particle derived fluxes were lower, decreasing from the surface to 25 m,

and then increasing again to ~ 23 ± 26 pmol m^{-2} day^{-1} down to 150 m. Below 150 m, fluxes decreased to below detection. At 150 m, small particle derived PHg fluxes were only measurable at Station 6 (61 pmol m^{-2} day^{-1}) and below detection at all other stations. At Station 5, the large particle derived PHg flux was below detection, compared to 36 pmol m^{-2} day^{-1} at Station 6 at 150 m (Table 4.3).

Sediment trap fluxes were calculated both by direct measurement of material per square meter per time deployed, and by multiplying the water column derived ^{234}Th flux by the element to ^{234}Th ratio measured in the trap material (Table 4.7). Direct measurements resulted in a smaller range of fluxes than calculations via the particle to ^{234}Th ratio, which resulted in a wide range fluxes. This difference was more pronounced at Station 5, with PC fluxes calculated from water column ^{234}Th measurements below detection versus directly measured PC fluxes of 128 µmol m^{-2} day^{-1}. POC fluxes directly measured in the traps were the same at Stations 5 and 6 (66 ± 6 µmol m^{-2} day^{-1}). Using water column ^{234}Th measurements, POC fluxes were determined to be 218 µmol m^{-2} day^{-1} at Station 6 and below detection at Station 5. PN flux at Station 6 was three times higher than those measured at Station 5 when directly measured by the sediment trap, two orders of magnitude higher when calculated via ^{234}Th (Table 4.7). Mercury concentrations were not determined in sediment trap material due to contamination concerns.

4.4. Discussion

Sinking particles are a major pathway for transporting material from the surface ocean to the mesopelagic(Siegel et al., 2016). Thus they play a critical role in the oceans' capacity to act as a sink for atmospheric carbon dioxide, serve as a food source, and as a

mechanism for the transfer of contaminants through the food web (Buesseler et al., 2006; Siegel et al., 2014). Carbon and essential nutrients such as N have been the focus of most particle flux studies, partially because of the role they play in climate regulation, but also because of their role in the food web (Buesseler et al., 2009, 2006; Lam et al., 2015; Owens et al., 2015). There has been significantly less attention on trace element and contaminant particle fluxes, such as mercury (e.g., Lam et al., 2015). While inorganic mercury is particle reactive, MMHg bioaccumulates in organism tissues and human consumption of contaminated fish poses a health risk (C. Lamborg et al., 2014). Thus, the biogeochemical cycling of Hg in marine systems fundamentally differs from C and N, with Hg entering and remaining in the food web dependent on speciation. Low oxygen zones, such as the midwaters characteristic of the central Equatorial Pacific, may also play a role in Hg speciation, as mercury methlyation is often associated with intense microbial activity in these regions, although exact mechanisms are not well understood (Blum et al., 2013; Hammerschmidt and Bowman, 2012; Heimbürger et al., 2010). While low oxygen facilitates Hg cycling, the reverse is true for C; POC fluxes attenuate more slowly in low oxygen regimes because remineralization methods dependent on oxygen. For example, zooplankton grazing are less effective within low oxygen zones (Cavan et al., 2017).

4.4.1 Thorium activities

Previous studies in the region are limited, however the total ^{234}Th:^{238}U disequilibria profiles, ^{234}Th fluxes, and small/ large particulate ^{234}Th activities measured in this study are similar to previous investigations in the central Pacific, albeit with fluxes in the lower end of the range. For example, in a transect along 140°W from 12°S to 12°N,

Murray et al. (2005) found that the ^{234}Th:^{238}U ratio generally increased with depth at all stations, showing particle formation above 150 m and substantial remineralization below. At 10ºS, 152ºW, Black et al. (2018) also reported a transition from ^{234}Th deficits to excess ^{234}Th relative to ^{238}U near 150 m. In this study, significant ^{234}Th deficits were only observed at Stations 3 and 6 (12 and 5ºN) with remineralization generally occurring between 100 and 150 m. These differences are likely due in part to sampling location; Murry et al. (2005) and Black et al. (2018) were farther east and south, closer to the upwelling zone that would have higher particle fluxes from increased primary production (Dunne et al., 2000).

High ^{234}Th activities relative to ^{238}U resulted in generally small ^{234}Th deficits throughout the water column. As a result, the ^{234}Th fluxes measured at 150 m in this study were low, averaging 258 ± 155 dpm m^{-2} day^{-1}, excluding negative numbers. Using ^{234}Th deficits to calculate fluxes results in high uncertainties due to the combination of error propagation and repeated measurements when using the 1-D steady state model (Buesseler et al., 2009). As we were only able to measure a single profile at the majority of stations, our flux errors should be considered minimum estimates as they are based solely on measurement uncertainties. Buesseler et al. (2009) determined that the minimum flux that could be detected was 125 dpm m^{-2} day^{-1}, and this detection limit increased to 395 dpm $m^{-2}day^{-1}$ when non-steady state processes were included. Our results differ from the water column derived ^{234}Th fluxes of 1200 ± 400 dpm m^{-2} day^{-1} measured at 180 m by Black et al. (2018) and direct sediment trap ^{234}Th fluxes by Murray et al. (1996) along 140ºW from 12ºS to 12ºN, which ranged from ~1000 - 2500 dpm m^{-2} day^{-1} at 150. The ^{234}Th sediment trap fluxes Murray et al. (1996) calculated including

advection terms spanned a wider range, ~500-2500 dpm m^{-2} day^{-1}. Regardless, our cumulative range of direct sediment trap and water column ^{234}Th fluxes at 150 m (>144 ±22 dpm m^{-2} day^{-1}) are much lower than those measured previously, albeit in nearby locations subject to different physical processes, such as upwelling.

4.4.2 Particulate C, N, and Hg Concentrations

Primary production, and subsequently C flux, has been shown to decrease dramatically from ~2°N to both the north and south along a meridional gradient in the central equatorial Pacific. Between 5 and 10°N, primary production decreases from ~ 40 mmol C m^{-2} day^{-1} to ~ 20 mmol C m^{-2} day^{-1} and this gradient is less pronounced during El Nino conditions (Hernes et al., 2001; Lundry et al., 1997). Overall, average small PC (615 ± 490 nmol L^{-1}), POC (506 ± 416 nmol L^{-1}) and PN (81 ± 70 nmol L^{-1}) concentrations at all stations and depths were on the lower end, but within range of those previously measured (e.g., Buesseler et al. 1995; Lam et al. 2018). Large PC (avg. 50 ± 9 nmol L^{-1}) are smaller by an order of magnitude and large POC by two orders of magnitude (avg. 5 ± 0.4 nmol L^{-1}) than previous studies in proximal locations dominated by upwelling (Buesseler et al., 1995; Lam et al., 2018). The dramatic decreases in small and large PC, POC, and PN concentrations with increasing depth at Stations 5 and 6 occur at the same depth as a dramatic decrease in fluorescence (Figure 2).

The difference in percent of PC that is POC in small (80% POC) and large (10% POC) particles is likely due to a change in the composition of the particles. In a transect of the equatorial south Pacific, Lam et al. (2018) found small particles maintained a consistently high ratio of POC to PC moving east to west, but large PC was increasingly

dominated by inorganic carbon moving westward. By 140°W, large particle composition was 50% inorganic carbon, and only 25% organic material, consistent with our results at 150°W. This change may be due in part to a shift in the phytoplankton assemblage, such as an increase in foraminifera (Lam et al., 2018).

Small particulate Hg concentration profiles measured at Stations 5 and 6 and are consistent with those measured by Munson et al. (2015), which ranged from ~20 - 60 fmol L^{-1}. At station 1, PHg concentrations were the same, within error, of Munson et al.'s (2015) measured at 17°N as well (Table 4.1). Munson et al. (2015) found that PHg concentrations at 150 m increased moving northward from the equator due to decreased rainfall farther north; our results show PHg concentrations at 150 m remaining relatively constant with latitude (28 ± 5 fmol L^{-1}).

4.4.3 Element/Th ratios

Element to thorium ratios are a critical component of estimating ^{234}Th based water column fluxes of an element or compound of interest (Buesseler et al., 2006). Ratios can change with depth due to a variety of physical, biological and chemical processes, ranging from changes in particle surface area to bacterial reworking, and thus will vary based on particle size and water column dynamics (Buesseler et al., 2006; Lam et al., 2015). Peaks in the small PC/Th ratios at 50-75 m at Stations 5 and 6 (Figure 4.4) occur just above the subsurface peak in fluorescence (Figure 4.3) and is driven by a large increase in PC concentrations. There is no similar peak in the PC/Th ratio in the large particles. This indicates that there is subsurface production of small PC, but not large PC, and is likely associated with picoplankton found in this region (Black et al., 2018)

Different POC/PN ratios for small and large size particle fractions indicate that small phytoplankton may play a role in this difference (Lam et al. 2018). PC/Th ratio profiles in both small and large size classes below 100 m at Stations 5 and 6 were both lower, and the same, within error, respectively, indicating that similar processes may be influencing both size fractions, such as aggregation of small particles into larger ones, or disaggregation of large particles.

PC/Th ratios are higher than those found at 180 m by Black et al. (2018), which was 0.7 ± 0.01 at 12°S and 152°W and on the low end of those found by Buesseler et al. (1995) and Buesseler et al. (2009), which ranged from <0.5 to >4 μmol dpm^{-1} and 3.6 to 7.5 μmol dpm^{-1} for small and large particles, respectively. Sediment trap PC/Th ratios previously reported at Station ALOHA range from 3.9-14.9 μmol dpm^{-1} at 150 m (Benitez-Nelson et al., 2001; Buesseler et al., 2009), and from 5-8°N x 140°W are reported as ~2 - ~4 μmol dpm^{-1} (Murray et al., 1996), higher than those measured in this study (0.6-1.8 μmol dpm^{-1}) (Figure 3).

Profiles of PHg/Th ratios at Stations 5 and 6 show peaks at 25 and 125 m, which occur above and below peaks in POC/Th ratios. These differences suggest that dissimilar processes influence PHg formation and remineralization compared to PC formation and remineralization. The high PHg/Th peak at 25 m could be due in part to atmospheric deposition of Hg (Munson et al., 2015), and the peak at 125 m coincides with the oxycline at both stations, but the oxycline is much steeper at Station 5. This indicates that PHg concentration is likely influenced to some degree by the decline in oxygen. It has been hypothesized that low oxygen environments increase microbial reduction of Hg^{2+} to Hg^0, which is more soluble in seawater (Munson et al., 2015). While PHg/Th

ratio measurements in large particles are limited, they are the same or lower than those measured at the same depths in small particles, suggesting that, like PC, similar processes may be influencing both size fractions, such as aggregation of small particles into larger ones, or disaggregation of large particles.

Closer examination of PHg:C ratios, however, confirms that there are differences in particle cycling with increasing depth in water column. At Stations 5 and 6, the PHg/PC profiles are much more similar to the PHg/Th profile than the PC/Th profile (Figure 4.4), indicating that PHg is dominating changes in the ratio with depth. Munson et al. (2015) found that PHg:PC ratios ultimately increased with increasing depth, which seems to be the case at Station 6, but not Station 5, where oxygen concentrations are lower below 125 m. It is possible that some PHg is preferentially removed compared to PC in low oxygen waters, perhaps through methylation. At Station 5 in the small size fraction, PHg/PC ratios at 150 m were more than 2 times higher than those measured in the large size fraction. In contrast, at Station 6, small and large PHg:PC ratios at 150 m were the same within error. Compared to PHg:PC measurements made by Munson et al. (2015) at 150 m, ratios in this study were higher at all stations except station 1 (53 ± 4 fmol $umol^{-1}$), which fell in the middle of their range. Munson et al. (2015) did not find that remineralization of PC was well correlated with MeHg production, but rather varied with latitude. Coupled with our work, this supports the hypothesis that different microbial consortia are influencing PHg and PC concentrations and partially explain the differences in PHg:PC ratios with latitude(Bianchi et al., 2018; Blum et al., 2013).

4.4.4 PC and PN Fluxes

Latitudinal changes in primary productivity are not clearly reflected in PC, POC and PN fluxes measured in this study. The previously observed latitudinal changes in primary productivity (Hernes et al., 2001) do not appear to exert influence at 150 m at this longitude. Low C fluxes are not unprecedented in this area; Munson et al (2015) found that total mass flux at all depths at 17°N was below the detection limit of their sediment traps. Reported C fluxes using ^{234}Th- ^{238}U method in this region range from 400-4000 µmol m^{-2} day^{-1} (C. Benitez-Nelson et al., 2001; Black et al., 2018). Sediment trap PC, POC and PN fluxes here were lower by an order of magnitude than those found by Hernes et al. (2001), but given the Th derived fluxes, are not unreasonable. At Station 6 between 50 and 100 m, PC, POC and PN fluxes in the small size fraction are similar to those found by Black et al. (2018) and Benitez-Nelson et al. (2001) further north at Station ALOHA but are reduced to below detection below 150 m due to extensive remineralization. At Station 6, particle flux is higher at the surface and only attenuates below 75 m, which indicates that particle cycling in the upper 100 m is similar between the two stations, but differences may be caused by the depth of the fluorescence max, which is a proxy for primary production. Most physical/chemical (e.g., Oxygen, temperature, salinity, nutrient availability) parameters are the same between these two stations in the upper 75 m. A shift in foodweb composition and grazing activity moving away from the equator likely is the reason for higher particle flux at Station 6 compared to Station 5 (Cavan et al., 2017; Hernes et al., 2001; Lundry et al., 1997; Munson et al., 2015; Murray et al., 2005, 1996). Low POC fluxes in the large size fraction relative to large PC flux is again likely due to particle composition, which has been shown to be

increasingly inorganic C moving toward the center of the Pacific, possibly due to shift in phytoplankton community to smaller phytoplankton (Black et al., 2018; Lam et al., 2018). Overall, differences between stations in PC, POC and PN fluxes do not appear to be influenced by the shoaling of the oxygen minimum zone near 8^{o}N to 150 m. Differences between flux profiles at Stations 5 and 6 are minimal below 150m, and sediment trap PC fluxes are similar between Stations 5 and 6 as well. Current research suggests that POC flux is enhanced by lower dissolved oxygen as zooplankton do not assist with remineralization or particle repackaging in waters with low oxygen (Cavan et al., 2017), which is not the case here. Rather, remineralization and low particle fluxes mask any potential differences in PC flux associated with decreased oxygen concentration.

4.4.5 PHg Fluxes

Quantifying PHg sinking fluxes is a crucial part of understanding Hg cycling and the depths at which Hg may be introduced into the food web (Munson et al., 2015). This study provides some of the first measurements of sinking PHg fluxes in the equatorial Pacific using *in-situ* pumps and how those fluxes change with water depth and dissolved oxygen availability. Previous work made use of sediment traps to measure fluxes and used pumps to collect particle samples, but not to calculate fluxes (Lamborg et al., 2016; Munson et al., 2015; Strode et al., 2010). Based on PHg:PC ratios, PHg fluxes were influenced by a combination of particle scavenging and biological processes that were distinct from those that influence PC fluxes. It appears that dissolved oxygen concentrations may play a bigger role in PHg flux than in PC flux. PHg fluxes are the same between Stations 5 and 6 above 100 m, where dissolved oxygen concentrations are

also similar (160-190 µmol kg^{-1}). However, by 125 m, dissolved oxygen is 140 µmol kg^{-1} at Station 6 compared to 20 µmol kg^{-1} at Station 5. Small PHg fluxes at 125 m at Station 6 are 7 times higher than at station 5. This is in agreement with previous work that suggests low oxygen is associated with increased Hg methylation (Blum et al., 2013; Munson et al., 2015). PHg fluxes are higher in the more oxygenated waters, and in water with less oxygen PHg flux was lower, perhaps because PHg is being removed through methylation. Higher particle concentrations overall increase PHg concentrations by providing a substrate onto which PHg can adsorb (Munson et al. 2015). Particle fluxes are slightly higher at Station 6 which may contribute to higher PHg fluxes. Mercury isotopes ratios, dissolved Hg and MeHg data would be necessary to confirm this hypothesis. Although the data is limited, PHg fluxes of large particles at 150 m are similar to small PHg fluxes at each station, indicating that large and small PHg particles are undergoing the same particle cycling processes at this depth. Below 200 m, fluxes for all elements are below detection, indicating that remineralization processes dominate at all stations, regardless of primary productivity or oxygen concentration below 200 m.

4.4.5. Conclusion

^{238}U-^{234}Th was used to measure PC, PN, and PHg fluxes throughout the water column across a latitudinal gradient from 5ºN -17ºN along 155ºW, following a shoaling oxygen minimum zone. Particle fluxes of PC, POC and PN were generally low at all stations, peaking at Stations 5 and 6 coincident with an increase in fluorescence and decreasing rapidly with increasing depth, such that at 150 m, fluxes were often below detection. This made elucidation of spatial changes difficult to detect. While there were differences in PC, POC and PN fluxes in the upper 100 m between stations 5 and 6, PHg flux in the

upper 100 m was the same between stations, indicating that particle cycling for PHg is indeed different from PC, POC and PN. Primary production directly creates PC, whereas the only contribution to PHg primary production makes is providing substrates onto which Hg^0 is oxidized to Hg^{2+} (Munson et al., 2015). Hg particle cycling in the surface waters will remain different from C or N cycling due to processes that only affect Hg, such as photodegradation or methylation/demethylation (Fitzgerald and Lamborg, 2003; C. H. Lamborg et al., 2014; Munson et al., 2015). These results confirm that dissolved oxygen concentrations play an important role in subsurface Hg cycling and are critical for understanding Hg bioaccumulation in marine systems.

4.6 Acknowledgments

We would like to thank the captain and crew of the R/V Kilo Moana, Justin Miyano, Meryssa Piper, Kalina Grabb and Marc Humphries for their assistance with pump deployment and sample collection. This work was funded by National Science Foundation grant OCE 1433313, and BU was supported by a University of South Carolina Presidential Fellowship

4.7 References

Alonso-Gonzalez, I.J., Aristegui, J., Lee, C., Sanchez-Vidal, A., Calafat, A., Fabres, J., Sangra, P., Masque, P., Hernandez-Guerra, A., Benitez-Barrios, V., 2010. Role of slowly settling particles in the ocean carbon cycle. Geophys. Res. Lett. doi:10.1029/2010GL043827

Benitez-Nelson, C., Buesseler, K.O., Karl, D.M., Andrews, J., 2001. A time-series study of particulate matter export in the North Pacific Subtropical Gyre based on 234 Th : 238 U disequilibrium. Deep Sea Res. I 48, 2595–2611.

Benitez-Nelson, C.R., Buesseler, K.O., van der Loeff, M.R., Andrews, J., Ball, L., Crossin, G., Charette, M.A., 2001. Testing a new small-volume technique for determining 234 Th in seawater. J. Radioanal. Nucl. Chem. 248, 795–799.

Bianchi, D., Weber, T.S., Kiko, R., Deutsch, C., 2018. Global niche of marine anaerobic metabolisms expanded by particle microenvironments. Nat. Geosci. 11, 263–268. doi:10.1038/s41561-018-0081-0

Biswas, A., Blum, J.D., Bergquist, B.A., Keeler, G.J., Xie, Z., 2008. Natural mercury isotope variation in coal deposits and organic soils. Environ. Sci. Technol. 42, 8303–8309. doi:10.1021/es801444b

Black, E.E., Buesseler, K.O., Pike, S.M., Lam, P.J., 2018. 234Th as a tracer of particulate export and remineralization in the southeastern tropical Pacific. Mar. Chem. 201, 35–50. doi:10.1016/j.marchem.2017.06.009

Blum, J.D., Popp, B.N., Drazen, J.C., Anela Choy, C., Johnson, M.W., 2013.

Methylmercury production below the mixed layer in the North Pacific Ocean. Nat. Geosci. 6, 879–884. doi:10.1038/ngeo1918

Buesseler, K., Andrews, J.A., Hartman, M.C., Belastock, R., Chai, F., 1995. Regional estimates of the export flux of particulate organic carbon derived from thorium-234 during the JGOFS EqPac program. Deep Sea Res. II 42, 777–804.

Buesseler, K.O., Benitez-nelson, C.R., Moran, S.B., Burd, A., Charette, M., Cochran, J.K., Coppola, L., Fisher, N.S., Fowler, S.W., Gardner, W.D., Guo, L.D., Gustafsson, O., Lamborg, C., Masque, P., Miquel, J.C., Passow, U., Santschi, P.H., Savoye, N., Stewart, G., Trull, T., 2006. An assessment of particulate organic carbon to thorium-234 ratios in the ocean and their impact on the application of 234 Th as a POC flux proxy. Mar. Chem. 100, 213–233. doi:10.1016/j.marchem.2005.10.013

Buesseler, K.O., Pike, S., Maiti, K., Lamborg, C.H., Siegel, D.A., Trull, T.W., 2009. Thorium-234 as a tracer of spatial , temporal and vertical variability in particle flux in the North Pacific. Deep. Res. Part I 56, 1143–1167. doi:10.1016/j.dsr.2009.04.001

Buesseler, K.O., Trull, T.W., Steinberg, D.K., Silver, M.W., Siegel, D.A., Saitoh, S., Lamborg, C.H., Lam, P.J., Karl, D.M., Jiao, N.Z., Honda, M.C., Elskens, M., Dehairs, F., Brown, S.L., Boyd, P.W., Bishop, J.K.B., Bidigare, R.R., 2008. VERTIGO (VERtical Transport In the Global Ocean): A study of particle sources and flux attenuation in the North Pacific. Deep. Res. II 55, 1522–1539. doi:10.1016/j.dsr2.2008.04.024

Cavan, E.L., Trimmer, M., Shelley, F., Sanders, R., 2017. Remineralization of particulate organic carbon in an ocean oxygen minimum zone. Nat. Commun. 8, 1–9.

doi:10.1038/ncomms14847

Choy, C.A., Popp, B.N., Hannides, C.C.S., Drazen, J.C., 2015. Trophic structure and food resources of epipelagic and mesopelagic fishes in the north pacific subtropical Gyre ecosystem inferred from nitrogen isotopic compositions. Limnol. Oceanogr. doi:10.1002/lno.10085

Choy, C.A., Popp, B.N., Kaneko, J.J., Drazen, J.C., 2009. The influence of depth on mercury levels in pelagic fishes and their prey. Proc. Natl. Acad. Sci. U. S. A. 106, 13865–13869. doi:10.1073/pnas.0900711106

Cossa, D., Harmelin-Vivien, M., Mellon-Duval, C., Loizeau, V., Averty, B., Crochet, S., Chou, L., Cadiou, J.-F., 2012. Influences of bioavailability, trophic position, and growth on methylmercury in hakes (Merluccius merluccius) from Northwestern Mediterranean and Northeastern Atlantic. Environ. Sci. Technol. 46, 4885–93. doi:10.1021/es204269w

Dunne, J.P., Murray, J.W., Rodier, M., Hansell, D.A., 2000. Export flux in the western and central equatorial Pacific: zonal and temporal variability. Deep Sea Res. I 47, 901–936.

Durkin, C.A., Estapa, M.L., Buesseler, K.O., 2015. Observations of carbon export by small sinking particles in the upper mesopelagic. Mar. Chem. doi:10.1016/j.marchem.2015.02.011

Fitzgerald, W.F., Lamborg, C.H., 2003. Geochemistry of Mercury in the Environment. Treatise on Geochemistry 9.

Hammerschmidt, C.R., Bowman, K.L., 2012. Vertical methylmercury distribution in the subtropical North Pacific Ocean. Mar. Chem. 132–133, 77–82. doi:10.1016/j.marchem.2012.02.005

Hannides, C.C.S., Popp, B.N., Close, H.G., Benitez-nelson, C.R., Ka'apu-Lyons, C.A., Gloeckler, K., Wallsgrove, N., Umhau, B., Palmer, E., Drazen, J.C., n.d. Seasonal dynamics of midwater zooplankton and relation to particle cycling in the North Pacific Subtropical Gyre . Prog. Oceanogr. 1–101.

Haskell, W.Z., Berelson, W.M., Hammond, D.E., Capone, D.G., 2013. Particle sinking dynamics and POC fluxes in the Eastern Tropical South Pacific based on 234Th budgets and sediment trap deployments. Deep. Res. Part I Oceanogr. Res. Pap. 81, 1–13. doi:10.1016/j.dsr.2013.07.001

Heimbürger, L.E., Cossa, D., Marty, J.C., Migon, C., Averty, B., Dufour, A., Ras, J., 2010. Methyl mercury distributions in relation to the presence of nano- and picophytoplankton in an oceanic water column (Ligurian Sea, North-western Mediterranean). Geochim. Cosmochim. Acta 74, 5549–5559. doi:10.1016/j.gca.2010.06.036

Hernes, P.J., Peterson, M.L., Murray, J.W., Wakeham, S.G., Lee, C., Hedges, J.I., 2001. Particulate carbon and nitrogen fluxes and compositions in the central equatorial Pacific. Deep Sea Res. Part I Oceanogr. Res. Pap. 48, 1999–2023. doi:10.1016/S0967-0637(00)00115-1

Kadko, D., Feely, R., Massoth, G., 1994. Scavenging of 234Th and phosphorus removal from the hydrothermal effluent plume over the north Cleft segment of the Juan de

Fuca Ridge. J. Geophys. Res. doi:10.1029/93JB02952

Kennedy, P., Kennedy, H., Papadimitriou, S., 2005. The effect of acidification on the determination of organic carbon , total nitrogen and their stable isotopic composition in algae and marine sediment. Rapid Commun. Mass Spectrom. 19, 1063–1068. doi:10.1002/rcm.1889

Knauer, G.A., Martin, J.H., Bruland, K.W., 1979. Fluxes of particulate carbon, nitrogen, and phosphorus in the upper water column of the northeast Pacific. Deep Sea Res. Part A, Oceanogr. Res. Pap. 26, 97–108. doi:10.1016/0198-0149(79)90089-X

Lam, P.J., Lee, J.M., Heller, M.I., Mehic, S., Xiang, Y., Bates, N.R., 2018. Size-fractionated distributions of suspended particle concentration and major phase composition from the U.S. GEOTRACES Eastern Pacific Zonal Transect (GP16). Mar. Chem. 201, 90–107. doi:10.1016/j.marchem.2017.08.013

Lam, P.J., Ohnemus, D.C., Auro, M.E., 2015. Size-fractionated major particle composition and concentrations from the US GEOTRACES North Atlantic Zonal Transect. Deep. Res. Part II Top. Stud. Oceanogr. 116, 303–320. doi:10.1016/j.dsr2.2014.11.020

Lamborg, C., Bowman, K., Hammerschmidt, C., Gilmour, C., Munson, K., Selin, N., Tseng, C.-M., 2014. Mercury in the Anthropocene Ocean. Oceanography 27, 76–87. doi:10.5670/oceanog.2014.11

Lamborg, C.H., Hammerschmidt, C.R., Bowman, K.L., 2016. An examination of the role of particles in oceanic mercury cycling. Philos. Trans. R. Soc. A 374.

Lamborg, C.H., Hammerschmidt, C.R., Bowman, K.L., Swarr, G.J., Munson, K.M., Ohnemus, D.C., Lam, P.J., Heimbürger, L.-E., Rijkenberg, M.J. a., Saito, M. a., 2014. A global ocean inventory of anthropogenic mercury based on water column measurements. Nature 512, 65–68. doi:10.1038/nature13563

Lundry, M.R., Barber, R.T., Bidare, R.R., Chai, F., Coale, K.H., Dam, H.G., Lewis, M.R., Lindley, S.T., McCarthy, J.J., Roman, M.R., Stoecker, D.K., Verity, P.G., White, J.R., 1997. Iron and grazing constraints on primary production in the central equatorial Pacific: An EqPac synthesis. Limnol. Oceanogr. 42, 405–418. doi:10.4319/lo.1997.42.3.0405

Maiti, K., Benitez-nelson, C.R., Rii, Y., Bidigare, R., 2008. Deep-Sea Research II The influence of a mature cyclonic eddy on particle export in the lee of Hawaii. Deep Sea Res. II 55, 1445–1460. doi:10.1016/j.dsr2.2008.02.008

Munson, K.M., Lamborg, C., Swarr, G.J., Saito, M.A., 2015. Mercury species concentrations and fluxes in the Central Tropical Pacific Ocean. Global Biogeochem. Cycles 29, 656–676. doi:10.1002/2015GB005120.Received

Murray, J.W., Paul, B., Dunne, J.P., Chapin, T., 2005. 234Th,210Pb,210Po and stable Pb in the central equatorial Pacific: Tracers for particle cycling. Deep. Res. Part I Oceanogr. Res. Pap. 52, 2109–2139. doi:10.1016/j.dsr.2005.06.016

Murray, J.W., Young, J., Newton, J., Dunne, J., Chapin, T., Paul, B., Mccarthys, J.J., 1996. Export flux of particulate organic carbon from the central equatorial Pacific determined using a combined drifting trap-234Th approach. Deep. Res. II 43, 1095–132. doi:10.1016/0967-0645(96)00036-7

Owens, S.A., Buesseler, K.O., Sims, K.W.W., 2011. Re-evaluating the 238 U-salinity relationship in seawater : Implications for the U – 234 Th disequilibrium method. Mar. Chem. 127, 31–39. doi:10.1016/j.marchem.2011.07.005

Owens, S.A., Pike, S., Buesseler, K.O., 2015. Thorium-234 as a tracer of particle dynamics and upper ocean export in the Atlantic Ocean. Deep Sea Res. Part II Top. Stud. Oceanogr. 116, 42–59. doi:10.1016/j.dsr2.2014.11.010

Pike, S.M., Buesseler, K.O., Andrews, J., Savoye, N., 2005. Quantification of 234 Th recovery in small volume sea water samples by inductively coupled plasma-mass spectrometry. J. Radioanal. Nucl. Chem. 263, 355–360.

Puigcorbé, V., Benitez-nelson, C.R., Masqué, P., Verdeny, E., White, A.E., Popp, B.N., Prahl, F.G., Lam, P.J., 2015. Small phytoplankton drive high summertime carbon and nutrient export in the Gulf of California and Eastern Tropical North Pacific. Global Biogeochem. Cycles 1309–1332. doi:10.1002/2015GB005134.Received

Richardson, T.L., Jackson, G.A., 2007. Small Phytoplankton and Carbon Export from the Surface Ocean. Science (80-.). 838–840. doi:10.1126/science.1133471

Selin, N.E., 2009. Global Biogeochemical Cycling of Mercury: A Review. Annu. Rev. Environ. Resour. 34, 43–63. doi:10.1146/annurev.environ.051308.084314

Siegel, D.A., Buesseler, K.O., Behrenfeld, M.J., Benitez-Nelson, C.R., Boss, E., Brzezinski, M.A., Burd, A., Carlson, C.A., D'Asaro, E.A., Doney, S.C., Perry, M.J., Stanley, R.H.R., Steinberg, D.K., 2016. Prediction of the Export and Fate of Global Ocean Net Primary Production: The EXPORTS Science Plan. Front. Mar. Sci. 3, 1–

10. doi:10.3389/fmars.2016.00022

Siegel, D.A., Buesseler, K.O., Doney, S.C., Sailley, S.F., Behrenfeld, M.J., Boyd, P.W., 2014. Global assessment of ocean carbon export by combining satellite observations and food-web models. Global Biogeochem. Cycles 28, 181–196. doi:10.1002/2013GB004743.Received

Strode, S., Jaeglé, L., Emerson, S., 2010. Vertical transport of anthropogenic mercury in the ocean. Global Biogeochem. Cycles 24, 1–10. doi:10.1029/2009GB003728

Weinstein, S.E., Moran, S.B., 2005. Vertical flux of particulate Al, Fe, Pb, and Ba from the upper ocean estimated from234Th/238U disequilibria. Deep. Res. Part I Oceanogr. Res. Pap. doi:10.1016/j.dsr.2005.03.008

Table 4.1 1-53 µm particle concentrations. Abbreviations: PTh-particulate thorium; PC-particulate carbon; POC-particulate organic carbon; PN-particulate nitrogen; PHg-particulate mercury.

Lat ºN	Station	Depth (m)	PTh (dpm L^{-1})	± Error	PC (nmol L^{-1})	± Error	POC (nmol L^{-1})	± Error	PN (nmol L^{-1})	± Error	PHg (fmol L^{-1})	± Error
17	1	150	0.13	0.02	510	25	487	24	72	4	27	1.4
15	2	150	0.15	0.02	530	26	418	21	67	3	-	-
12	3	150	0.17	0.02	413	21	404	20	64	3	-	-
10	4	150	0.13	0.02	294	15	275	14	45	2	-	-
8	5	5	0.48	0.06	580	29	545	27	69	3	88	4
8	5	25	0.36	0.04	720	36	722	36	84	4	84	4
8	5	50	0.31	0.04	2099	105	1837	92	294	15	46	2
8	5	75	0.35	0.03	607	30	571	29	93	5	-	-
8	5	100	0.25	0.02	-	-	-	-	-	-	43	2
8	5	125	0.19	0.02	331	17	296	15	50	3	38	2
8	5	150	0.21	0.02	308	15	126	6	42	2	24	1

8	5	200	0.20	0.02	271	14	193	10	31	2	-	-
8	5	250	0.19	0.01	186	9	141	7	21	1	26	1
8	5	400	0.15	0.01	234	12	197	10	26	1	24	1
5	6	5	0.72	0.06	1032	52	997	50	120	6	22	1
5	6	25	0.45	0.08	1037	52	790	39	128	6	66	3
5	6	50	0.24	0.01	914	46	889	44	102	5	36	2
5	6	75	0.11	0.01	1838	92	1237	62	267	13	-	-
5	6	100	0.23	0.02	834	42	724	36	125	6	25	1
5	6	125	0.21	0.02	576	29	294	15	70	4	64	3
5	6	150	0.21	0.03	380	19	281	14	50	3	33	2
5	6	200	0.23	0.03	321	16	164	8	34	2	-	-
5	6	250	0.18	0.02	291	15	173	9	29	1	23	1
5	6	300	0.18	0.02	247	12	197	10	26	1	30	2
5	6	400	0.13	0.01	208	10	182	9	22	1	28	1

Table 4.2 >53 µm particle concentrations. Abbreviations: PTh-particulate thorium; PC-particulate carbon; POC-particulate organic carbon; PN-particulate nitrogen; PHg-particulate mercury.

Lat ºN	Station	Depth (m)	PTh (dpm L^{-1})	± Error	PC (nmol L^{-1})	± Error	POC (nmol L^{-1})	± Error	PN (nmol L^{-1})	± Error	PHg (fmol L^{-1})	± Error
17	1	150	0.02	0.002	44	2	4	0.2	5	0.3	-	-
15	2	150	0.02	0.002	41	9	4	0.3	5	1	-	-
12	3	150	0.02	0.002	58	28	4	1.5	6	3	-	-
10	4	150	0.02	0.003	55	23	6	0.1	8	2	-	-
8	5	5	0.02	0.00	59	3	6	0.3	8	0.04	-	-
8	5	25	0.24	0.01	53	3	5	0.2	8	0.61	-	-
8	5	50	0.07	0.01	70	3	7	1.1	10	3.25	-	-
8	5	75	0.08	0.01	74	4	9	1.2	11	1.88	-	-
8	5	100	0.06	0.01	29	1	8	0.4	8	6.47	-	-
8	5	125	0.05	0.01	50	2	8	0.4	8	0.18	-	-
8	5	150	0.03	0.01	50	35	3	0.5	5	3.94	2	0

8	5	200	0.02	0.00	33	2	3	0.1	3	0.16	-	-
8	5	250	0.02	0.00	28	1	3	0.1	2	0.12	-	-
8	5	400	0.02	0.00	23	1	2	0.1	2	0.04	-	-
5	6	5	0.01	0.00	47	2	4	0.2	4	0.18	-	-
5	6	25	0.01	0.00	29	1	3	0.2	4	0.38	-	-
5	6	50	0.06	0.01	60	3	6	0.3	7	0.60	-	-
5	6	75	0.08	0.04	86	4	10	0.5	15	2.21	-	-
5	6	100	0.02	0.00	65	3	4	0.2	7	1.81	-	-
5	6	125	0.09	0.03	166	8	17	0.8	24	1.88	-	-
5	6	150	0.04	0.00	38	2	4	0.2	5	0.68	4	0
5	6	200	0.02	0.00	35	2	2	0.1	3	0.93	-	-
5	6	250	0.15	0.01	24	1	2	0.1	2	0.02	-	-
5	6	300	0.02	0.00	21	1	2	0.1	2	0.00	-	-
5	6	400	0.01	0.00	19	1	2	0.1	2	0.02	2	0

Table 4.3 1-53 µm element to thorium ratios. Abbreviations: PTh-particulate thorium; PC-particulate carbon; POC-particulate organic carbon; PN-particulate nitrogen; PHg-particulate mercury.

Lat ºN	Station	Depth (m)	PC/Th (µmol dpm^{-1})	± Error	POC/Th (µmol dpm^{-1})	± Error	PN/Th (µmol dpm^{-1})	± Error	PHg/Th (fmol dpm^{-1})	± Error
17	1	150	3.8	0.5	3.6	0.5	0.5	0.07	201	27
15	2	150	3.6	0.5	2.8	0.4	0.5	0.07	-	-
12	3	150	2.4	0.4	2.4	0.4	0.4	0.06	-	-
10	4	150	2.2	0.3	2.1	0.3	0.3	0.05	207	29
8	5	5	1.2	0.2	1.1	0.2	0.1	0.02	185	25
8	5	25	2.0	0.2	2.0	0.2	0.2	0.03	232	26
8	5	50	6.7	0.9	5.8	0.8	0.9	0.13	147	20
8	5	75	1.7	0.2	1.6	0.1	0.3	0.02	-	-
8	5	100	-	-	-	-	-	-	171	17
8	5	125	1.8	0.2	1.6	0.2	0.3	0.03	203	25
8	5	150	1.4	0.2	0.6	0.1	0.2	0.02	110	13
8	5	200	1.3	0.2	0.9	0.1	0.2	0.02	-	-

8	5	250	1.0	0.1	0.7	0.1	0.1	0.01	137	13
8	5	400	1.6	0.1	1.3	0.1	0.2	0.02	157	15
5	6	5	1.4	0.1	1.4	0.1	0.2	0.02	30	3
5	6	25	2.3	0.4	1.8	0.3	0.3	0.05	147	26
5	6	50	3.8	0.3	3.7	0.3	0.4	0.03	149	11
5	6	75	16.0	1.8	10.8	1.2	2.3	0.27	-	-
5	6	100	3.7	0.4	3.2	0.3	0.5	0.06	108	12
5	6	125	2.8	0.3	1.4	0.2	0.3	0.04	311	38
5	6	150	1.9	0.2	1.4	0.2	0.2	0.03	162	22
5	6	200	1.4	0.2	0.7	0.1	0.2	0.02	-	-
5	6	250	1.6	0.2	1.0	0.1	0.2	0.02	124	14
5	6	300	1.4	0.2	1.1	0.1	0.1	0.02	165	19
5	6	400	1.6	0.2	1.4	0.2	0.2	0.02	217	26

Table 4.4 >53 µm element to thorium ratios. Abbreviations: PC-particulate carbon; POC-particulate organic carbon; PN-particulate nitrogen; PHg-particulate mercury.

Lat ºN	Station	Depth (m)	PC/Th (µmol dpm^{-1})	± Error	POC/Th (µmol dpm^{-1})	± Error	PN/Th (µmol dpm^{-1})	± Error	PHg/Th (fmol dpm^{-1})	± Error
17	1	150	2.8	0.3	0.2	0.03	0.3	0.04	-	-
15	2	150	2.3	0.5	0.2	0.02	0.3	0.06	-	-
12	3	150	2.6	1.3	0.2	0.07	0.3	0.14	-	-
10	4	150	2.2	1.0	0.2	0.03	0.3	0.09	-	-
5	5	5	3.2	0.3	0.3	0.03	0.4	0.03	-	-
8	5	25	0.2	0.0	0.0	0.00	0.0	0.00	-	-
8	5	50	1.0	0.2	0.1	0.02	0.2	0.06	-	-
8	5	75	0.9	0.1	0.1	0.02	0.1	0.03	-	-
8	5	100	0.4	0.1	0.1	0.03	0.1	0.10	-	-
8	5	125	1.1	0.2	0.2	0.04	0.2	0.04	-	-
8	5	150	1.4	1.1	0.1	0.02	0.2	0.12	45	10

8	5	200	1.5	0.1	0.1	0.01	0.1	0.01	-	-
8	5	250	1.3	0.1	0.1	0.01	0.1	0.01	-	-
8	5	400	1.5	0.1	0.1	0.01	0.1	0.01	-	-
5	6	25	2.4	0.2	0.3	0.03	0.3	0.04	-	-
5	6	50	1.1	0.2	0.1	0.02	0.1	0.03	-	-
5	6	75	1.0	0.5	0.1	0.06	0.2	0.09	-	-
5	6	100	3.1	0.3	0.2	0.02	0.4	0.09	-	-
5	6	125	1.8	0.7	0.2	0.07	0.3	0.10	-	-
5	6	150	1.0	0.1	0.1	0.01	0.1	0.02	96	13
5	6	200	1.7	0.3	0.1	0.01	0.1	0.05	-	-
5	6	250	0.2	0.0	0.0	0.00	0.0	0.00	-	-
5	6	300	1.3	0.2	0.1	0.01	0.1	0.01	-	-
5	6	400	1.7	0.2	0.1	0.01	0.1	0.01	152	13

Table 4.5 1-53 µm particle fluxes from in-situ pumps. Abbreviations: PTh-particulate thorium; PC-particulate carbon; POC-particulate organic carbon; PN-particulate nitrogen; PHg-particulate mercury. Bold indicates below detection (<224 dpm m^{-2} day^{-1}) or remineralization.

Lat ºN	**Station**	**Depth (m)**	**PTh (dpm m^{-2} d^{-1})**	**± Error**	**PC (µmol m^{-2} d^{-1})**	**± Error**	**POC (µmol m^{-2} d^{-1})**	**± Error**	**PN (µmol m^{-2} d^{-1})**	**± Error**	**PHg (fmol m^{-2} d^{-1})**	**± Error**
17	1	150	**0**	**0**	**0**	**0**	**0**	**0**	**0**	**0**	**0**	**0**
15	2	150	**0**	**0**	**0**	**0**	**0**	**0**	**0**	**0**	-	-
12	3	150	515	355	1246	881	1220	863	193	137	-	-
10	4	150	**0**	**0**	**0**	**0**	**0**	**0**	**0**	**0**	**0**	**0**
5	6	5	**15**	**21**	19	25	18	24	2	3	3	4
8	5	25	**119**	**81**	236	163	237	163	28	19	28	19
8	5	50	273	99	1823	709	1595	620	255	99	40	16
8	5	75	308	102	537	184	505	173	82	28	-	-
8	5	100	273	102	-	-	-	-	-	-	47	18
8	5	125	**92**	**157**	165	281	147	251	25	43	19	32

8	5	150	**0**	**0**	**0**	**0**	**0**	**0**	**0**	**0**	**0**	**0**
8	5	200	**0**	**0**	**0**	**0**	**0**	**0**	**0**	**0**	0	0
8	5	250	**0**	**0**	**0**	**0**	**0**	**0**	**0**	**0**	**0**	**0**
8	5	300	**0**	**0**	-	-	-	-	-	-	-	-
8	5	400	**0**	**0**	**0**	**0**	**0**	**0**	**0**	**0**	**0**	**0**
5	5	5	**92**	**162**	131	232	127	224	15	27	3	5
5	6	25	269	162	623	392	474	299	77	49	39	25
5	6	50	258	162	979	621	952	604	110	70	38	24
5	6	75	337	178	5392	2924	3629	1968	783	425	-	-
5	6	100	457	181	1674	690	1452	598	250	103	49	20
5	6	125	450	185	1252	537	639	274	152	65	140	60
5	6	150	375	188	694	360	513	266	92	48	61	32
5	6	200	278	191	392	273	201	140	42	29	-	-
5	6	250	**12**	**254**	20	406	12	241	2	40	2	32
5	6	300	**0**	**0**	**0**	**0**	**0**	**0**	**0**	**0**	**0**	**0**
5	6	400	**0**	**0**	**0**	**0**	**0**	**0**	**0**	**0**	**0**	**0**

Table 4.6 >53 µm particle fluxes from in-situ pumps. Abbreviations: PC-particulate carbon; POC-particulate organic carbon; PN-particulate nitrogen; PHg-particulate mercury. Bold numbers indicate remineralization.

Lat **ºN**	**Station**	**Depth (m)**	**PC (µmol m^{-2} d^{-1})**	**± Error**	**POC (µmol m^{-2} d^{-1})**	**± Error**	**PN (µmol m^{-2} d^{-1})**	**± Error**	**PHg (fmol m^{-2} d^{-1})**	**± Error**
17	1	150	**0**	**0**	**0**	**0**	**0**	**0**	-	-
15	2	150	**0**	**0**	**0**	**0**	**0**	**0**	-	-
12	3	150	1340	1141	99	77	148	125	-	-
10	4	150	**0**	**0**	**0**	**0**	**0**	**0**	-	-
8	5	25	27	18	2	2	4	3	-	-
8	5	50	280	115	27	12	41	21	-	-
8	5	75	274	99	32	12	43	17	-	-
8	5	100	121	51	35	15	33	31	-	-
8	5	125	100	171	17	29	16	27	-	-
8	5	150	**0**	**0**	**0**	**0**	**0**	**0**	**0**	**0**
8	5	200	**0**	**0**	**0**	**0**	**0**	**0**	-	-
8	5	250	**0**	**0**	**0**	**0**	**0**	**0**	-	-

8	5	400	**0**	**0**	**0**	**0**	**0**	**0**	-	-
5	5	5	50	68	5	6	7	9	-	-
5	6	5	745	1318	59	105	57	101	-	-
5	6	25	656	401	76	47	87	54	-	-
5	6	50	277	185	26	18	33	22	-	-
5	6	75	354	250	43	31	61	44	-	-
5	6	100	1419	579	92	38	160	76	-	-
5	6	125	806	447	82	46	115	64	-	-
5	6	150	365	189	39	20	44	24	35.9	18.63
5	6	200	461	326	23	17	38	29	-	-
5	6	250	2	40	0	4	0	4	-	-
5	6	300	**0**	**0**	**0**	**0**	**0**	**0**	-	-
5	6	400	**0**	**0**	**0**	**0**	**0**	**0**	**0**	**0**

Table 4.7 150 m Sediment trap element to thorium ratios and particle fluxes. PTh-particulate thorium; PC-particulate carbon; POC-particulate organic carbon; PN-particulate nitrogen. Bold numbers indicate remineralization.

Sediment Trap	**Station**			**PC/Th µmol dpm^{-1}**	**± Error**	**POC/Th µmol dpm^{-1}**	**± Error**	**PN/Th µmol dpm^{-1}**	**± Error**
	5	-	-	1.8	0.2	1.0	0.1	0.1	0.02
	6	-	-	0.6	0.1	0.6	0.1	0.3	0.05
		$P^{234}Th$ (dpm m^{-2} d^{-1})	**± Error**	**PC (µmol m^{-2} d^{-1})**	**± Error**	**POC (µmol m^{-2} d^{-1})**	**± Error**	**PN (µmol m^{-2} d^{-1})**	**± Error**
Direct	5	75	7	128	13	68	7	10	1
	6	118	15	71	7	65	6	33	3
Th-derived	5	-	-	**0**	**0**	**0**	**0**	**0**	**0**
	6	-	-	240	203	218	185	113	95

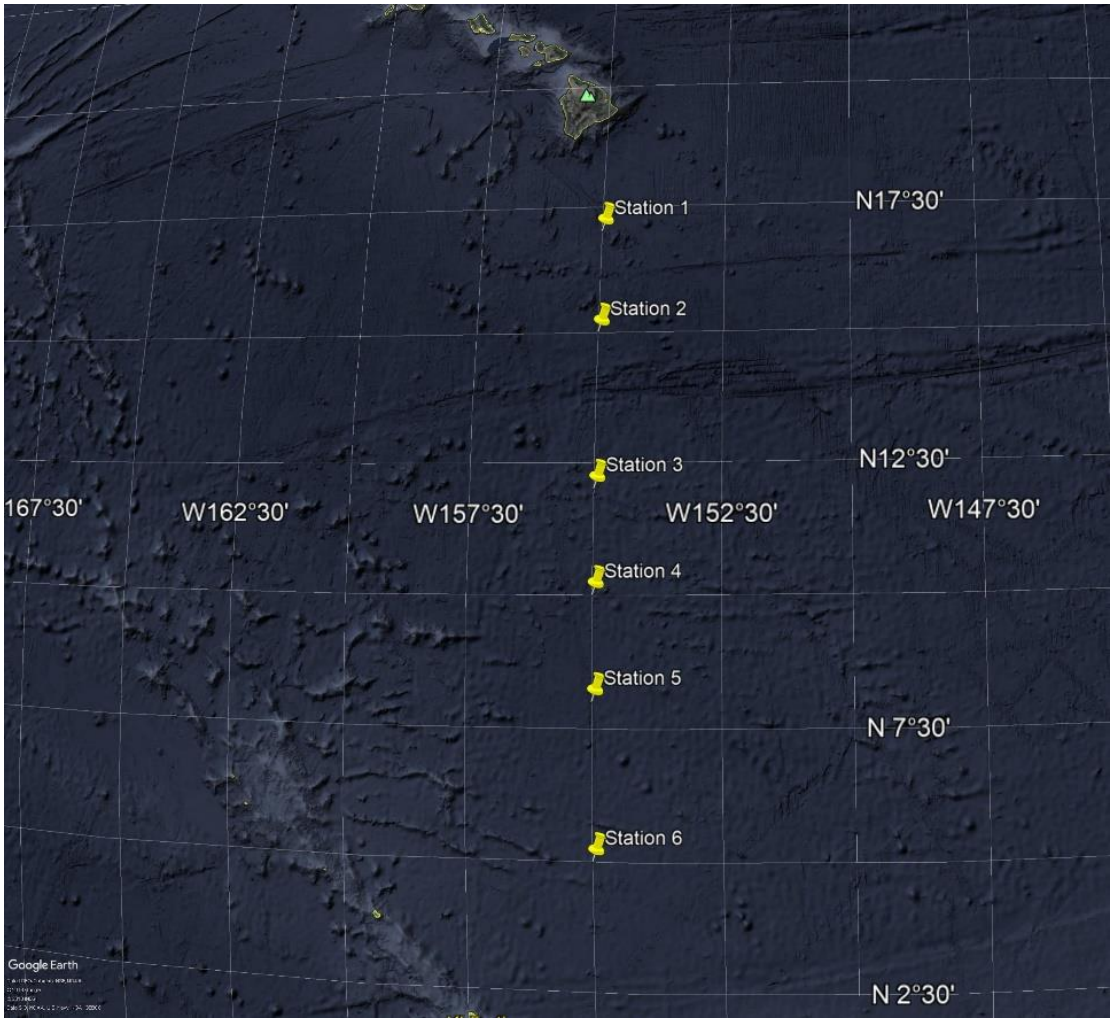

Figure 4.1 Map of Stations 1,2,3,4,5 and 6 in the central Pacific Ocean. Source: Google Earth

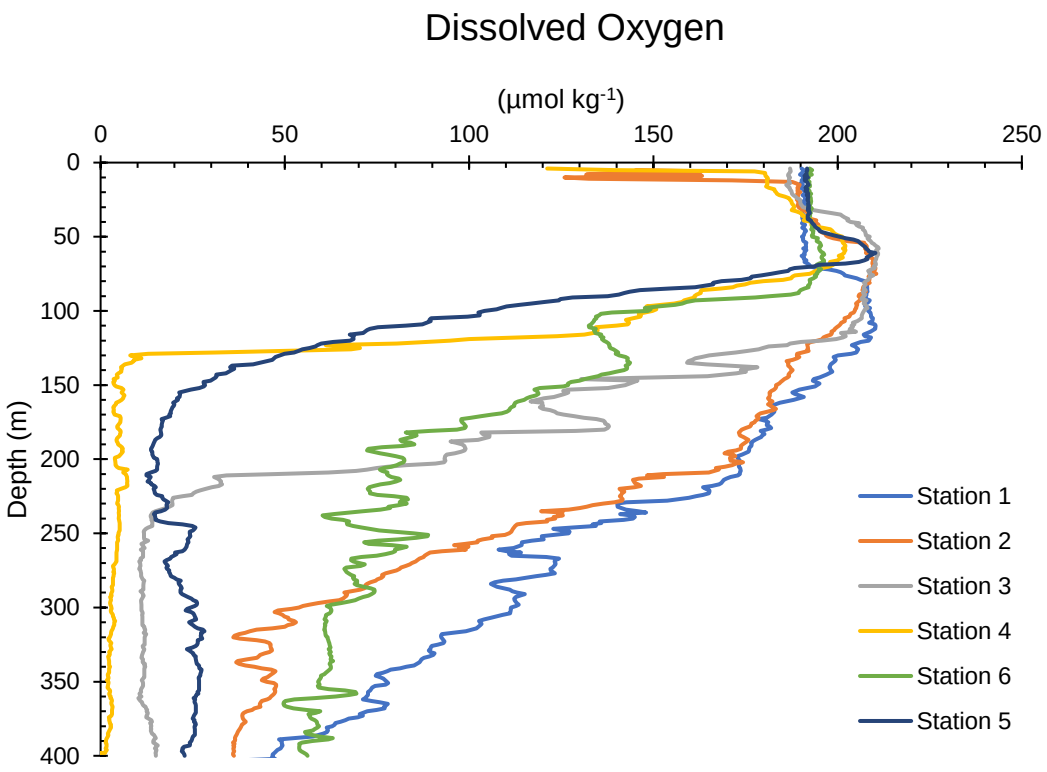

Figure 4.2 Dissolved oxygen profiles in the upper 400 m at stations 1-6.

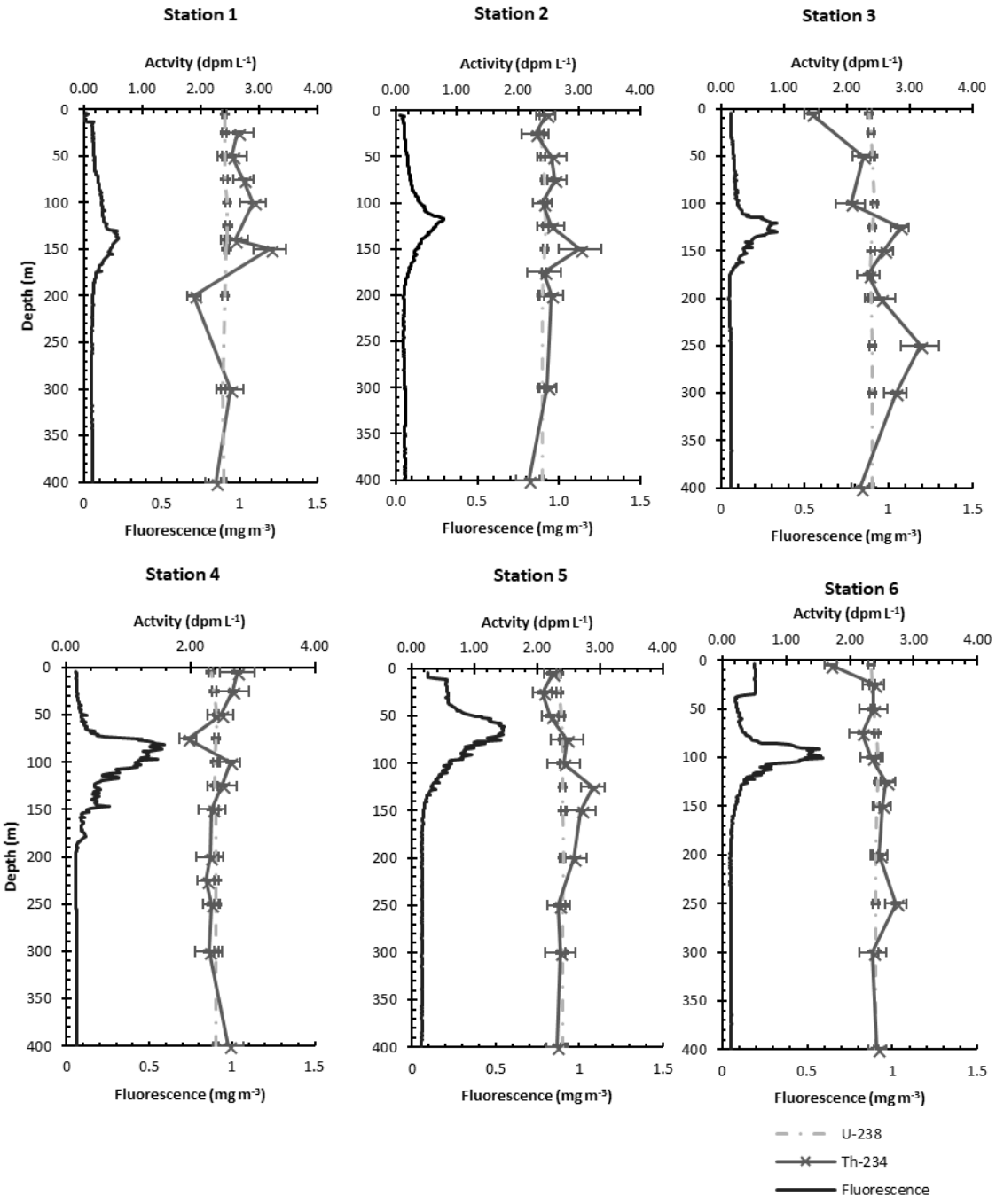

Figure 4.3 Plot of 234Th activity, 238U activity (upper axis), and fluorescence (lower axis) with depth at stations 1,2,3,4,5, and 6. Error bars indicate standard error.

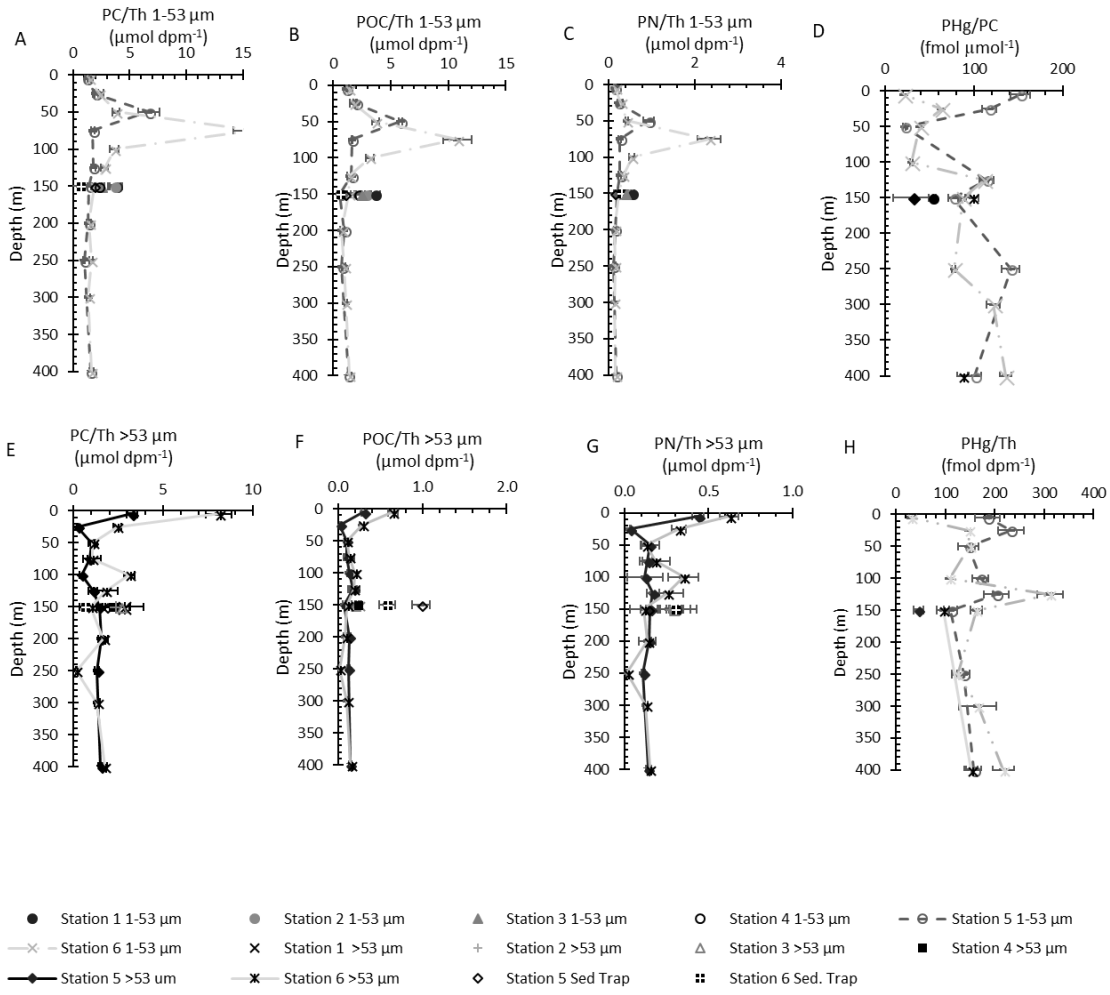

Figure 4.4 Vertical profiles of element ratios for small particle PC/Th (A), POC/Th (B) and PN/Th (C), PHg:PC(D), large particle PC/Th (E), POC/Th (F) and PN/Th (G),and all particulate and PHg/Th (H). Abbreviations: PC, particulate carbon; POC, particulate organic carbobn; PN, particulate nitrogen; Th, particulate thorium; PHg, particulate mercury

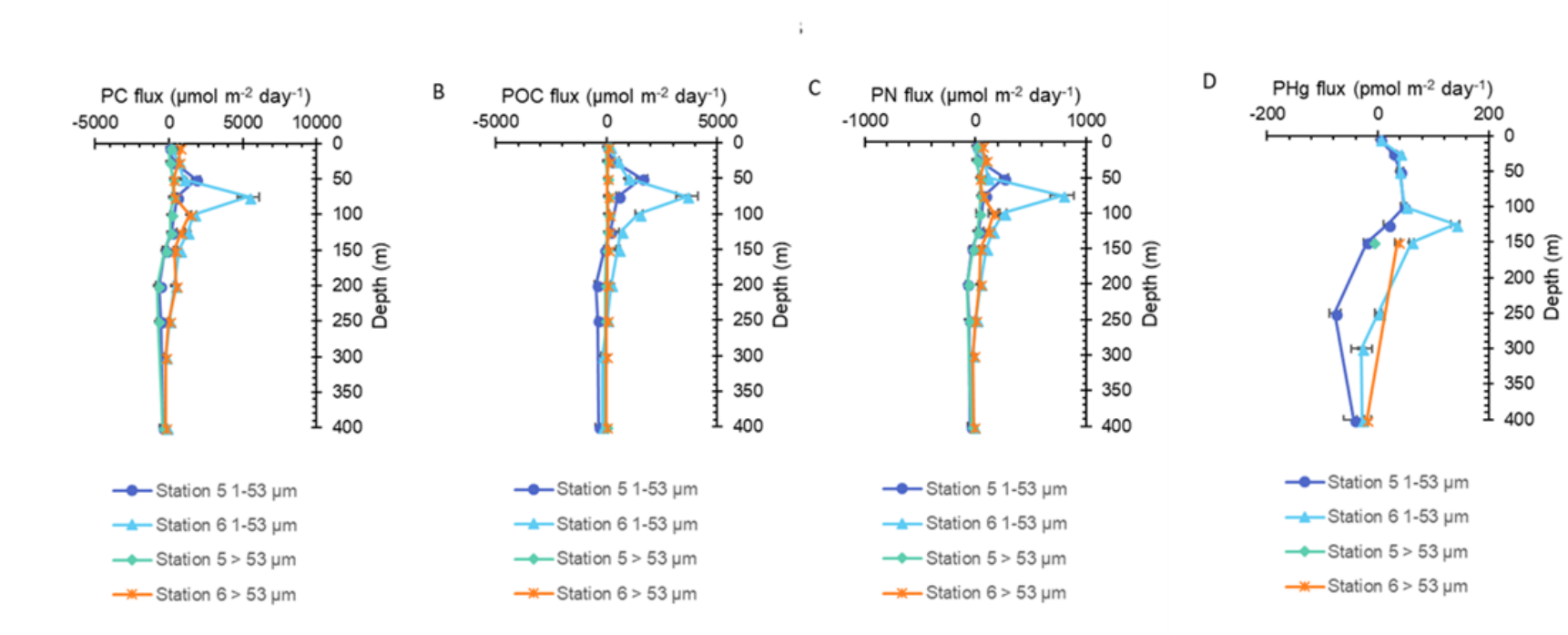

Figure 4. 5 Vertical profiles of Particulate Carbon (A), Particulate Organic Carbon (B), Particulate Nitrogen (C), and Particulate Mercury (D) fluxes for 1-53µm and > 53µm size fractions at stations 5 and 6. Abbreviations are PC: particulate carbon; POC: particulate organic carbon; PN: particulate nitrogen; PHg: particulate mercury

CHAPTER 5: CONCLUSIONS

5.1 Conclusions

The goal of this dissertation was to characterize particle cycling and the downward flux of particulate carbon (PC, nitrogen (PN), the neurotoxin domoic acid (DA), and mercury (Hg) in three different marine environments (coastal waters off Santa Barbara, U.S.A, Station ALOHA in the North Pacific Subtropical Gyre, and along a transect in the central North Pacific) using a combination of surface deployed sediment traps, in situ pumps, and ^{238}U-^{234}Th disequilibria. Changes in particle fluxes were examined across seasons, variation in water chemistry and shifts in ecology.

Chapter 2 focused on DA producing blooms of the diatom *Pseudo-nitzschia* in the Santa Barbara Basin, California. Concentrations of dissolved and particulate DA and *Pseudo-nitzschia* abundances were measured in the upper 150 m of water column across the Santa Barbara Basin as part a three-year time series. Samples were also collected from sediment traps moored at 147 m and 509 m in the center of the basin and at two pier based stations. *Pseudo-nitzschia* abundance and domoic acid concentrations were examined in the context of upwelling and non-upwelling seasons, and our results showed that blooms of *Pseudo-nitzschia* were not correlated with nutrient inputs from this process. Although *Pseudo-nitzschia* are solely responsible for the production of DA, bulk *Pseudo-nitzschia* abundance was a poor predictor of DA concentration, likely due to the variety of *Pseudo-nitzschia* spp with different toxicities within the ecosystem. Rather, DA concentrations in the dissolved phase, which were about half of the total DA measured, were a significantly better predictor of particulate DA concentrations (R^2 = 0.90). Our results add to the growing body of research suggesting that not only is dissolved DA significant and potentially involved in allelopathic effects, but it could be

used as a relatively easy indicator of particulate DA abundance. Sediment trap DA and *Pseudo-nitzschia* concentrations were decoupled from those in the upper 150 m, with less than 5% of DA produced in the upper water column reaching depths of 500 m. Nonetheless, once produced particulate DA sank rapidly and much more efficiently than bulk *Pseudo-nitzschia*, perhaps due to the formation of marine snow that minimized particulate DA remineralization.

In Chapter 3, seasonal changes (February 2014, September 2014 and May 2015) in PC, PN, and PHg fluxes derived using ^{238}U-^{234}Th disequilibria, *in situ* pumps, and sediment traps were examined at Station ALOHA in the North Pacific Subtropical Gyre. Results indicate that a large diatom bloom, likely facilitated by cyanobacteria, resulted in high PC and PN fluxes that ranged from 2135 to 477 μmol m^{-2} day^{-1}, respectively, at 150 m. In contrast, February was characterized by lowest PC and PN fluxes of 944 and 155 μmol m^{-2} day^{-1} respectively, while May PC and PN fluxes were intermediate, 1392 and 211 μmol m^{-2} day^{-1} respectively. Particulate C, PN, and PTh ratios coupled with complimentary measurements of the nitrogen isotope signature of amino acids in small and large particles as well as in size fractioned zooplankton, show very different biogeochemical cycling pathways occurring in the foodweb. In February, zooplankton grazing had a strong influence on particle flux, whereas in May and September, microbial reworking of particles was more influential. Small particles were a significant food source of zooplankton in Feb due to the absence of larger particles, while larger particles dominated food sources in May and September. These findings support the hypothesis that small particles are an important food source for mesopelagic zooplankton and fish much of the year. Particulate Hg fluxes showed similar seasonal trends to PC and PN,

but PHg fluxes were influenced more strongly by particle scavenging and microbial reworking below 150 m, with PHg fluxes at 150 m ranging from 83 to 146 pmol m^{-2} day^{-1} and increasing with increasing depth in September. These measured high pHg fluxes are among the highest measured in an open ocean ecosystem and explain the high mercury concentrations in fish that are known to feed in deeper waters. These results reinforce the need to characterize PHg fluxes as a source of Hg bioaccumulation at depth in marine foodwebs.

The potential impact of oxygen concentrations on PC, PN, and PHg fluxes was examined along a north-south transect in the central North Pacific in August 2015. Overall, particle fluxes were very low with little to no export occurring at depths of 150 m, averaging 255 ±447 µmol C m^{-2} day^{-1}YY using both sediment traps and ^{238}U-^{234}Th disequilibria. Two stations, one located within the oxygen minimum zone (8^{o}N), and the other in fully oxygenated waters (5^{o}N) were characterized in detail and had very similar hydrography and fluorescence profiles. While peaks in PC and PN export occurred coincident with the peak in fluorescence between 50 and 75 m, PC (and PN) fluxes in oxygenated waters was 2 times larger, 3629 µmol m^{-2} day^{-1}. Particulate Hg fluxes were at a maximum slightly deeper, ~ 100 m, but fluxes were also much greater in oxygenated waters, 140 pmol m^{-2} day^{-1}. We hypothesize that PC and PN fluxes likely differed due to a reduction in zooplankton feeding in low oxygen waters which reduced particle formation; large particles showed no increase in fluxes at depth. Particulate Hg was further influenced by increasing solubility by low oxygen environments coupled with limited bioaccumulation by larger taxa. Regardless, both sites where characterized by rapid remineralization immediately below their respective peaks, resulting in little to no

export by 150 m. Therefore, while oxygen concentration may influence the magnitude of particle formation in the upper column, it made no difference in the export that ultimately reached deeper waters in this system. As oxygen minimum zones become more prevalent due to oceans warming, it will be important to understand the impact these zones have on particle cycling.

In conclusion, characterizing particle fluxes is essential for understanding their biogeochemical cycling. These fluxes change both temporally and spatially, adding layers of complexity to their cycles. Knowledge of both zooplankton and phytoplankton community composition is essential for understanding particle cycling differences across size fractions, and in the case of compound or element specific particle cycles, a more detailed understanding at the genus and species level may be necessary. Water chemistry parameters that vary temporally and spatially (eg. Temperature, salinity, oxygen concentration) are most influential on particle cycling through the control they exert over local ecology, and accounting for these influences will be essential in future work.